# Study of Electrochemical Performance of Lithium and Zinc Metal Anodes for Rechargeable Batteries

Pranav Karanth

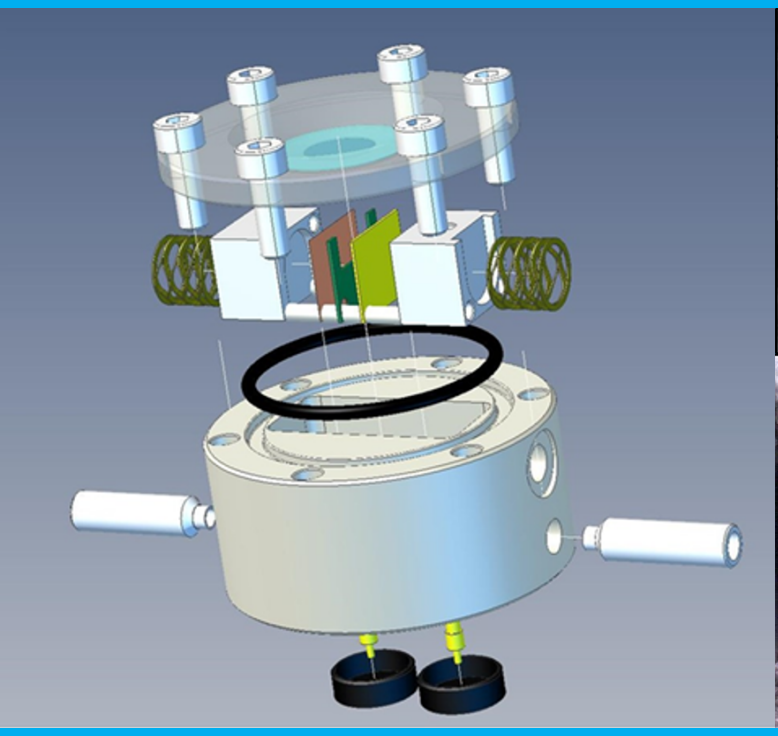

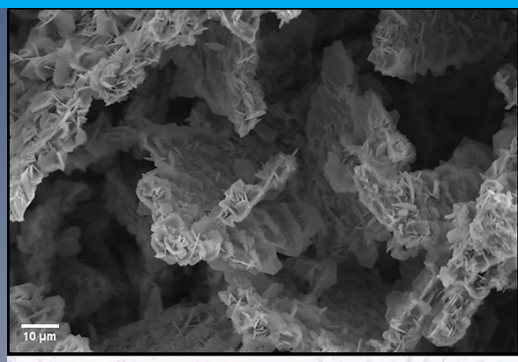


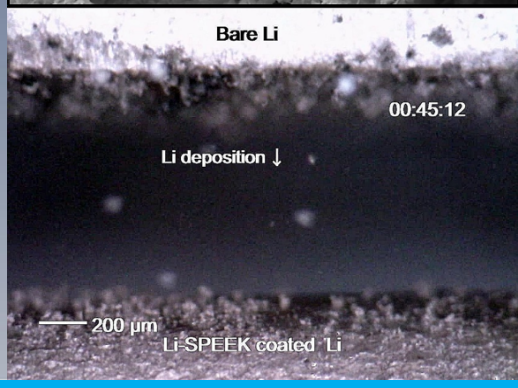


TU Delft

# Study of Electrochemical Performance of Lithium and Zinc Metal Anodes for Rechargeable Batteries

by

**Pranav Karanth**

to obtain the degree of Master of Science
in Sustainable Energy Technology
at the Delft University of Technology,
to be defended publicly on Thursday August 29, 2019 at 12:00 noon.

| | | |
|---|---|---|
| Student number: | 4740459 | |
| Project duration: | September 2018 – July 2019 | |
| Thesis committee: | Dr. E. M. Kelder, | TU Delft, supervisor |
| | Prof. dr. ir. M. Wagemaker, | TU Delft |
| | Prof. dr. S. J. Picken, | TU Delft |
| | Dr. S. Basak, | TU Delft, daily supervisor |

*This thesis is confidential and cannot be made public until December 31, 2020.*



TU Delft

# ACKNOWLEDGEMENTS

I look back at the past 11 months of my life as a Master research student at the RID with a sense of fulfilment and gratitude. Working on this project has given me the necessary background knowledge and experience to be able to pursue a research career in the field of batteries, and I am glad I made this choice.

I have several people to thank for, without whom this project would have been impossible. Erik, my main supervisor, has been immensely supportive of me since day one. I still remember some of our long-drawn-out discussions where he would patiently listen to all my queries and answer them convincingly. He has always ensured a steady progress of my project with timely, constructive feedback. I was allowed a great degree of freedom in terms of research and I truly appreciate that. Thank you very much, Erik.

Shiv, my daily supervisor is someone who has helped me in several ways: weekly planning, providing necessary insights into the experiments, regular feedback, critical evaluation of my ideas, help with SEM/TEM and so on. He has contributed a lot to helping me grow as researcher and I cannot thank him enough for that. Special thanks also to Frans, for his important contribution to the design of the operando microscopy cell and its optimization, and for being there to offer all sorts of practical help when required. I would like to thank Shell, the sponsors of the project, for being constantly supportive of our research progress, and also Xiaoming Huang from PTG Eindhoven for the help with the XPS analysis.

I would also like to thank all the people associated with the SEE group for their support and co-operation. Special thanks also to the fellow master students, who contributed greatly to making this experience a pleasant one. I am sure we have learned a lot from one another during this period, both academically and otherwise. Finally, I would like to thank my family for all the support throughout this period.

*Pranav Karanth*
*Delft, August 2019*

# ABSTRACT

Metal anode based batteries, considered the ideal upgrade to Lithium ion batteries in terms of energy density, are currently held back by the non-homogeneous deposition phenomenon that leads to the formation of dendrites that short circuit the cell. The solution to this problem is twofold: while it is important to come up with solutions that mitigate/resist dendrite formation, it is more important to fully understand the deposition phenomena in metal anodes through experiments and theoretical analyses.

This study aimed to first understand the deposition mechanism in Zinc and Lithium metal anodes, and then study the feasibility of polymer coatings based on Sulfonated Poly Ether Ether Ketone (SPEEK) as a solution to mitigating the dendrites.

The electrochemical performance of Zinc in $ZnSO_4$ electrolyte systems was studied for a wide range of current densities and for different operating conditions with the help of operando microscopy and ex-situ SEM. Further, the mechanism of initial Zinc deposition was visualized with the help of in-situ TEM. The origins of the different types of morphology observed at these conditions were explained on the basis of competition between the mass transfer and the kinetics for control over the overall process. Further, a proof of concept was established for the use of SPEEK based coatings on Zinc metal, and the electrochemical performance of polymer coated Zinc electrodes was analyzed.

In the case of Lithium, the deposition in carbonate based electrolytes was first studied with the help of operando microscopy for Bare Lithium. Operando microscopy was also carried out to study the influence of the SEI, the separator and a standard polymer coating (PVDF) on Lithium deposition. Further, Lithiated SPEEK was used as a polymer coating on Lithium, and it was observed that a more even Lithium deposition takes place with the Li-SPEEK coating on Lithium. Slight improvements were observed in the $Li^+$ conductivity of the coating with the addition of $TiO_2$ nanofiller to the polymer. However, performance issues were observed with long term cycling, possibly due to the instability of the polymer coating in carbonate electrolytes over long periods.

**Keywords:** Lithium metal anode, Zinc metal anode, Dendrites, SPEEK, Operando microscopy

# CONTENTS

# List of Figures

# 1

# INTRODUCTION

Batteries are all set to be an integral part of the future energy infrastructure largely powered by renewables. Lithium ion batteries currently enjoy the lion's share of the market, but better alternatives are desired for, both in terms of energy density and cost effectiveness. While batteries with Lithium metal as the anode could be a potential solution to the energy density issue, Zinc-ion batteries with Zinc metal as the anode could serve as a cost effective alternative to Lithium ion batteries, especially for stationary applications. The key to making both these battery chemistries work is to ensure safe and long operation of the metal anodes used, and this serves as the primary motivation behind this study.

## 1.1. THE CASE FOR ZINC-ION BATTERIES WITH ZINC METAL AS THE ANODE

Batteries with Zinc as the anode and aqueous electrolytes were one of the first commercially produced. While the classic leclanche cell and dry cell types used an $ZnCl_2$-$NH_4Cl$ amalgam electrolyte, while the later 'high duty' versions used KOH with dissolved ZnO as the electrolyte. While these batteries provided a superior power and energy density thanks to the high ionic conductivity of KOH, the rapid degradation of the Zinc anode and safety concerns owing to leakage of the electrolyte etc. still remained unaddressed.

Researchers are increasingly looking towards inexpensive and safer alternatives to Lithium ion batteries, particularly for stationary energy storage. Zinc air and Zinc ion batteries, with anodes based on inexpensive and abundant Zinc are gaining rapid attention. Of these, Zinc ion batteries have generated great interest as these systems can use Zinc metal directly as the anode and usually involve near neutral pH aqueous electrolytes that ensure safer operation and longer lifetimes of the metal anode in comparison to alkaline systems. While the bulk of the research today in the field of Zinc ion batteries is based on establishing new intercalation based cathode materials with high discharge capabilities and long lifetimes, it is also important to study in isolation the

performance of the Zinc metal anode in such electrolyte systems and establish the performance metrics for the same.

The Zinc anode has been studied at battery level applications in the past, but the studies have mostly been related to its performance in alkaline electrolyte systems. [16] On the other hand, electrodeposition studies of Zinc in neutral systems (such as $ZnSO_4$) have been mostly been done for macroscale applications such as electroplating. It is therefore, of interest to study the electrochemical performance of Zinc anode in mildly acidic electrolytes at a scale relevant for battery systems.

## 1.2. LITHIUM ANODE BASED BATTERIES: CHALLENGES AND POSSIBLE SOLUTIONS

Lithium-ion batteries currently rely on liquid organic electrolytes, whose main advantage is the high ion conductivity. However, challenges related to flammability (regarding safety) and Lithium dendrite growth ( regarding life-time of the battery) are urging people to look for alternative electrolytes. Polymer electrolyte is emerging as an alternative aimed the inherent flexibility in dealing with the volume changes of the electrode during cycling, but still require optimization in terms of stability and conductivity.

One of the ways to reduce Lithium dendrite growth while also ensuring high ionic conductivities is to produce a protective, homogeneous SEI layer that greatly reduces the amount of liquid electrolyte coming in contact with the Li metal. The non-homogeneous SEI that forms when conventional liquid electrolytes react with the Li metal leads to uneven Li distribution on the surface and eventually dendrites. A protective surface coating would not only homogenize the Li flux, but also mechanically resist any possible dendrite growth, thereby ensuring a longer, safe operation of Li-ion batteries. A uniform surface layer can be achieved either by means of electrolyte additives that readily react with Li to give a uniform layer, or by coating Li with conductive polymers beforehand.

Perfluorosulfonic acid based polymers such as Nafion have already been utilized as surface coatings, as PFSA based compounds also provide the additional benefit of hindering polysulfide diffusion to the Li metal anode in the case of Li-S batteries. Sulfonated Poly Ether Ether Ketone (SPEEK) also a PFSA based polymer, therefore proves to be an interesting candidate for achieving protective surface coatings on the Li metal anode. Further, SPEEK could also potentially work as a protective coating for Zinc in aqueous batteries, as the material is known to be conductive in aqueous systems.

## 1.3. OPERANDO MICROSCOPY AS A TECHNIQUE TO STUDY METAL ANODES

Over the years, the global battery research community has attempted to tackle the issue of dendrite formation in metal anodes and has also come up with several possible solutions to overcome this drawback. In comparison, little research has been carried out to understand the mechanistic origins of these ramified deposits. A simple but elegant technique to visually study the morphology evolution on these metal anodes is the Operando Optical Microscopy. Although limited by the maximum possible resolution to some extent, Optical microscopy could be an effective tool to study the deposition and

stripping phenomena in these metal anodes, as demonstrated by the likes of Dasgupta et. al. [7], Bai et. al. [17] and several others.

## 1.4. SCOPE OF WORK AND RESEARCH QUESTIONS

This study aims at studying the electrochemical performance of Lithium metal anodes in organic electrolyte systems, and Zinc metal anodes in mildly acidic electrolyte systems ($ZnSO_4$ in this case) with the help of operando optical microscopy, and further, the effect of polymer based protective coatings on the electrodeposition mechanism for both these anodes, with a special focus on the ionomer Sulfonated Poly Ether Ether Ketone (SPEEK).

Further, since the Zinc metal anode has not yet been investigated in detail at the battery scale for mildly acidic electrolyte systems, it is also desired to arrive at a comprehensive model that describes the electrochemical performance across various current densities and with changes in the other operating parameters such as the salt concentration and the temperature.

The research questions relevant to this project could be posed under two categories:

**1. Study of Bare Zinc and Lithium metal anodes with Operando microscopy:**

**a) How does the morphology evolution occur in the case of a Zinc metal anode in a $ZnSO_4$ electrolyte system :**

- **across different current densities?**
- **with time and number of cycles?**
- **with changes to the operating parameters?**

**b) How does the competition between the mass transfer (diffusion) and the kinetics for control over the overall Zinc ion transfer process influence the morphologies and the crystal orientations of the Zinc deposits?**
**c) How does Lithium deposit in carbonate electrolytes at nominal current densities? How do the SEI and separator influence the plating and the overall cycling?**

**2. Performance of SPEEK as a protective coating on Lithium and Zinc:**

**a) Can SPEEK be used a coating to protect the Zinc metal anode in aqueous systems at moderate to high current densities?**
**b) How does Li-SPEEK behave when used as polymer coating on Lithium?**

- **Is it mechanically and chemically stable with the organic electrolyte?**
- **How do the thickness and the uniformity of the coating influence its electrochemical performance?**
- **Can the performance of SPEEK as a coating be improved by doping with ceramic nanoparticles to improve the conductivity?**

# 2

# Literature Review

This chapter aims at introducing the reader to the basics, the research challenges involved, and the role of polymers in the development of batteries that use metallic Zn and Li as the anode. The theories of dendrite formation are discussed. Further, polymer electrolytes and their previous applications in metal anode based cells are briefly discussed. Finally, a special class of polymers known as ionomers are introduced, their successful applications in batteries are highlighted, and possible avenues for performance improvements in ionomer based coatings are also discussed. Most of these sections serve as a justification to the choice of materials and methods that are a part of this study.

## 2.1. Zinc-ion Batteries

### 2.1.1. Working Mechanism

A Zinc ion battery normally consists of metallic zinc as the anode, a near neutral (or mildly acidic) electrolyte and a cathode that can intercalate $Zn^{2+}$ ions.

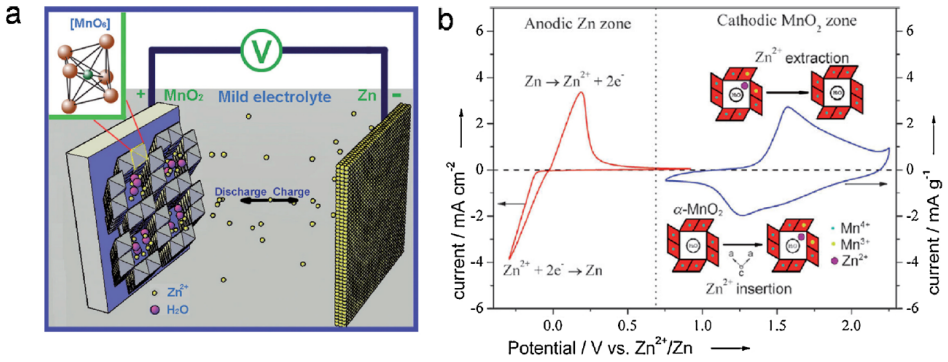


Figure 2.1: Schematic of a Zn-ion Battery [1]

One of the most commonly studied Zn ion battery systems is the Zn/1M $ZnSO_4$/$\alpha$-$MnO_2$ system. ([2] The migration of $Zn^{2+}$ ions between the metal Zn anode and the tunnels of the $\alpha$-$MnO_2$ intercalating cathode can be described as follows:

The two reactions are as follows [2]:

At the anode:

$$Zn \rightarrow Zn^{2+} + 2e^- \tag{2.1}$$

At the cathode:

$$Zn^{2+} + 2e^- + 2\alpha - MnO_2 \rightarrow ZnMn_2O_4 \tag{2.2}$$

The salt in the electrolyte solution, i.e. $ZnSO_4$, fully dissociates into $Zn^{2+}$ and $SO_4{}^{2-}$ ions, and the electrical current is carried in the solution by both these species. The transference number of $Zn^{2+}$, or the fraction of the total electric current carried by the $Zn^{2+}$ ions in the solution is a function of the relative electrical mobilities of the two ions, and is about 0.4 for $Zn^{2+}$ in $ZnSO_4$ [18].

The insertion of $Zn^{2+}$ ions generally results in the phase transition of the cathode; in this case, from a tunneled structure to a spinel structure, although some studies have also reported transitions to other structures.[2] While insertion/extraction is the most commonly reported mechanism for Zinc transport into cathode materials, reaction- conversion mechanism has also been reported for several cathode materials.[2]

### 2.1.2. CHOICE OF ANODE, ELECTROLYTE AND CATHODE IN ZN-ION BATTERIES

**Anode:** As noted earlier, one of the advantages of the Zinc ion battery is the possibility of using the metallic Zinc foil directly as the anode. In addition to the high energy density provided by the usage of Zinc directly as a foil, Zinc has been known to exhibit remarkably better plating/stripping efficiency in mild acidic/neutral electrolytes as compared to alkaline electrolytes [1]. Also, the usage of mildly acidic electrolytes render metals such as Cu and Al unsuitable as current collectors for the electrodes. Even for the cathode, stainless steel, Titanium and Carbon based current collectors are used. [2].

**Electrolyte:** Several aqueous electrolyte candidates in the near-neutral regime have been studied. Some of these include $ZnSO_4$, $Zn(CF_3SO_3)_2$, $ZnCl_2$, Zn acetate and $Zn(NO_3)_2$. Of these, $ZnCl_2$ and $Zn(NO_3)_2$ displayed poor coulombic efficiencies owing to the instability of $Cl^-$ and $NO_3{}^-$ ions. [2] $ZnSO_4$ and $Zn(CF_3SO_3)_2$ are the mostly widely used electrolytes, owing to their higher stability and compatibility with intercalation cathodes.

Of the two, $Zn(CF_3SO_3)_2$ was observed to have better reversibility and faster kinetics of Zinc deposition and dissolution. This is because the $CF_3SO_3{}^-$ ions are bulkier (as compared to $SO_4{}^{2-}$ with a double charge) and this decreases the number of water molecules surrounding the $Zn^{2+}$ ions, which reduces the solvation effect and enables better $Zn^{2+}$ transport. [19] It has to be noted, however, that $Zn(CF_3SO_3)_2$ is significantly costlier than $ZnSO_4$ at this point, thereby presenting a roadblock to the commercialization of batteries with these electrolytes.

In addition, the effects of additives along with these electrolytes have also been studied. It has been demonstrated that the presence of certain ions such as $Na^+$ and $Mn^{2+}$ ions in the solution can improve the performances of the anode or the cathode, or sometimes both. While $Na^+$ ions can prevent Zinc dendrite formation at high current densi-

ties by means of an electrostatic shield mechanism,[20] many researchers have reported improved performances with the usage of $Na^+$ and $Mn^{2+}$ salts in addition to the electrolyte, and this has been attributed to the reduction dissolution of cathode materials. [19] Further, a higher concentration of the electrolyte salt has also resulted in improved Coulombic efficiencies according to researchers like Chen et al.[21]

**Cathode:** A lot of research within Zn-ion batteries is focused on Cathodes, as it is highly challenging to develop materials that are structurally stable at high insertion rates, facilitate fast $Zn^{2+}$ diffusion into the lattice and offer high energy densities. Manganese based oxides, Vanadium based oxides, Prussian Blue analogs, polyanion compounds etc. have all been reported to facilitate reversible $Zn^{2+}$ intercalation/reaction. [2]. As it can be inferred from Fig. 2.2, each group of compounds offers its own advantages. While Manganese oxides appear to offer both a high potential and specific capacity, other groups such as Vanadium oxides have been reported to be more structurally stable over time. [19]

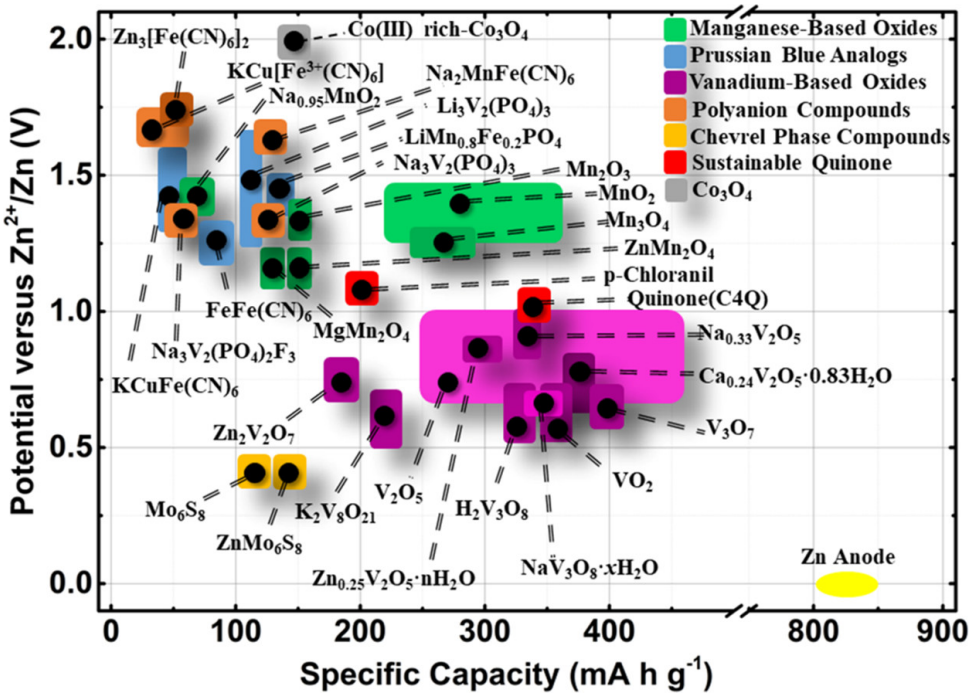


Figure 2.2: Cathode Materials for Zn-ion Batteries [2]

### 2.1.3. PERFORMANCE CHALLENGES OF ZINC ION BATTERIES

Zn-ion batteries can suffer from performance issues both on the Cathode and the Anode side.

**Cathode Performance:** As already stated, Manganese oxide based cathodes that offer high potential and specific capacity suffer from poor stability and capacity fading,

largely owing to the dissolution of $Mn^{2+}$ ions in the electrolyte. While such dissolution can be prevented to some extent by already having $Mn^{2+}$ ions in the solution, the capacity fading still remains a problem. Also, the determination of the mechanism of $Zn^{2+}$ uptake (intercalation vs reaction conversion) in Mn based cathodes is also rather complicated and requires a more detailed study in order be able to design better cathodes. [2].

Other Cathode groups such as Vanadium oxides suffer from strong electrostatic interactions between the host lattice and the $Zn^{2+}$ ions, resulting in a slow diffusion of $Zn^{2+}$ ions and entrapment of a part of $Zn^{2+}$ ions in the host lattice or formation of Zn containing Vanadium phases. Increasing the reversibility and kinetics of $Zn^{2+}$ insertion into Vanadium based cathodes is therefore, a major challenge.

**Anode Performance:** High discharge rates can also result in poor performance of the Zinc metal anode, and can result in dendrite formation. In the previously used Alkaline electrolytes, the Zinc anode suffered from a number of issues in addition to dendrite formation, such as corrosion of the Zinc anode and passivation of the Zn surface due to precipitation of ZnO. Another major issue was the spontaneous evolution of Hydrogen as a side reaction during Zn deposition and this was mostly due to the favourable thermodynamics of the HER at basic pH. It was, in fact, this collection of performance issues that led to the exploration of mildly acidic aqueous electrolytes for Zn-ion batteries.

The degree of dendrite formation largely depends on the initial shape change induced by the electrolyte on the Zinc anode, and such shape change can be explained by the so called 'density gradient theory'. [22] As it has been demonstrated by several researchers, such corrosion is absent in mild acidic electrolytes [1] and therefore the degree of dendrite formation is a lot lesser, although the problem still exists. A lot of research efforts have therefore been devoted to tailoring the surface charge distribution on Zinc. Moreover, attaining a high Coulombic efficiency also remains a challenge owing to the various side reactions that consume the anode and the electrolyte. [2]

## 2.2. LI-S BATTERIES AND THEIR PERFORMANCE ISSUES

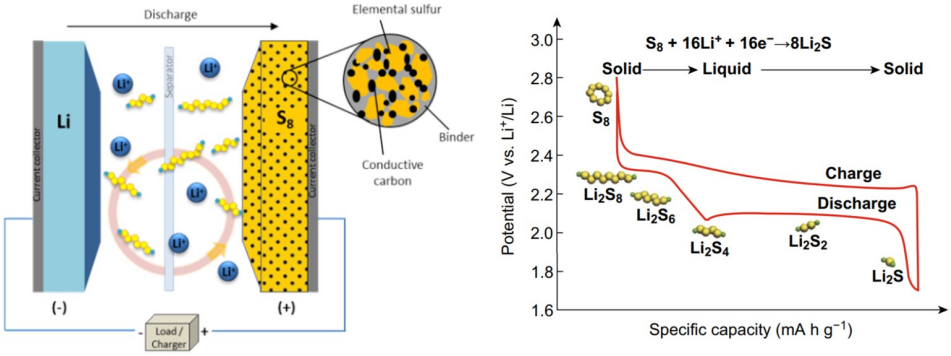


Figure 2.3: Schematic of a Li-S Battery (left) [3], Typical Charge discharge profile of a Li-S battery (right) [4]

The Lithium Sulfur battery is one of the most widely researched topics under energy

storage devices, thanks to the promise of being able to combine high energy density with cost effectiveness. While the energy density provided by Lithium metal anode is theoretically the highest, Sulfur as the cathode material also provides a theoretical gravimetric capacity of about 1675 mAh/g nearly six times that of the widely used NMC cathodes (278 mAh/g). Moreover, Sulfur's availability as an abundant, inexpensive material is also a huge advantage over the existing cathodes that rely heavily on rare earth metals such as Cobalt. However, it needs to be noted that Sulfur cathodes require a conductive carbon matrix to make up for the insulating properties of Sulfur and also the volume changes occurring during cycling.

The electrolyte used is usually based on a 1:1 (by volume) mixture of 1,3-dioxolane (DOL) and 1,2-dimethoxyethane (DME).The dissolved salt can be either LiTFSI or $LiClO_4$, often with a small weight percentage of $LiNO_3$ as an additive. [23]

**Polysulfide related performance issues:** A large share of Li-S battery research is focused on optimizing the electrochemical process at the cathode. The S cathode ($S_8$) undergoes a conversion reaction to give $Li_2S$ during the discharge phase through a series of multiple chemical and electrochemical reactions. The overall reaction of the Sulfur cathode and the various intermediates formed corresponding to their point of appearance in the voltage trace are shown in Fig. 2.3 (right). [4]

This gives rise to several intermediate species known as polysulfides, and these polysulfides dissolve in the electrolyte, diffuse throughout the electrolyte window, rupture the SEI layer and reach the Li metal anode. Their reaction with the Li metal anode continuously consumes active Lithium. Therefore, polysulfide diffusion can be highly detrimental to the lifetime of the battery as the active material in both the anode and the cathode are consumed on a continuous basis. [23] $LiNO_3$, widely used as an electrolyte additive in Li-S batteries, stabilizes the Li anode performance to some extent by forming a stable SEI and inhibiting the reactions between the polysulfides and the Li metal anode. However, such additives, limited by their wt% are not beneficial for the long term performance as $LiNO_3$ is also consumed during the continuous cycling. [24] Other approaches to tackle this issue mostly have to do with developing cathode materials that can encapsulate these polysulfides. [23] the use of polymer interlayers with functional groups that block the diffusion of polysulfides is another interesting approach, which will be discussed in detail in section 2.8.

**Anode related performance issues:** A major issue with any battery having Lithium metal as the anode, is the uneven Lithium deposition eventually leading to the formation of dendrites that can short circuit the cell. In short, dendrite formation in Li metal is primarily a consequence of the heterogeneous solid electrolyte interphase formed by reaction with the organic electrolytes. In addition, the accumulation of dead Lithium with each cycle is another major challenge, as the electrolyte continuously reacts with the unevenly deposited Lithium to form fresh SEI layers and electrically insulate these deposits. A significant amount of research is therefore focused on achieving a homogeneous, stable long term SEI layer either through electrolyte additives or through anode pretreatment to obtain coatings. The phenomenon of dendrite formation will be discussed in detail in section 2.3.

## 2.3. GENERAL THEORY OF ELECTRODEPOSITION AND DENDRITE FORMATION

Over the years, several researchers have tried to explain the initiation and growth phase of dendritic deposits on native metals. Prominent among them are Bockris et al. [25] and Chazalviel et al. [26][27] While the theory proposed by the Bockris group is based on surface forces and mass transport, the latter is based on electromigration limitation due to depletion of cation concentration and creation of space charge layers that influence the ramified growth of deposits. It is important to note here that while both the theories posit the existence a minimum current density for dendritic growth to take place, the so called limiting current proposed by Chazalviel et al. is generally much higher in magnitude.

### 2.3.1. THE BOCKRIS MODEL

The summary of the model proposed by Bocrkris et al. over two papers is as follows. A minimum current density, corresponding to a minimum overpotential, is required for the initiation of bulk diffusion controlled deposition (nucleation) of metal on the given substrate. Under bulk linear diffusion control, the prismatic (or pyramidal) outgrowth of the deposits happens wherein the height of the deposits increases with time while the radius of their tip decreases.

At a certain time, the tip of the deposits and attains a stable tip radius much smaller than the thickness of the diffusion layer of the macroelectrode to ensure that spherical diffusion at the tips is now favourable over linear diffusion. This point in time corresponds to the onset of dendritic growth. After the initiation, the dendritic growth is beyond the control of diffusion boundary layer of the macroelectrode, and is nearly controlled by the kinetics of deposition at the tips, i.e. the dendrite growth is almost linear in time the rate of dendritic growth is directly proportional to the applied overpotential.[25] [28] [29]

### 2.3.2. THE CHAZALVIEL MODEL

The theory proposed by Chazalviel for dendritic growth in solutions with a binary salt as the electrolyte and current densities higher than the limiting current density is as follows. (Again, a minimum activation overpotential is required for the initial deposition of metal on the substrate.) A concentration gradient of metal cations exists from the cathode to the anode (the native metal/substrate on which the deposition is happening).

During electrodeposition on the metallic anode, it is the cathode where oxidation takes place and therefore this positively charged electrode attracts anions from the solution. Unlike the metal cations, these ions cannot deposit, so they pile up to form a so called space charge layer with excess negative charge. On the other hand, the depletion of anions at the anode side causes a buildup of excess positive charge, influencing the local electric field. Further, at values of current density greater than the limiting current, the concentration of the metal cation eventually drops to zero near the anode, at a time known as Sand's time. This corresponds to the onset of dendritic deposition. At this point, the electroneutrality condition is violated and the potential is observed to diverge owing to the lack of charge carriers. (An example for Sand's time calculation, conducted

as a part of this work, can be found in Appendix A.3)

Once the electric fields have attained a high enough value, instability of electric field across the metal anode surface occurs, and new deposits find increased electric field at their tips causing ramified dendritic growth in the direction of the electric field. In order to avoid further accumulation of space charge, these deposits would have to grow at a velocity of $-\mu_e E_o$, where $\mu_e$ is the mobility of anions and $E_o$ the applied electric field. Thus, it could be concluded that the dendritic growth is again under activation control. [26] [27]

### 2.3.3. THE THEORY OF SEI FORMATION

The two aforementioned theories do not satisfactorily explain the formation of dendrites at current densities lower than the limiting current in Lithium based systems that normally involve the formation of a Solid Electrolyte Interface (SEI) on reaction with the organic electrolytes involved. The additional detrimental effect caused by the SEI leading to SEI formation can be explained using the Mosaic theory. [30]

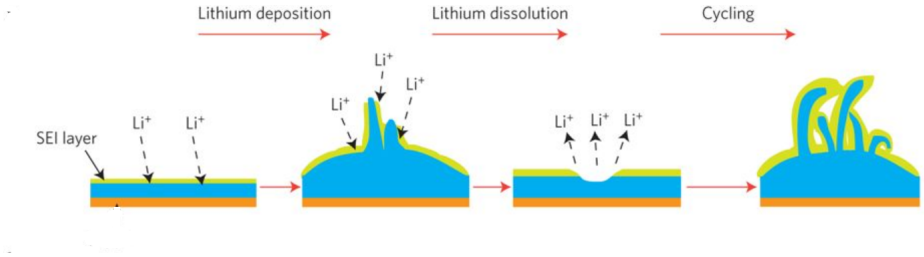


Figure 2.4: Mechanism of Dendrite formation with Li metal anode [5]

$Li^+$ conductivity and Electric field distribution through the SEI over the given surface is generally non-homogeneous , mainly owing to the different SEI components formed at uneven thicknesses. Moreover, the SEI film is not stable and usually cracks as a result of successive volumetric expansion and stress caused by Li plating and stripping. The resulting cracks at the defects of SEI films causes electrochemical hot spots, wherein fresh Li gets exposed.

Bare Lithium has a lower energy barrier for $Li^+$ ions than the SEI components, thus resulting in a higher degree transport and deposition on exposed Li region, and this triggers filamentary and dendritic Li growth. [31][30]

### 2.3.4. COMPOSITION OF THE SEI LAYER AND ITS OPTIMIZATION

The Mosaic model [30] indicates that the SEI composition across the surface is not homogeneous, but rather a mixture of insoluble multiphase products. The SEI is not homogeneous in the thickness direction either, and has a dual (inorganic-organic) layer structure. The inorganic layer is formed on the Li metal side and is made of lower oxidation state species such as $Li_2O$, $Li_3N$, LiF, LiOH, and $Li_2CO_3$. The outer organic layer consists of higher oxidation state species, such as $ROCO_2Li$, ROLi, and $RCOO_2Li$ (R is the solvent related group). In general, the organic components of the SEI layer are determined

by the solvent, and the inorganic components determined by the salt-solvent reactions. [32] The SEI chemistry also depends on the $Li^+$-solvation sheath. The solvent–solvent and salt–solvent local structures can strongly influence the reduction voltage and kinetics. [33]

In comparison to conventional Lithium batteries, Li-S systems tend to have a somewhat different composition of the SEI layer. These batteries generally employ solvents with lower reduction voltages, i.e. dioxolane (DOL) and dimethoxyethane (DME). both DOL and DME are relatively stable against the Li metal surface in comparison to carbonate based electrolytes that decompose spontaneously. The salt commonly used, LiFSI, decomposes completely and forms LiF as the main SEI component. Further, Li-S batteries have polysulfide decomposition before that of any other electrolyte component, and precipitation of the $Li_2S$ formed on Lithium is also thermodynamically stable. [33]

One of the foremost requirements of the SEI layer is that it must be able to avoid further electrolyte reduction reaction by blocking the tunneling of electrons from the electrode to the electrolyte. This particular action is achieved by the inorganic layer of the SEI.[33]. Lin et al. calculated the critical thickness that prevents electron tunneling for LiF, $Li_3PO_4$, and $Li_2CO_3$. The order was found to be $Li_2CO_3$ > $Li_3PO_4$ > LiF, implying LiF has the best electronic insulation of the three. They also concluded that an SEI with only a few nanometres thickness is sufficiently effective to protect Li metal from the electrolyte reduction reactions, provided the inorganic SEI layer is a complete crystal without pinholes [32]

The most common approach to obtain a uniform SEI layer has, therefore, been to include electrolyte additives that readily undergo reduction first to form a stable layer. Vinylene Carbonate (VC) is commonly used for graphite anodes and has also been explored for Li anode. While every solvent and salt species has a unique decomposition voltage, this value is sensitive to the nearby $Li^+$ ions. Considering the $Li^+$-solvent complexes in the implicit solvent, the first electron reduction order for carbonate electrolytes is VC > PC  EC  DMC (cis–trans) > DMC (cis–cis) Fluoroethylene carbonate (FEC) is another commonly used additive, particularly for Si and Sn anodes but also for Li metal. LiF is the main reduction product obtained with FEC. [33]

Further, the mechanical stability of the SEI formed also plays a crucial role in determining the lifetime of the Li metal. A mechanically stable SEI would remain intact despite the expansion/contraction of the electrode during successive cycling. Reversible (elastic) deformation of the layer is desired over irreversible (plastic) deformation. In the case of artificial SEI layers, mechanical strength and electrode adhesion are therefore considered to be the key performance indicators, as fracture and delamination of such layers are to be prevented at all costs. In general, the stiffness of the SEI decreases from the inorganic to the organic and then to the polymeric components. Among the commonly occurring inorganic components, LiF has the highest stiffness. [33]

## 2.4. MORPHOLOGY STUDY OF ZINC - EFFECT OF PROCESS PARAMETERS AND MATERIALS USED

While the dendritic morphology formed at high current densities is something that can be easily recognized for most metals, as many five distinct morphologies have been ob-

served for Zinc deposition from Alkaline solutions at a battery scale. It is to be noted however, that the Zinc exists as zincate $(Zn(OH)_4)^{2-}$ in alkaline solutions and the degree of corrosion associated with Alkaline solutions is much higher, and therefore, one should not expect to see a similar morphology change at similar current densities for mildly acidic solutions. Nevertheless, it is important to know the characteristics of these different types of Zn deposits that allows for easy detection and identification for future researchers. According to Zhang et al. [6] there are five types of zinc deposits, namely mossy or spongy, layered, granular, dendrite, and cluster (cluster has also been referred to as 'heavy spongy' in [16]); they occur in the order of increasing current density. The additional characteristics of each type of deposit has been listed in Fig. 2.5b.

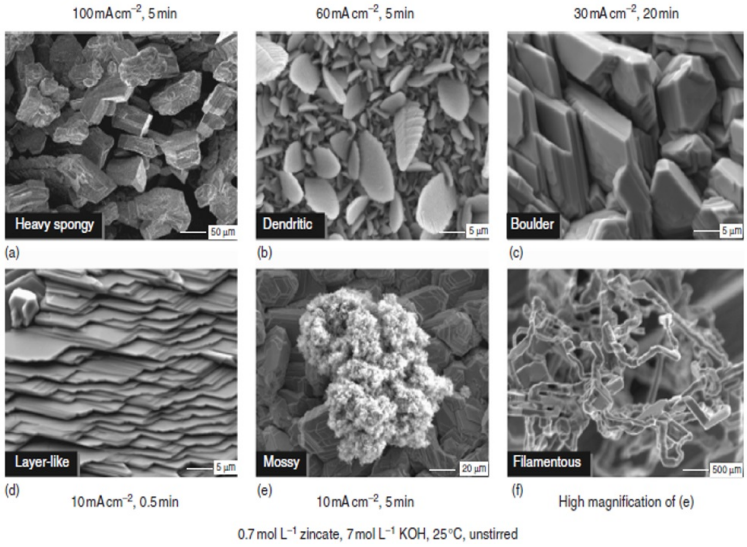


Figure 2.5: Types of Zn deposits in Alkaline Solutions [6]

In addition to the current density, the appearance of a certain morphology type could also depend on several other factors. For instance, A mossy deposition could also occur on top of a smooth deposit at a low current density at longer deposition times. Certain morphology types, such as the layered/flaky and the boulder deposit (together referred to as compact deposits) are transient in nature, and tend to be replaced by other other morphological types as the deposition/cycling progresses.

Further, it can be noticed these morphologies differ in several aspects such as porosity, crystal growth direction and nucleation site selectivity. While compact deposits tend to adhere to the substrate well, mossy, dendrite and cluster deposits tend to be porous, dispersed and non-adherent. Except for boulder and cluster deposits that are anisotropic (i.e. grow randomly in all three dimensions with individual deposits also having a polycrystalline nature [16]) in nature, the preferred growth plane for these deposits is generally [001] and [101], while, the preferred growth directions are [112] and [101]. [16]

In addition to current density and time, the effect of various process parameters such as zincate concentration in the solution, temperature, surface roughness, nature of the

substrate etc. have all been shown to alter the deposition morphology. The shift of the morphology regime towards mossy at high temperatures and concentrations and dendritic at low temperatures and concentrations can be noted from the morphology diagram. An increased surface roughness resulted in mossy deposition on rough surfaces at low to moderate current densities, while it did not have much of an effect at high current densities. While not relevant for deposition on native metal surface, deposition on a different metal substrate could also result in different initial morphologies and growth mechanisms depending on the degree of compatibility of Zn with the substrate. [16]

While there have been efforts to perform similar morphology studies for Zinc electrodeposition from mildly acidic solutions at the battery scale, [34] they have not been as detailed as the study by Zhang et al. [16] for alkaline systems. Therefore, with Zn-ion battery related research slowly gathering momentum, it would be of interest to study in detail the variations in morphology for Zinc deposition in mildly acidic solutions.

## 2.5. OPERANDO MICROSCOPY TO STUDY THE MORPHOLOGY EVOLUTION ON METAL ANODES

While a lot of morphology studies for both Zn and Li are based on post-mortem ex-situ analysis of the cycled samples, some of the studies have even attempted operando optical (video) microscopy to capture the morphological changes on the metal changes. Dasgupta et al. [7] took this a step further by performing the operando microscopy on a Li-Li symmetric visualization cell and also linking the time-dependent morphological changes observed in the visualization cell with the corresponding changes in electrochemical (voltage) response curve. Doing so allows for a detailed understanding of the electrochemical processes occurring on the metal anode surfaces, and how the transitions between reaction (or rather the lowest impedance) pathways for electrodeposition and electrodissolution lead to changes in the observed voltage traces. [7]

### 2.5.1. THE CHARACTERISTIC VOLTAGE TRACE

The commonly observed characteristic voltage trace for metal-metal symmetric cells is as follows. In the first half-cycle, the cell potential always decreases from a maximum. In the half-cycles that follow, the voltage trace (1) drops from a maximum, (2) decreases to a minimum, (3) increases up to a local maximum, and (4) decreases thereafter. This characteristic voltage trace has been observed for a wide range of current densities, for various electrolytes, and for different cell configurations by several researchers. [7]

Figure 2.6, taken from the work of Dasgupta et al. [7], shows the observed morphological changes on the Li metal anode alongside the corresponding voltage trace.

### 2.5.2. THE IMPEDANCE PATHWAY MODEL

Dasgupta et al. explained the observed morphological changes and voltage traces by means of an impedance pathway model for each of the cell components, the schematic representation of which is shown in Fig. 2.7. The overpotential at each electrode is a function of the total current, which is equal to a sum of the individual currents for each of the 'impedance pathways' at that electrode, i.e. the value of the current through each pathway is inversely proportional to the overall impedance of that pathway. The domi-

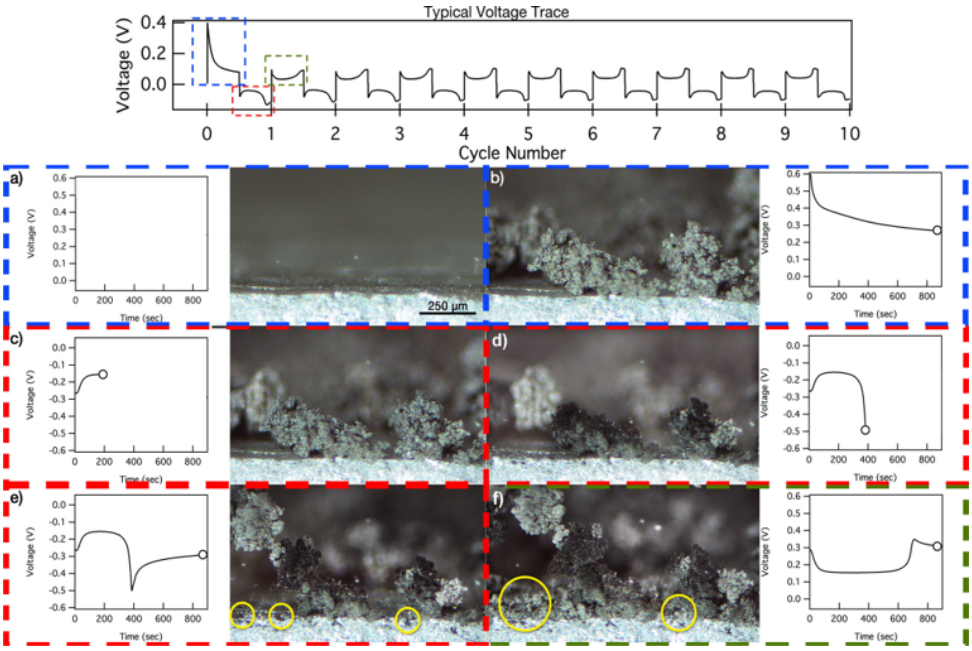


Figure 2.6: Morphology evolution on the Lithium metal anode corresponding to various stages in the overall voltage trace, as obtained by Dasgupta et. al. [7]

nant current pathway at each electrode is the one with the lowest impedance, and this makes the greatest contribution to the overall electrode overpotential.

In Fig. 2.7b, the regions corresponding to the area fraction of each process, $\theta_p$, is shown for the cathode (b) and for the anode (c). The impedance of the individual process is inversely proportional to the area coverage $\theta_p$ and the activation energy of the process $\delta G_p$ (more coverage, less impedance)

Fig. 2.7c shows a typical two-electrode voltage trace wherein the shaded regions indicate the dominant reaction pathways at the anode (above the trace) and the cathode (below the trace). The transition regions between the pathways are left unshaded. [7]

A more detailed explanation of the traces and the morphology changes can be made using this model. The Lithium surfaces are initially pristine, each with an SEI layer that forms upon contact with the liquid electrolyte.

### 2.5.3. MORPHOLOGY EVOLUTION DURING THE FIRST HALF CYCLE

During the first half-cycle, the top electrode (undergoing electrodissolution, not in view) has no previous deposits, and therefore the only mode of dissolution is pitting. On the bottom electrode, mossy deposits are formed at random locations. Fresh nucleation requires overcoming of an activation barrier, and in comparison, the kinetics of growth on the random deposits already formed requires lower energy.Therefore, once the initial mossy deposits nucleate, the dominant reaction pathway at the cathode changes from fresh deposition to growth on top of these deposits. As the area fraction of the growing

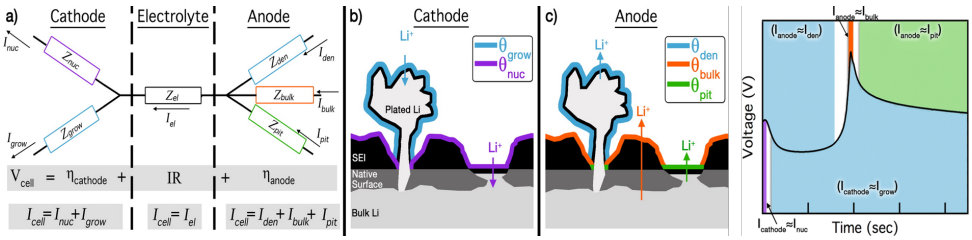


Figure 2.7: The Impedance Pathway Model proposed by Dasgupta et. al. to describe the deposition mechanism of Lithium. a) The overall impedance as a network of individual impedances corresponding to each component, b) and c) the area coverage terms with respect to the cathode and the anode, d) The typical voltage trace produced for a Lithium anode, with coloured regions depicting the dominant modes of current at those periods. [7]

deposits increases, the impedance associated with mossy growth $Z_{grow}$ keeps dropping, such that $I_{grow}$>$I_{nuc}$.

The initial drop in voltage is mainly due to the decrease in overpotential following the nucleation at the bottom electrode, which is followed by the change in impedance paths (fresh from nucleation to growth) and thereafter, the increase in the area coverage of the mossy deposits. In comparison, the pitting on the top electrode contributes a lot lower to the voltage trace.

### 2.5.4. MORPHOLOGY EVOLUTION DURING THE SECOND HALF CYCLE

On switching polarity, with mossy deposits and bulk Lithium both existing on the electrode to be stripped, Li dissolution occurs mainly from the mossy deposits because $\delta G_{den}$< $\delta G_{bulk}$. A maximum in the cell voltage is obtained, but this is largely due to the activation barrier for the initial nucleation on the top electrode (not in view).

Further, the cell overpotential drops to a minimum, which corresponds to a change in reaction pathways from fresh nucleation to growth on top of the new deposits on the top electrode, owing to the kinetics of growth being relatively faster.

Once the active Li in the mossy deposits on the bottom electrode starts depleting, $\theta_{den}$ decreases and the impedance increases, causing an increase in the cell voltage. As $\theta_{den}$ tends to zero, stripping of Li from the bulk becomes favourable, and a maximum in cell voltage occurs. With dissolution from the bulk, the dominant process at the bottom electrode is kinetically slow and a kinetically fast mossy growth is dominant at the top electrode. Therefore, the largest contribution to the overpotential is from the bottom electrode as this point. Further, a second decrease in the voltage trace is observed, owing to the change in the dominant mode of dissolution to pitting from the bottom electrode.

$\theta_{pit}$ gradually increases, as $\delta G_{pit}$< $\delta G_{bulk}$. At this point, the dominant deposition mode is mossy growth and the dissolution mode is stripping from the pits. As $\theta_{pit}$ and $\theta_{grow}$ keep increasing, the cell voltage keeps decreasing.

While the impedance pathway model proposed by Dasgupta et al. [7] has not been rigorously used in the following study, video recording the morphology evolution and correlating them to the voltage traces has been done for deposition studies in both Zinc and Lithium based systems.

## 2.6. POLYMER ELECTROLYTES

Polymer based electrolytes, particularly gel-polymer electrolytes (gelled with liquid electrolyte) have already been employed in rechargeable batteries. A lot of research is also being dedicated towards achieving protective polymer coatings for metal anodes. This study specifically deals with the application of polymer electrolytes as coatings on metal anodes, and therefore, it is important to understand their working principle and obtain insights into the various material properties crucial for their functioning.

### 2.6.1. THE CONDUCTION MECHANISM

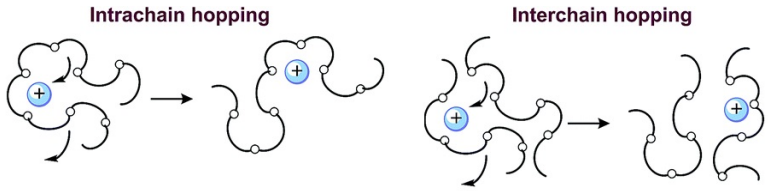


Figure 2.8: The two modes of cation conduction in PEO, as proposed by Xue et. al. [8]

While polymer electrolytes can be technically grouped under solid electrolytes, their ion transport mechanism is quite different from that of the inorganic materials commonly referred to as the solid state electrolytes. In polymer electrolytes, the polymeric host material serves as the medium of ionic transport, and the chain segmental motions and rearrangements of this host material play their part in the overall ion transport, as shown in Fig. 2.8. In contrast, ions are conducted through crystal defects in the case of inorganic solid electrolytes. Unlike the polymeric hosts, these sites are fixed.

When gelled with liquid electrolytes, the composite electrolyte is referred to as a gel-polymer electrolyte, and when used without the liquid electrolytes, they are referred to as solid polymer electrolytes. In both these cases, A Li based salt serves the source of $Li^+$ ions for conduction. [35]

### 2.6.2. CHARACTERISTICS OF A GOOD POLYMER ELECTROLYTE

The polymeric host materials would have to meet several requirements in order to function as a good electrolyte. A high ionic conductivity is a must for any polymer electrolyte and this value is greatly influenced by the segmental motions of polymer chain. This, in turn, depends on the glass transition temperature, below which the ionic conductivity drops drastically. It is at this temperature that the material undergoes a transition from amorphous phase to a crystalline phase. It is ideal to have a relatively low glass transition temperature.[36] Therefore, copolymers are sometimes added to the polymer chain to reduce the degree of crystallinity. PVDF-HFP is one such example, where the HFP parts helps in reducing the crystallinity. [37]

In addition, the presence of groups promoting easy dissolution of the salt (to give $Li^+$ ions) also improves the conductivity. [36] For example, the presence of (-C-F-) groups, known to be strongly electron withdrawing, ensure a high dielectric constant (9.4-10.6) and easy dissociation of salts in the case of PVDF-HFP. [37]

Stability of the polymer in all aspects: chemical, electrochemical, thermal and mechanical - is crucial for a good polymer electrolyte. A wide electrochemical window, a high degradation temperature, and a high mechanical strength of the order of Giga Pascals are all desired of a good polymer electrolyte. The flexibility of the polymer is also important as in the case of the SEI layers, with elastic deformations preferred over plastic deformations. [36]

Further, a good polymer electrolyte is also expected to have a good interfacial contact (and therefore, low interfacial resistance) with the electrodes, particularly the Li metal anode. Another important aspect that decides the lifetime of the Li metal and the battery itself is the Lithium transference number, defined as the fraction of the total current carried by the $Li^+$ ions in a system. This number should ideally be close to 1, as a high transference number would imply that accumulation of negative charge carriers would occur on one side of the electrolyte window, giving rise to space charge layers that accelerate the formation of dendrites.

While bulkier salt anions are beneficial in the sense that they dissociate easily (low dissociation barrier), it is desirable to immobilize these anions such that only $Li^+$ ions are moving through the system and contributing to the current. The quest for such materials has resulted in a widespread interest in single ion conducting ionomers, discussed in detail in section 2.8.

## 2.7. POLYMER ELECTROLYTES AS PROTECTIVE COATING (ARTIFICIAL SEI) ON LI METAL

The favourable properties of polymer electrolytes in terms of compatibility with liquid electrolytes and the ability to mechanically resist dendrite growth has led to research over its potential application as an artificial SEI in liquid electrolyte (LE) based batteries. While the porous nature of the polymer backbone ensures that a certain amount of liquid electrolyte is absorbed by the polymer to ensure high $Li^+$ conductivity through the polymer (similar to GPEs), [36] these polymer layers come into contact with the LE only during the operation of the cell (unlike when being used a GPE where the entire polymer film has been in contact with the LE during soaking), and little to no LE makes direct contact with the Li metal. The overall conductivity of the system can also be higher than that of a GPE based system, with LE still being the dominant medium of transport. Compared to pure LE based systems, this system has a polymer layer, although at a much lower thickness as compared to GPEs, offering sufficient mechanical resistance to dendrite formation, without compromising much on the overall conductivity.

While using polymers as protective coatings in conjunction with liquid electrolytes, it is important to consider several factors to ensure optimal functioning of the coating, the most important ones being the polymer chemistry and the thickness of the coating. [9]

### 2.7.1. EFFECT OF POLYMER CHEMISTRY ON THE ELECTROCHEMICAL PERFORMANCE

At similar thicknesses, the polymer chemistry plays a major role in deciding the type and size of Lithium deposits. Depending on the properties of polymers, these coatings can

reduce dendrite formation either by mechanically suppressing the dendrites with a high modulus or by improving the homogeneity of Li deposition through surface effects. [9]

Through a series of experiments with different polymer coatings at different thicknesses, Lopez et. al. identified dielectric constant and surface energy as the two key factors deciding the Li deposit size. Polymers with a low surface energy of their own generally resulted in larger deposits and smaller surface areas. Low surface energy of polymers implies lower interaction between the polymer layer and the Lithium surface, and thereby and an increase in the interfacial energy. Further, high dielectric constant polymers generally resulted in higher exchange currents and decreased overpotentials at a certain current density and therefore larger individual Lithium deposits. For example, while a PEO coating (dielectric constant around 5) resulted in small diameter (in 100s of nm), rod like shaped Li deposits, PVDF (dielectric constant = 15) resulted in larger (in 1000s of nm), hemispherical deposits. [9]

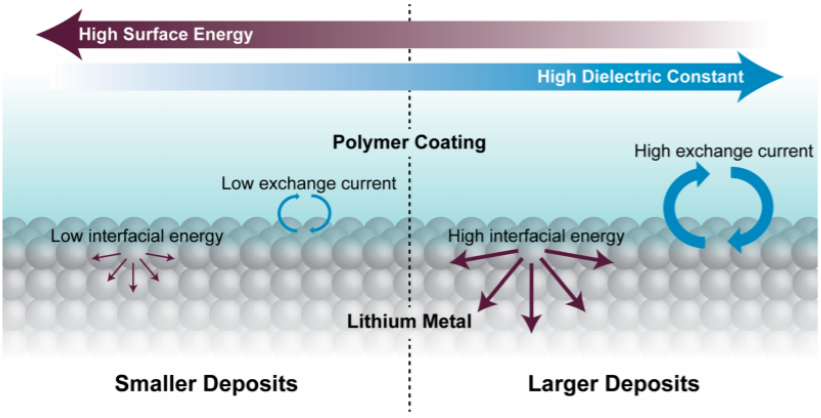


Figure 2.9: Effect of Polymer coating chemistry on the individual deposit size [9]

In the case of polymer coatings, their compatibility and interaction with the liquid electrolyte in the battery environment is also crucial for the battery lifetime. Different polymers swell in liquid electrolytes to different degrees, thereby altering the amount of liquid electrolyte directly coming in contact with Lithium, while a few polymers, depending on their composition, could react with the liquid electrolytes over time, resulting in degradation of the polymer coating, loss of electrolyte and thereby a decrease in the battery performance. [9]

### 2.7.2. EFFECT OF COATING THICKNESS ON THE ELECTROCHEMICAL PERFORMANCE

Further, the thickness of the polymer coating was also found to play a crucial role in determining the nature of Li deposits, and also that the optimum thickness of the polymer is unique for each polymer material.

Lopez et al. tried to optimize the thickness for several polymers by spincoating them on Copper at different thicknesses and then Lithiating them at 1 mA/cm$^2$. [9] In the case

of PVDF for instance, while a thickness of about 0.9 microns resulted in uniform deposition of Li, thicknesses below this value resulted in patchy growth with round shaped Li deposits as in the case of bare Copper, implying that the coating was too thin to alter the spatial distribution of the Li metal. [9]

At higher thicknesses of 3 microns and above, two different modes of Li deposition were observed. While majority of the deposition happened under the polymer coating, there were also smaller deposits that grew through the pinholes in the film. This suggests that the coating is too thick to allow for uniform deposition. Although the nucleation does begin below the coating, as the Li particles increase in size, they start growing through the defects where the impedance to Li transport is lower.

At even higher thicknesses, the impedance offered by the polymer layer increases even further, and now the deposition occurs solely through pinholes and defects, eventually leading to dendrites. It is therefore, important to optimize the coating thickness. Further, it was also found the optimum thickness of coating was unique for each polymer material and was strongly a function of its ionic conductivity. [9]

While these experiments were carried out for Copper substrate, getting these coatings to work at similar thicknesses for bare Li metal, which has a much higher degree of roughness, can be quite challenging. Commercially supplied Li also usually contains native oxide and nitride layers, As an extension to these findings, it could also be suggested that the surface of the Li metal itself needs to be uniform enough so that the possibilities of pinholes developing are greatly reduced.

### 2.7.3. PEO AND PVDF

Two of the most commonly used polymers for both polymer electrolyte and protective coating applications are Polyethylene Oxide (PEO) and polyvinylidene Fluoride (PVDF). PEO has a low glass transition temperature of -67 $^{o}$C. It has a donor ether group in the Polymer backbone (-$CH_2$ - $CH_2$ - O-) which is favourable for coordination with cations. It also has a high dielectric constant value (around 5) which helps in improving salt dissociation and thereby ionic conductivity. However, PEO is semi-crystalline at room temperature and as a result, its ionic conductivity at room temperature is quite low (of the order of $10^{-6}$ S/cm). [38]

Several approaches have been tried to improve the conductivity of PEO, the most common one being the addition of nanofillers, which will be discussed in section 2.9.2. For applications as a sole polymer electrolyte, use of plasticizers (such as Succinonitrile) with high dielectric constant and relatively low melting points, is also an option to increase the conductivity. [38]

PVDF is also a semi-crystalline polymer, but with a high Fluorine content (59.4 wt%). The arrangement of $CH_2$ and $CF_2$ group along its polymer chain results in its excellent mechanical, thermal and chemical stability and its strongly hydrophobic nature. The strong electronegativity of F atoms contributes to its high dielectric constant (about 15), aiding in easy salt dissociation, while the high bond dissociation energy of the -CF bond results in the aforementioned all-round stability of the material.

The high dielectric constant results in a potential gradient between the film and the Li substrate, and this helps in uniform deposition of Li below the film. [39]

PVDF has already been successfully employed as a protective coating on Li by many

researchers. [39] [40]. It is also possible to obtain a uniform inorganic (LiF) SEI layer when PVDF is used with certain solvents. One such approach involves coating PVDF as a solution in DMF, and this was shown to result in a uniform layer of LiF on Li. [40]

## 2.8. IONOMERS: SINGLE ION CONDUCTING POLYMERS AND THEIR APPLICATIONS IN BATTERIES

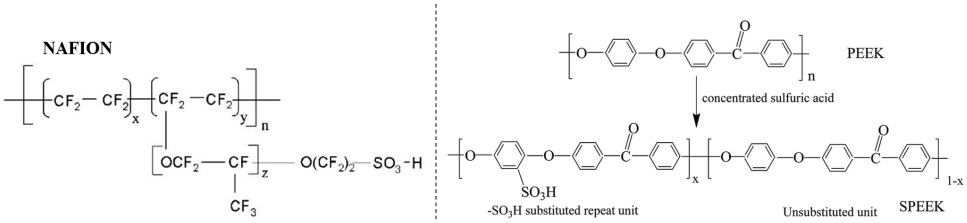


Figure 2.10: Chemical structures of Nafion (left) [10] and SPEEK (right) [11]

As already discussed, having a low transference number generally results in a build up of anions at one of the electrodes, resulting in concentration polarization that aids the formation of dendrites. For this reason, the free movement of anions needs to be reduced or eliminated. This is possible in the case of ionomers, where anionic groups are covalently bonded to the polymeric backbone, thus making the compound single ion conducting. [36]

Ionomers, especially those with sulfonate groups as the immobilized anions have an additional significance in the case of Li-S batteries, as these compounds have been demonstrated to prevent polysulfide (also negatively charged) diffusion onto the Li metal anode. Therefore, ionomers that can prevent both dendrite formation and polysulfide diffusion could be the ideal solution to improving the lifetime of a Li-S battery.

### 2.8.1. NAFION

One of the most commonly researched ionomers for Battery applications is Nafion (trademark of DuPont inc.). Like PVDF, Nafion is a highly fluorinated compound and the arrangement of -CF groups along the polymer chain imparts it with excellent chemical, thermal and mechanical properties. Several researchers have explored the possibility of using Nafion based compounds either as a coating on Li or as an interlayer that reduces polysulfide diffusion and suppresses dendrite formation. [41] [23] [24] [42] While Nafion is semicrystalline and has a low ionic conductivity (about $4x10^{-6}$ S/cm) at room temperature, improvements have been achieved by either Lithiating the material, adding nanofillers, blending with more conductive polymers or by combining two or more such modifications.

Further, with Nafion being a patented material and also a highly fluorinated one, scaling up its use in batteries can have major implications on the cost effectiveness and the eco-friendliness of these products. It is therefore, desired to have a cheaper compound with similar all-round properties, but with a lesser fluorine content.

### 2.8.2. SULFONATED POLY ETHER ETHER KETONE (SPEEK)

Sulfonated Poly Ether Ether Ketone (SPEEK) has often been touted as an alternative to Nafion, not just for Fuel cell applications but also battery applications owing to its similar mechanical, chemical and thermal properties.

SPEEK is obtained by the reaction of Poly Ether Ether Ketone (PEEK) with Sulphuric acid, with the residence time of the reaction deciding the degree of sulfonation (DS). In this first-order electrophilic substitution reaction, an -$SO_3H$ group is attached to one of the four chemically equivalent positions of the phenyl ring as shown in Fig. 2.10. Degree of Sulfonation (DS) is a percentage measure of the monomer units of PEEK that have undergone sulfonation. [43]

The sulfonate groups attached to PEEK have an electronegative oxygen atom and this helps the polymer to interact with Lithium salts. Like most polymer electrolytes, SPEEK is semicrystalline at room temperature and has a glass transition temperature range of 135-220 $^oC$ depending on the degree of sulfonation. [44][45][43]

Having the right value of DS is crucial for the optimal performance of the polymer. It has been observed that the addition of Sulfonate groups to PEEK results in diffraction peak broadening, which suggests a decrease in crystallinity upon sulfonation. [43] At the same time, Sulfonation resulted in a material with higher glass transition temperature than that of PEEK in most studies [44][45][43], and Tg is generally expected to drop with a decrease in crystallinity. This suggests that the increase in Tg is perhaps due to strong interaction of the Sulfonate groups with other sulfonate groups (Hydrogen bonding) and/or with the ketone groups of the polymer. [43]

Further, SPEEK tends to get more hygroscopic with increase in DS with more channels available for water/moisture uptake, resulting in membrane instability, particularly for Li battery based applications. However, having a DS lower than 50% severely affects the ionic conductivity of the polymer as there are not enough channels to conduct $Li^+$ ions. Optimizing the DS to the performance requirements is therefore, a must. [43]

Dimethyl Sulfoxide (DMSO) is the most commonly used solvent for SPEEK. The residual DMSO left in the SPEEK coatings/membranes also serves as a plasticizer; it increases the amorphous fraction of the polymer and thereby the ionic conductivity. It is also a common practice to lithiate the ionomer before it can be coated/used in Lithium based batteries. The presence of $Li^+$ in place of $H^+$ in the polymer has been shown to decrease the Tg and increase the ionic conductivity.

## 2.9. COMPOSITE POLYMER COATINGS

Poor conductivity of polymer electrolytes has been a major hurdle in their commercialization. While there have been several approaches to increasing the conductivity of polymers at room temperatures, one must realize that these improvements must not arrive at the cost of significant reduction in the mechanical integrity of these polymers, which defeats the very purpose of using polymer based coating to mechanically resist dendrite formation in the first place. While having a liquid plasticizer might work well for polymer electrolytes in terms of reducing the crystallinity and increasing the conductivity, such an approach is not recommended when the polymer is to be used as a protective coating on Lithium. The same goes for copolymerization with amorphous units, provided the degree of copolymerization negatively impacts the mechanical strength of the

polymer. [46]

### 2.9.1. WITH CERAMIC COATED SEPARATORS

Inorganic ceramics such as $TiO_2$ and $Al_2O_3$ and their positive effects on Li anode performance have been studied extensively. $Al_2O_3$ for example, is an excellent passivator of electrons and has a bandgap of 9.9eV. The slow electron transfer rate greatly reduces the LE decomposition and active Li consumption. [33] While these ceramics have been incorporated as ALD based coatings on Li, ceramic coated separators when used in conjunction with polymer based coatings can display a similar effect. Tu et al. were able to significantly improve the lifetime of Li metal anode by combining a thin coating of Lithiated Nafion on Li with an $Al_2O_3$ based separator. [42]

### 2.9.2. INORGANIC NANOFILLERS

Inorganic ceramics such as $TiO_2$ and $Al_2O_3$, when nanosized, can also be used as fillers in the matrix of the polymer to boost the conductivity. According to Xue et al., addition of fillers into the polymer matrix increases the amorphous phase of the polymer and suppresses recrystallization, resulting in a conductivity increase of 1-2 orders. The reduction in mechanical properties due to loss of crystallinity is compensated for by these nanosized fillers; their interaction with the polymer matrix contributes positively to the mechanical properties. [8] However, the fillers provide incremental conductivity only upto a certain concentration, exceeding which would result in decrease of conductivity due to blocking effects. In the case of PEO, this value is around 10 wt%. [47]

Inorganic nanofillers have also been used with ionomers. Jiang et. al. used 1 wt% nanoparticle $TiO_2$ as fillers in Nafion coatings on Li, resulting in improvements in both the conductivity (10 times) and the mechanical strength (2 times). According to them, the dispersed $TiO_2$ alters the shape of the ionic cluster and increases the density of the $-SO_3^-$ sites. However, concentrations beyond 1 wt% resulted in lower conductivities, which is possibly due to the aggregation of $TiO_2$ particles that blocks the transport of $Li^+$ ions. The improvement in mechanical properties has been attributed to the dynamic interactions between the fillers and the matrix that reduce the mobility of the main chain. [41]

### 2.9.3. LITHIUM ACTIVE SALTS AND SOLID ELECTROLYTE COMPOSITES

While Lithium active salts such as LiTFSI are commonly found dissolved in polymeric hosts such as PEO, they can also be used in ionomers like SPEEK. LiTFSI is perhaps the mostly commonly used Li salt, thanks to the bulky anion with a strong electron withdrawing nature, which helps in easy dissociation of the salt to generate a high amount of $Li^+$ ions in the polymer electrolyte/coating. Further, the flexibility of the TFSI anion results in a plasticizing effect, further improving the conductivity. [43] [46]

However, the conductivity improvement offered by the addition of TFSI peaks at a certain wt% and then drops. For SPEEK, this value was found to be around 20 wt%. The conductivity improved by nearly 1 order at room temperature and the membrane was found to be thermally stable upto 100 $^oC$. [43]

Similar to nanosized Li-inactive inorganic fillers, Li-active solid electrolytes can also be introduced into the polymer matrix to boost the conductivity. With a higher particle

size these particles can result in different modes of $Li^+$ conduction at different weight concentrations. At very low concentrations (<5 wt%), the particles behave similar to Li-inactive nanosized fillers in reducing the crystallinity and the dominant mode of conduction is still through the polymer. At certain higher concentrations, however, the solid electrolyte particles connect to form a percolated network, and now the dominant mode of conduction is through the solid electrolyte, and the composite electrolyte is now effectively a solid electrolyte bound together by the polymer. However, this results in a blockage of $Li^+$ conduction through the PEO pathway, and the overall conductivity might actually turn out to be lesser, as observed by Zheng et. al. [47]

### 2.9.4. POLYMER BLENDS

Single ion conducting ionomers offer additional benefits such as higher transference number and prevention of polysulfide diffusion, in comparison to conventional polymer electrolytes. However, the ionic conductivity of ionomers tend to be lower than that of the conventional polymer electrolytes. Therefore, the idea of blending the two types of polymers to obtain dual functional polymer coatings has gained traction in the recent years.

Luo et. al. combined Lithiated Nafion with PVDF to obtain a dual functional polymer that acted both as a protective layer to suppress dendrite formation on Li and as an interlayer to prevent PS diffusion into the Li metal anode. In addition to improving the ionic conductivity, blending Nafion with PVDF greatly reduced the degree of swelling of the polymer in liquid electrolyte and thus resulted in improved mechanical strength. It was concluded that PVDF entrapped the Nafion molecules within the coating layer by entanglement between the two polymers, which caused a reduction in swelling. The blend polymer provided a stable interface with much lesser overpotential at the same thickness in comparison to pure Nafion, and also a much better long term electrochemical performance. When used in a full Li-S cell, the blend polymer coated Li displayed much lesser leakage current (a measure of polysulfide diffusivity) than bare Li. [24]

Therefore, blending other ionomers such as Lithiated SPEEK with PVDF could certainly be a possibility to produce similar coatings. However, the miscibility of the two polymers at different different concentrations and also at different degrees of sulfonation of SPEEK need to be considered. He et al. studied the miscibility of SPEEK and PVDF based on the two aforementioned parameters and found that the best miscibility was found in those membranes that either had a low DS or a low wt% of one of the components. [48]

At DS values below 50%, the two polymers were miscible at all concentrations. PVDF is hydrophobic in nature and SPEEK gets more hydrophilic with increasing DS. Therefore, at higher DS values, intermolecular interactions between the two components weakens, resulting in immiscibility over a range of concentrations. The immiscibility pattern generally observed was that of 'islands' of the lower concentration phase dispersed in a sea of the higher concentration phase. Depending on the relative concentration, the islands either change in size or in density. This immiscibility disappears at very low or very high concentrations of one of the components. [48]

# 3

# MATERIALS AND METHODS

In this chapter, the procedures followed in the preparation of samples, the techniques used to characterize these samples and the techniques used to measure the electrochemical performance of the samples have been described. For the various experimental techniques used, a brief introduction to the working mechanism has been provided, followed by a description of the experimental configuration used in the study.

## 3.1. PREPARATION OF ELECTRODES AND ELECTROLYTE FOR ZINC-ZINC SYMMETRIC CELLS

The experiments were performed using Zn foils (Alfa Aesar, 250 $\mu$m thickness and 99.98 % purity) and 10 $\mu$m Copper foils were used for experiments involving electrodeposition on Cu substrate. Prior to experiments, the Zn foils were subjected to a mechanical cleaning process to remove the oxide layers and homogenize the surface. The metal surface was subjected to mechanical grinding using a SiC paper (Struers, Grit size FEPA P #2000).

For galvanostatic experiments using the KF-type test cell, the separator used was Glass Microfiber (GE Whatman Grade GF 6, 25 mm diameter, mm thickness) The required concentrations of $ZnSO_4$ were prepared by dissolving $ZnSO_4$ heptahydrate (Sigma Aldrich, 99 % pure) in deionised water.

## 3.2. PREPARATION OF LITHIATED-SPEEK AND PVDF SOLUTIONS

Sulfonated PEEK (Degree of Sulfonation = 85%) was prepared by subjecting PEEK powder (Victrex inc.) to sulfonation using conc. $H_2SO_4$ for a determined amount of time. For every batch of Li-SPEEK, about 150 mg of SPEEK was first dissolved in DMSO (100mg/1ml) and then cast into a film on a glass substrate. The vacuum dried film (for about 12 hrs) was then subjected to Lithiation by immersing it in a 2M $LiOH.H_2O$ solution at 80 $^oC$ for 12 hours with stirring. The film was then rinsed with running DM water to get rid of all the LiOH powder remaining on the film and then vacuum dried for 12 hours.

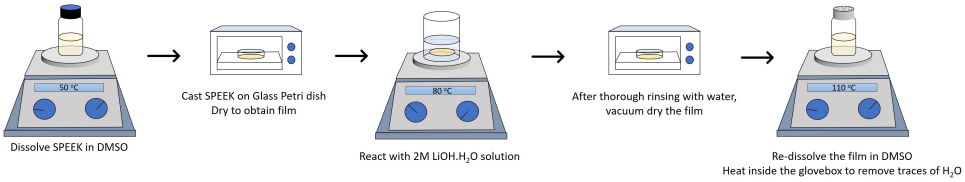


Figure 3.1: Stepwise procedure for the conversion of SPEEK to Li-SPEEK

The obtained Li-SPEEK film was then dissolved in DMSO at three different concentrations, 25mg/ml, 50 mg/ml and 100 mg/ml. Lower concentrations, if required, were obtained by further diluting these solutions with DMSO. The solutions were kept on stirring for 6 hours to ensure proper mixing.

PVDF (HSV900, Kynar) was dissolved in DMSO in a ratio of 50mg/ml (5 wt%) and stirred until a viscous solution was obtained. The solution was kept on stirring for another 24 hours to ensure uniform mixing.

## 3.3. PREPARATION OF LI-SPEEK WITH 1 WT% NANO-$TiO_2$

5 mg of $TiO_2$ nanopowder (<25nm, Sigma Aldrich) was added to 2 ml of DMSO. The solution was placed in an ultrasonic bath for 20 minutes to ensure proper dispersion of $TiO_2$ in DMSO. 0.4 ml of this solution was added to 2 ml of 50 mg/ml Li-SPEEK solution in DMSO, such that the $TiO_2$:Li-SPEEK weight ratio is now 1:100. This solution was again placed in an ultrasonic bath for 20 minutes to ensure uniform dispersion of $TiO_2$ in the Li-SPEEK solution.

## 3.4. POLYMER COATINGS ON LITHIUM

Pre punched Lithium foils (Sigma Aldrich) of 15.4 mm diameter were used. The Li foils were subjected to polishing until the surface was extremely shiny and visibly free of the native layer. These cleaned Li foils were flattened prior to use with the help of clean glass substrates. The thickness of the coating on Li was to be controlled by controlling the solvent concentration as required.

The polymer based solutions in DMSO were first heated at 110 $^{o}$C for 5-6 hours inside the Ar-glovebox to get rid of any traces of water present.

The polymer solutions were then coated onto Li using two different methods. The first method was drop coating, i.e. dropping the solution onto Li and then spreading it evenly using a fine rod, while the other method was to soak a Celgard separator in the solution, press it onto the Li foil for about 5 seconds and then slowly remove it. The coated Li foils were first heated at 60 $^{o}$C for 1 hour on the heater inside the Ar glovebox and then vacuum dried at 70 $^{o}$C inside the vacuum antechamber for 12 hours.

While it was impossible to measure the thickness of Li-SPEEK coating on Lithium, to get a rough estimate of the thickness of these coatings, Li-SPEEK was coated using a similar procedure(similar amount of solution on similar area) for Copper, and using a micrometer, the average thickness of these coatings was found to be in the range of 2-3 micron for concentration of 10 mg Li-SPEEK/ml DMSO.

## 3.5. POLYMER COATINGS ON COPPER

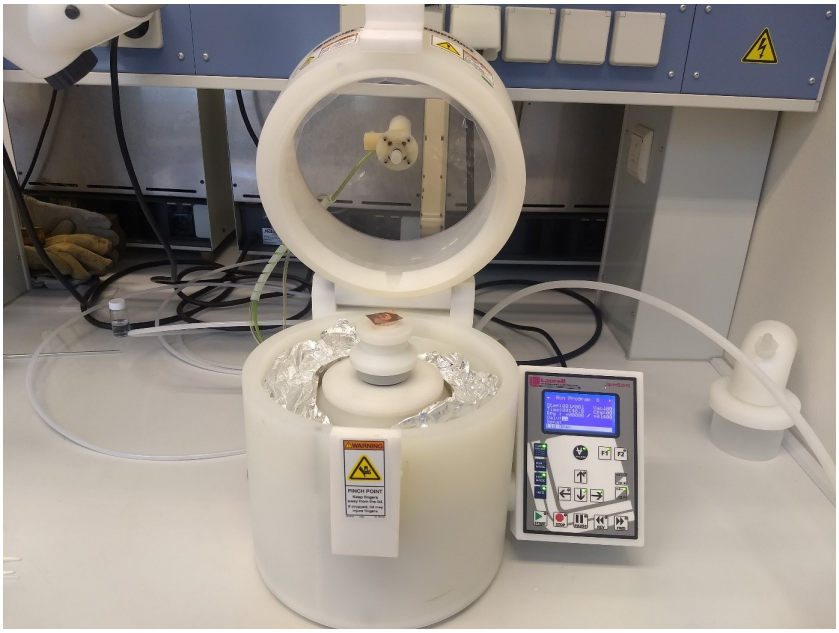


Figure 3.2: Spincoater used for Li-SPEEK and PVDF coatings on Copper

Thin, uniform, polymer coatings on Cu were achieved using the spincoating technique. The copper foils (50 micron thick) were first cleaned using 0.1M Oxalic acid to remove the native oxide layer and cleaned with acetone to remove the traces of acid. The clean copper foils were spincoated (Laurell WS-650 Spincoater) with the solutions at an RPM of 1400 for 50s. The coated foils were then vacuum dried at room temperature for 48 hours. The resulting coatings were then analyzed using AFM/SEM to observe the topology and homogeneity of coating.

## 3.6. SETUP FOR OPERANDO MICROSCOPY

The electrochemical test–cum-visualization cell used for operando microscopy, referred to hereafter as the 'Optical Cell', was designed as shown in Fig.3.3. The setup consists of the following parts:

**Vessel and the primary parts:** The vessel provides the volume to hold the primary parts of the cell and also acts as a reservoir for the liquid battery. The primary parts of the cell are the metal blocks made of stainless steel that act as current collectors, the electrodes to be tested that are placed on either of the metal blocks, and the wedge shaped spacer (1 mm thick, wedge cut = 5 x 10 mm) that forms the electrolyte window between the two electrodes. The entire vessel is filled with the liquid electrolyte of interest. The entire setup is pressed and held together by the steel springs, which also increase the pressure of operation and ensure proper electrical connectivity.

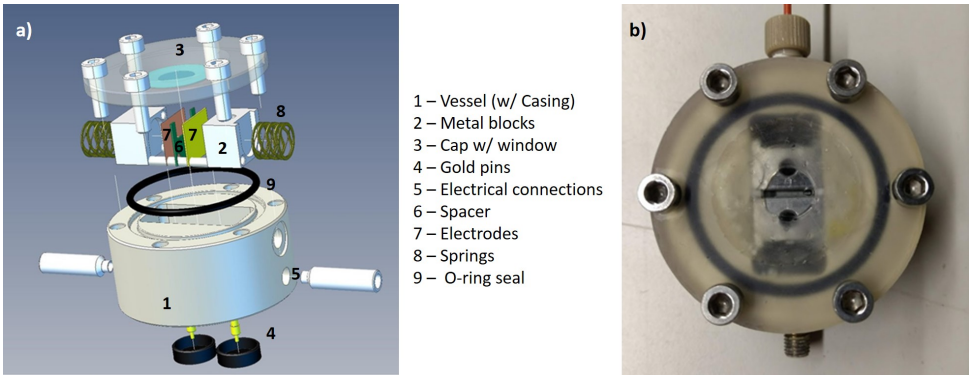


Figure 3.3: Custom-made Optical Cell used for the Operando Microscopy Experiments. a) Construction overview of the cell b) Top view of the assembled cell

**Top cover with viewing glass:** The cell is covered with a 3D printed plastic cover on top, which also has a viewing glass at the centre such that the electrodes and the electrolyte window are in view when subjected to microscopy. After the cell is assembled and the vessel is filled to the brim with the electrolyte, the cover is carefully placed on top such that there are no trapped air bubbles that can have a negative impact on both the operation of the cell and the quality of the microscopy. The screws are tightened such that the tightening of one screw is followed by the tightening of the screw directly opposite to it. This is done in order to ensure even tightening of the cell, the prevention of any possible electrolyte leakage and also to avoid mechanical failure of the glass due to uneven pressure applied. An O-ring seal is used beneath the cover to render the setup airtight.

**Electrical connections:** When assembled, the metal blocks are in contact with the gold plated pins at the bottom of the vessel, which are further connected to the external connection slots. The cell is currently a two electrode setup, which means the terminal for the reference electrode is coupled to that of the counter electrode.

The assembled optical cell was placed under the digital optical microscope (Dino-Lite Edge, 20x-220x, 5 MP camera). This was connected to a PC-controlled Metrohm Autolab system for galvanostatic cycling and other electrochemical techniques. The digital camera was also connected to a PC for capturing and controlling the live video.

Unless stated otherwise, all galvanostatic cycling experiments were performed at a current density of 5 mA/cm$^2$ for a minimum of 2 cycles, with the duration of each half cycle being 15 minutes (1.25 mAh/cm$^2$) with a time gap of 15s between the half cycles.

## 3.7. ELECTRICAL MEASUREMENTS WITH THE OPTICAL CELL AND THE KF-TEST CELL

The Zn-Zn symmetric optical cell was subjected to different Galvanostatic measurements, with currents ranging from 1 mA to 120 mA, for different deposition periods and for different number of cycles. In addition to the current density, other factors known to in-

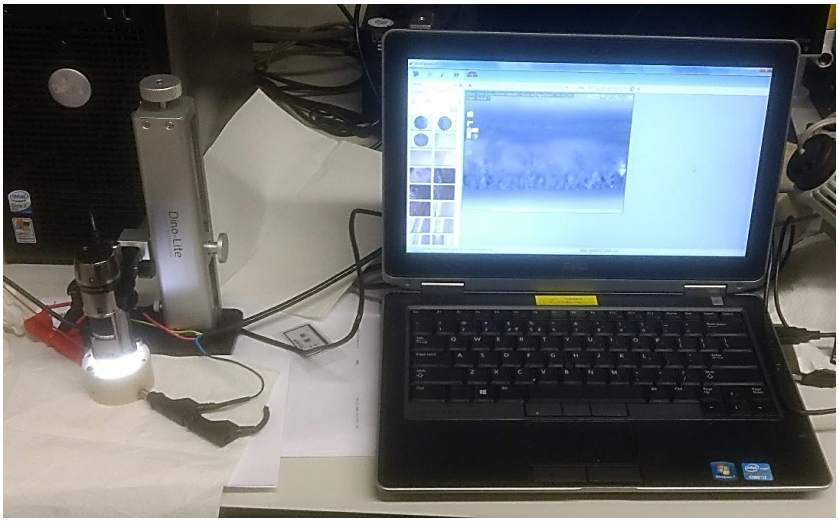


Figure 3.4: The Operando Microscopy Setup (Galvanostat not in the picture) to study the electrochemical behaviour of metal anodes

fluence the deposition morphology, namely the salt concentration, surface roughness, temperature, substrate type and additives were also altered.

Further, selected galvanostatic measurements were also performed on the using the KF- lab cell in a MACCOR 4420, These experiments were done in order to compare and correlate the voltage traces obtained with the optical cell to those obtained under more commonly used cell architecture types like the coin cells.

## 3.8. ELECTROCHEMICAL IMPEDANCE SPECTROSCOPY

Electrochemical Impedance Spectroscopy or EIS is a technique used to determine the nature and measure the quantity of the overall impedance (and its components) of an electrochemical system. This technique involves application of a small potential or current perturbation, sinusoidal in nature and at a certain frequency to measure the impedance at that frequency. This measurement is repeated over a range of frequencies, and the resulting data is plotted and analysed to obtain the overall impedance characteristics of the system. ([12])

EIS Data is generally presented either as a Bode plot (Frequency vs Modulus of Impedance) or as a Nyquist plot (Real and imaginary parts of the impedance plotted on a complex plane). As one can observe from Fig. 3.5b, the Nyquist plot can be roughly divided into two regions, a high frequency region where the ionic transport is kinetic controlled and a low frequency region where it becomes mass transfer controlled. ([12])

Further, the data from the Nyquist plot can be used to model the electrochemical system as a network of electrical circuit elements, each element corresponding to different transport and kinetic characteristics of the system. A typical 'Randles equivalent circuit' of elements is constructed as shown in Fig.3.5b and consists of the following compo-

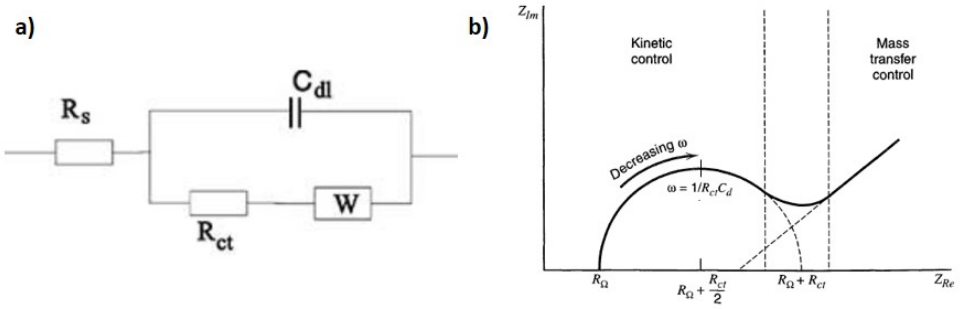


Figure 3.5: a) The simplified Randles circuit for a mixed control system [12] b) Nyquist plot for a mixed control system [13]

nents: The electrolyte resistance ($R_s$), the Double Layer Capacitance ($C_{dl}$), the (kinetic) Charge Transfer Resistance ($R_{ct}$) and the Warburg impedance (W). ([12])

While the Warburg impedance, which gives a measure of the resistance of mass transfer through the system (and thereby the diffusion coefficient) can be ignored under circumstances where the ionic transport is not mass transport limited, it has to be taken into consideration in this study, where the ion transport in dendritic regimes and through polymer coatings is studied, both subject to mass transfer limitations. The overall ionic conductivity $\kappa$ is then given as ([12]):

$$\kappa = \frac{l}{R \cdot A} \tag{3.1}$$

Formula for Warburg impedance, W

$$W = \sigma\omega^{-0.5}(1-j)tanh(\delta(\frac{j\omega}{D})^{0.5}) \tag{3.2}$$

Where l= interelectrode distance, R = overall ionic resistance (i.e. $R_\Omega + R_{ct}$ from Fig. 3.5b), A = area of the electrode, $\sigma$ = Warburg coefficient, $\omega$ = radial frequency, j = unit imaginary number, $\delta$ = Nernst thickness of the diffusion layer , and D = average diffusion coefficient of the diffusing species.

Electrochemical Impedance Spectroscopy was carried out on the optical cell, both at the beginning and the end of galvanostatic measurements, (Frequency range: 0.1 to $10^5$ Hz, Amplitude of signal: 0.01 VRMS ).

## 3.9. POST-MORTEM XRD

X-ray diffraction (XRD) is a non-destructive analytical method used to study the atomic/molecular crystal structure of materials. X-rays with wavelengths in the nanometric range scatter from a material with elementary structures called unit cells at this length scale, and the resulting interference produces a pattern of high and low intensities.

An X-ray beam is directed towards the sample, and the intensity of the scattered rays is measured as a function of the scattering angle $2\theta$, i.e. the angle between the incom-

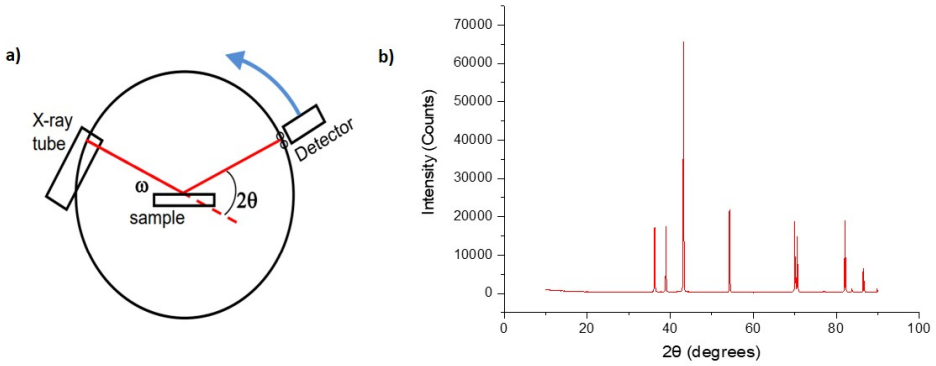


Figure 3.6: a) Schematic arrangement for an XRD measurement [14] b) XRD Spectrum for Zinc metal (source: this work)

ing and outgoing directions. Constructive interference corresponding to peaks in the diffraction pattern are obtained when the Bragg's law is satisfied

$$n\lambda = 2dsin\theta \tag{3.3}$$

Where, n is an integer, $\lambda$ is the wavelength of the x-ray beam and d is the distance between two successive crystal lattice planes. These interplanar distances corresponding to different crystal orientations result in a set of diffraction peaks unique to the material being analyzed. It is possible to identify the different phases in a given material on the basis of these signature patterns observed.([49]). Different phases have different degrees of sensitivity to X-rays and therefore it is not possible to directly estimate the relative amount of each phase in a given material based on their intensities. However, in the case of a single phase material like Zinc, the relative intensities corresponding to different crystal orientations are not always the same and differ based on the morphology (mossy, compact, dendritic etc.). XRD can therefore be a useful tool to distinguish between the different types of morphology observed on Zinc and can complement visual analysis techniques like SEM.

In this study, the crystallographic orientation of the deposits formed on Zn samples (capacity limited, at different current densities) was studied post-cycling using X-Ray Diffraction (PANalytical XPert PRO).

## 3.10. IN SITU TEM AND EX-SITU SEM

With light based microscopy techniques being limited by the degree of resolution only upto the wavelength of light, electron microscope techniques such as Scanning Electron Microscopy (SEM) and Transmission Electron Microscopy (TEM) were used to study the morphology evolution at the nanoscale in the case of Zinc. While both the techniques are electron microscopies, it is important to note the differences between the two. TEM allows the electrons to pass through the specimen, thereby producing a negative image on the fluorescent screen, while SEM is a surface scanning technique wherein a scan involves focusing of the electron beam on the surface and detection of the reflected beam.

The techniques are thus complementary in the type of image produced and the type of information they provide about the analysed material.

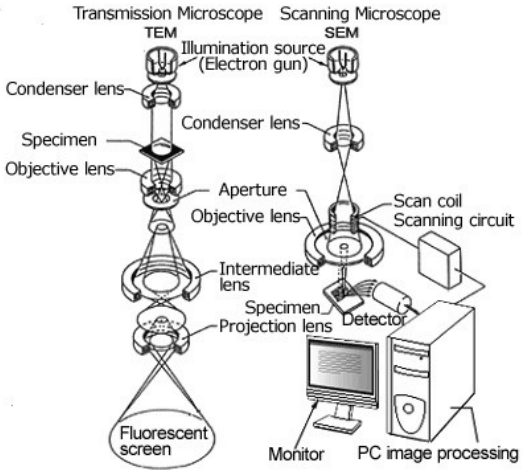


Figure 3.7: Schematic Diagrams for Transmission and Scanning Electron Microscopies [15]

In this study, the samples were subjected to SEM analysis post-cycling(JEOL JSM-IT100 with EDXS) to study the morphology changes. On the other hand, TEM was used for in-situ study of the initial phase of Zinc electrodeposition in the $ZnSO_4$ electrolyte system. A schematic diagram of the experimental setup is shown in Fig. 3.8. Two platinum electrodes were immersed in 0.1 M $ZnSO_4$ solution, with the arrangement enclosed by a 50 nm $Si_3N_4$ layer. A potential scan was performed with -0.2 V and 1V being the lower and upper intervals respectively, with a scan rate of 100 mV/s.

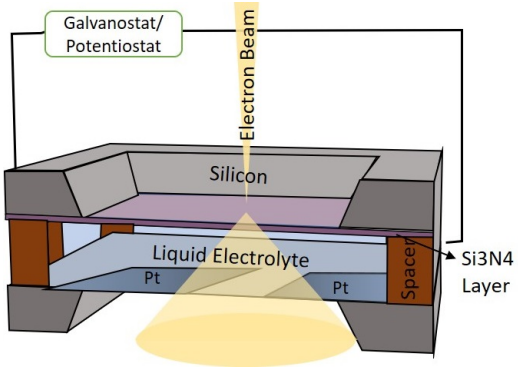


Figure 3.8: Schematic Diagram for the in-situ TEM Setup

# 4

# STUDY OF ELECTROCHEMICAL PERFORMANCE OF ZINC METAL ANODES

This chapter describes the results of a series of experiments carried out to study the electrochemical performance of the Zinc metal anode in a $ZnSO_4$ electrolyte system. The chapter begins with the operando microscopy of a Zn Zn symmetric cell, to develop correlations between the observed morphology changes and the voltage traces for moderate and high currents. Further, a detailed study of the Zinc deposition at different current densities and with changes to different operational parameters is carried out. Time based evolution of Zinc deposits with cycling is also studied. The mechanism of initial Zinc deposition is studied using in-situ TEM. Further, the effect of SPEEK as a protective coating on Zinc is investigated.

## 4.1. OPERANDO MICROSCOPY: CORRELATING VOLTAGE TRACES WITH MORPHOLOGY

A framework to correlate the voltage traces observed during the galvanostatic cycling to the observed morphological changes on the metal anode surface was described by Dasgupta et al.[7] for Lithium metal. In this study, the aforementioned framework has been utilized to correlate the voltage traces with the morphology changes on the Zinc metal anode.

While the current distribution over the Zinc metal in systems with near neutral aqueous electrolytes is much more uniform as compared to Lithium, mainly due to the absence of the non-homogeneous SEI layer, inhomogeneities still exist on the Zinc surface, (even after ensuring a certain degree of smoothness with mechanical grinding) that enable preferential nucleation and growth on these sites. The aforementioned framework can therefore be extended to Zinc in aqueous systems.

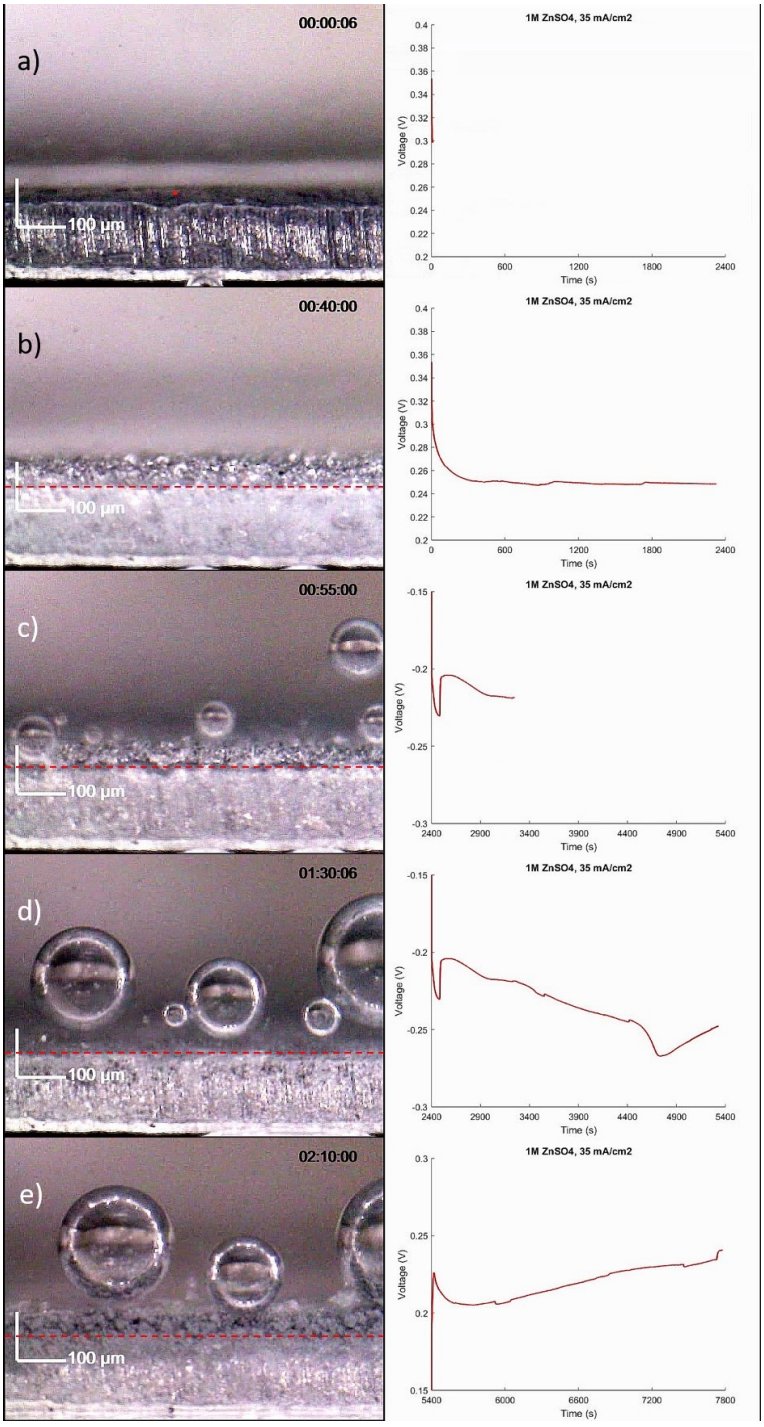


Figure 4.1: Video frames for the Zn-Zn Optical cell cycled at 35 mA/cm$^2$ for 3 half cycles, and the corresponding voltage traces. The compact Zinc deposited in the first half cycle (b) is stripped in the second half cycle, and a transition to stripping from the bulk is marked with a maximum in the voltage trace at around 4750 s(d). Mossy growth is observed during the third half cycle (e) in contrast to the first (b).

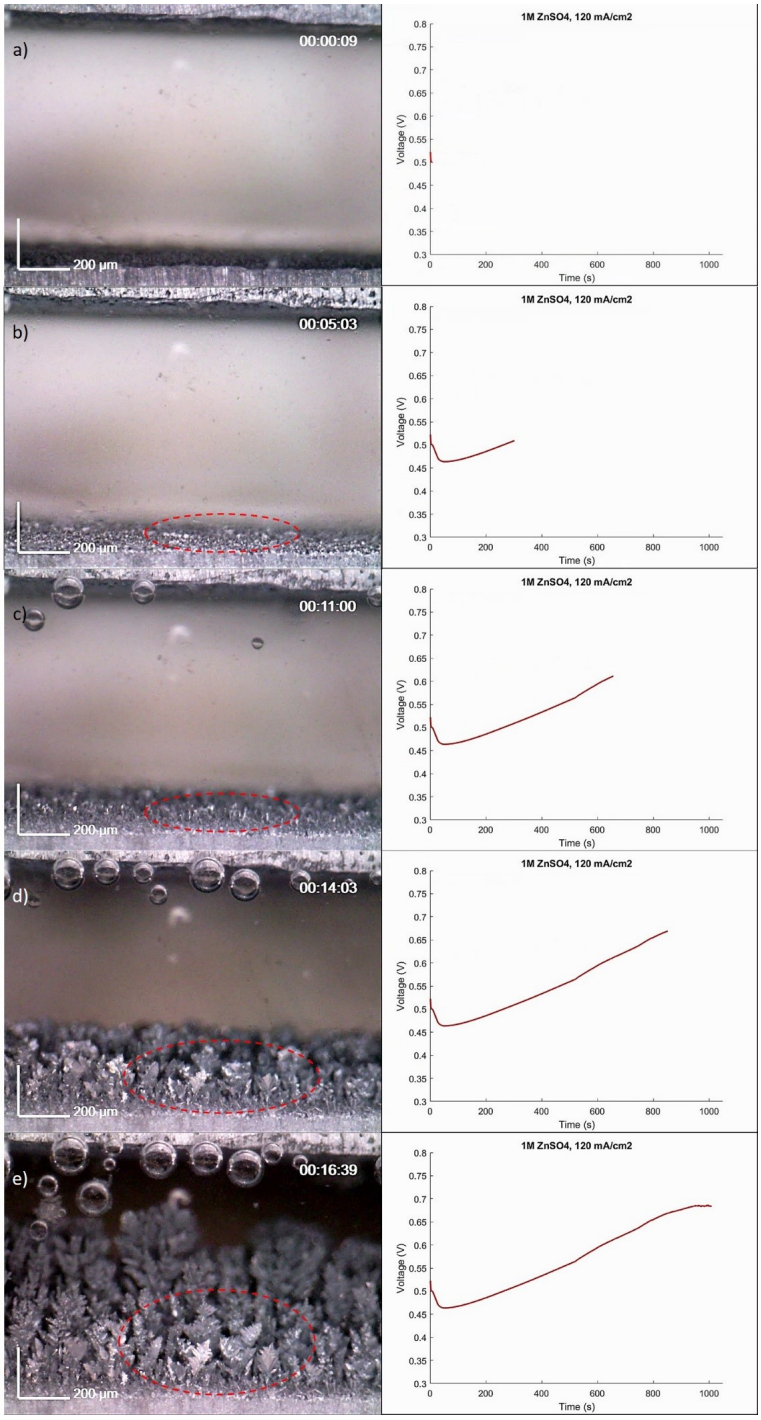


Figure 4.2: Video frames for the Zn-Zn Optical cell cycled at 120 mA/cm$^2$ for 18 minutes, and the corresponding voltage traces. The stagewise growth of dendrites from prismatic outgrowths, to dendrites growing vertically and finally to dendrites growing with branching can be observed.

The voltage trace of the Zn-Zn optical cell for 3 half cycles for 40 min, 50 min and 40 min respectively at 35 mA/cm$^2$ is analyzed, with a special focus on those points where the voltage trace exhibits path changes (corresponding to the impedance path changes as described by the reference framework[7]).

For the first half cycle (deposition on the bottom electrode) (Fig. 4.1b), an overvoltage maximum is observed right at the beginning, which then continuously drops as the deposition proceeds. The initial high polarization is due to the activation energy barrier associated with initial nucleation on Zinc.

Thereafter, zinc deposition proceeds mainly along a lower impedance pathway, i.e. deposition on already nucleated areas is preferred over fresh nucleation. As the nucleated areas grow, their surface area increases and this causes a decrease in the local (real) current density and therefore the overpotential. This value almost reaches a steady value, and the predominant mode of deposition is the growth of nucleated sites. The deposition is compact in nature.

At the beginning of the second half cycle, the overpotential reaches a maximum, followed by a steep drop. The maximum corresponds to the kinetic barrier for fresh deposition on the top electrode (not in view). The primary mode of stripping is from the fresh deposits of the previous half cycle. As their surface area decreases, the impedance for stripping increases, and this corresponds to a gradual increase in the polarization (Fig. 4.1c).

Once all the Zinc is stripped from the new deposits, blackening of the surface is observed (Fig. 4.1d). At this point, the polarization reaches a maximum value. The dominant stripping mechanism changes to stripping from the bulk. Like deposition, stripping is again non-homogeneous, and 'pits' are formed during the initial stripping from the bulk. The stripping mechanism gradually changes to pitting (although not clearly visible in the video, pitting was confirmed through post mortem SEM), and a change in impedance path is reflected by the voltage trace.

Pitting results in surface inhomogeneities on the bottom electrode. For the third half cycle, mossy Zinc deposition is observed on the bottom electrode, most likely originating from the rough, pitted sites of the previous half cycle (Fig. 4.1e). The voltage trace nearly repeats the same pattern as for the second half cycle (i.e. drop from an initial maximum, gradually increase up to a second maximum and then again decrease), and this behaviour of the voltage trace is repetitive in nature, in both the optical cell and other cell architectures. The reason for mossy growth during subsequent deposition cycles is further explained in Section 4.6.

In addition to the Zinc plating/stripping, bubble formation is observed close to the electrode during the stripping half cycle. The origin of this phenomenon, its dependence on the applied potential and its potential impact on the overall Coulombic efficiency have been discussed in detail in Appendix A.1

## 4.2. DENDRITE FORMATION: STAGES AND DEPENDENCE ON APPLIED POTENTIAL

While the general trend for the voltage trace in the first half cycle is as explained earlier for low and moderate current densities, deposition at very high current densities and/or

for longer periods can result in a slightly different voltage trace, due to the mass transfer limitation condition occurring at the cathode and the subsequent ramified growth. Such a trend was observed for Zinc deposition in the Zn-Zn symmetric system at 120 mA/cm$^2$. It was also possible to visualize the various stages involved in dendrite growth with the help of the operando video microscopy. When Zinc is deposited at a current density of 120 mA/cm$^2$, the Sand's time (see appendix A.3for calculations) corresponds to about 4 minutes.

The first prismatic outgrowths are indeed observed early on (around 4-5 minutes, Fig. 4.2b), but the dendritic outgrowth (i.e. accelerated deposit growth with branching) is observed starting from around 10-11 minutes (Fig. 4.2c). As one can observe, the deposit growth is initially lateral in nature (prismatic outgrowth), but branched dendrite growth commences once the radius of the tip is small enough to sustain spherical diffusion (around 10-11 minutes, Fig. 4.2c).

It is observed that the region after the first minimum in the voltage trace corresponds to the appearance of the first dendrite/prismatic deposit, and the voltage trace continues to increase throughout the dendrite initiation phase, where the dendrite initiation happens under diffusion control (Fig 4.2b,c). The continuous increase in the cell overpotential in the meantime can be attributed to the $Zn^{2+}$ concentration at the surface dropping drastically and to nearly zero.

However, once these dendrites grow beyond the influence of the diffusion layer, they grow rapidly with time in terms of height, and start branching out. This phase of the dendrite growth occurs under activation/kinetic control according to Bockris et al. [25]. During this period, the increase in the overpotential slows down (Fig. 4.2d), the value of the overpotential reaches a maximum and then starts to decrease (Fig. 4.2e). This is because the dendritic deposits are growing in the direction of the counter electrode, thereby reducing the effective interelectrode distance to be travelled by the Zinc ions.

The overall porosity of the Zinc deposits is observed to increase with time from 51.4% at 10 minutes to 68% at 14.5 minutes and 82.7% at 17 minutes (One may refer to Appendix A.4 for all the porosity values quoted hereafter). This further illustrates the transition from prismatic outgrowth to exponential and branched dendritic growth

As discussed in section 2.4, Zinc is known to exhibit several types of morphologies other than dendrites, and it would be of interest to investigate these morphologies produced at different current densities for the $ZnSO_4$ electrolyte system.

## 4.3. MORPHOLOGY CLASSIFICATION AND EFFECT OF EXPERIMENTAL PARAMETERS

Previous studies such as the one by Zhang et al. [16] for Alkaline electrolyte systems (with Zinc in the solution existing as Zincate ($Zn(OH)_4^{2-}$ ions)have been able to characterize and classify Zinc deposition at various current densities and by varying other experimental parameters. In contrast, this study employs the mildly acidic $ZnSO_4$ electrolyte (with Zinc existing as $Zn^{2+}$ ions in the solution) relevant for Zinc ion batteries.

There are several reasons to justify a separate study of morphology evolution at battery scale for the mildly acidic $ZnSO_4$ electrolyte system. To start with, the overall deposition kinetics of both the cases are quite different, with different ionic structures in the

solution and different activation energies. As explained by Zhang et al. [16] the different morphologies of Zinc are formed due to the interplay between mass transfer and activation controlled mechanisms of ion transport. With different kinetics, this interplay is expected to be different for mildly acidic electrolytes.

Further, several parasitic and corrosion reactions become thermodynamically favourable at alkaline pH, such as Hydrogen generation [1] and ZnO formation on the surface, resulting in loss of effective area of deposition. These factors also contribute to the evenness of Zinc deposition, and the degree of surface roughness in general hugely influences the deposition morphology. As such undesired effects are known to be a lot less pronounced in mildly acidic electrolytes, it would be of interest to investigate the different morphologies and the current densities at which they are generated in the case of $ZnSO_4$ based systems.

The aforementioned study [16] classified Zinc deposits as mossy, layerlike, boulder, dendrite and heavy spongy (cluster). Layerlike and bouldery deposits are commonly together referred to as 'compact' deposits, and differentiating between the two with optical microscopy can be difficult. In this study, almost all of the aforementioned morphologies are obtained for the current range investigated (1 to 120 mA/cm$^2$), with more than one morphology present on several occasions. Furthermore, it is also observed that the compact deposits are often temporary in nature and give way to either mossy or dendritic deposits depending on the current density.

### 4.3.1. IMPACT OF CURRENT DENSITY

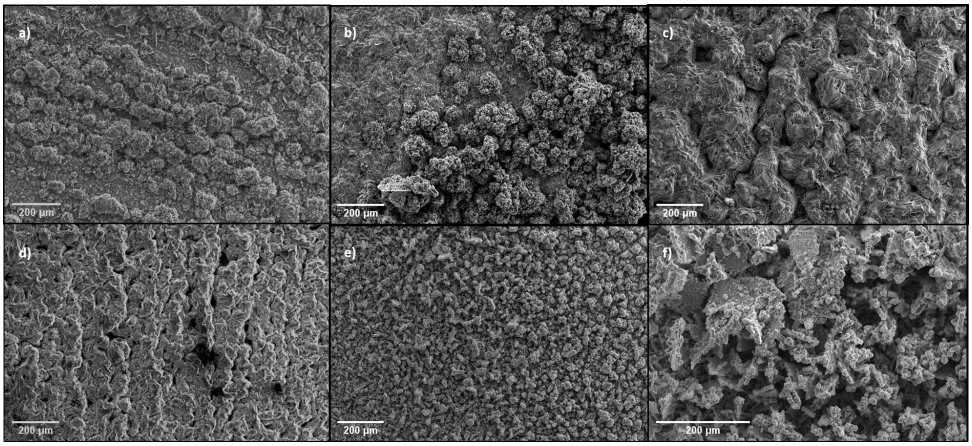


Figure 4.3: SEM Images of the Zinc deposits obtained after cycling for 35 mAh/cm$^2$ at different current densities: a) 1 mA/cm$^2$, b) 15 mA/cm$^2$, c) 35 mA/cm$^2$, d) 70 mA/cm$^2$, e) 120 mA/cm$^2$ (centre) and f) 120 mA/cm$^2$ (sides)

Further, the morphology of the Zinc deposits formed at a range of current densities (from 1 mA/cm$^2$ to 120 mA/cm$^2$) for 35 mAh/cm$^2$ of Zinc deposition was studied with the help of operando microscopy and post mortem SEM. At a lower current range of 1 mA/cm$^2$, the deposition is predominantly mossy in nature, although traces of layered

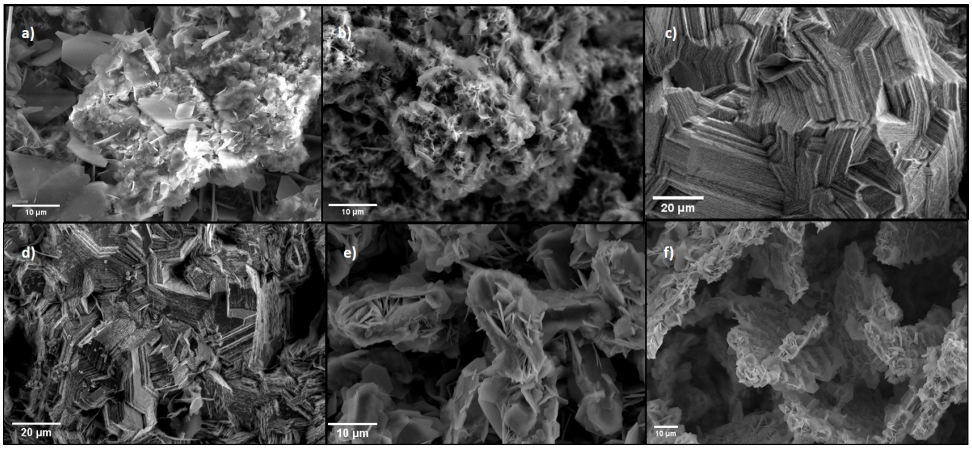


Figure 4.4: Magnified view of the SEM Images of the Zinc deposits obtained after cycling for 35 mAh/cm$^2$ at different current densities: a) 1 mA/cm$^2$, b) 15 mA/cm$^2$, c) 35 mA/cm$^2$, d) 70 mA/cm$^2$, e) 120 mA/cm$^2$ (centre) and f) 120 mA/cm$^2$ (sides)

lateral growth could also be observed (Fig.4.4a).

At a moderate current density of 15 mA/cm$^2$, a mixed morphology is observed, with the deposition being predominantly compact (boulder type) in nature, although mossy deposits appear to grow on top of the compact deposits after a certain period (an hour or so) as confirmed by the optical microscopy.

For higher current densities, i.e. 35 and 70 mA/cm$^2$, the deposition is again compact in nature, although it could be said that the deposition at 35 mA/cm$^2$ is more boulder-like in nature and the one at 70 mA/cm$^2$ appears to be more even. At the microstructural level, the morphology at both these current densities looks to be similar. The overall porosity of the deposits is also calculated based on the video and after 35 mAh/cm$^2$ of deposition, the 35 mA/cm$^2$ deposits exhibit a porosity of about 10% while the 70 mA/cm$^2$ deposits show about 5% porosity.

Further, at a very high current density of 120 mA/cm$^2$, a very uneven deposition is obtained, which consists of mainly clusterlike deposits , with dendritic deposits by the edges. The porosity of these deposits after 35 mAh/cm$^2$ of deposition is found to be about 48.7%. While the 'cluster' deposits visually look more compact than the mossy deposits, the high overall porosity is due to their uneven distribution and lack of aggregation with time as in the case of compact deposits.

Coming to the size of the individual deposits, the layerlike deposits are generally found to be in the range of 5-10 microns, the mossy growths in the range of tens of microns with filaments of the thickness of hundreds of nanometres. The cluster deposits are also in the range of tens of microns. The dendrites have a thickness averaging around 40 microns, the diameter of the dendrite tip is around 5-10 microns (see Appendix A.6.

### 4.3.2. IMPACT OF CURRENT DENSITY ON CRYSTAL ORIENTATION: XRD STUDY

Further, the ex-situ XRD analysis for the Zinc deposits obtained at different current densities result in some interesting observations with respect to the crystal orientation of Zinc deposits and also possible additional phases.

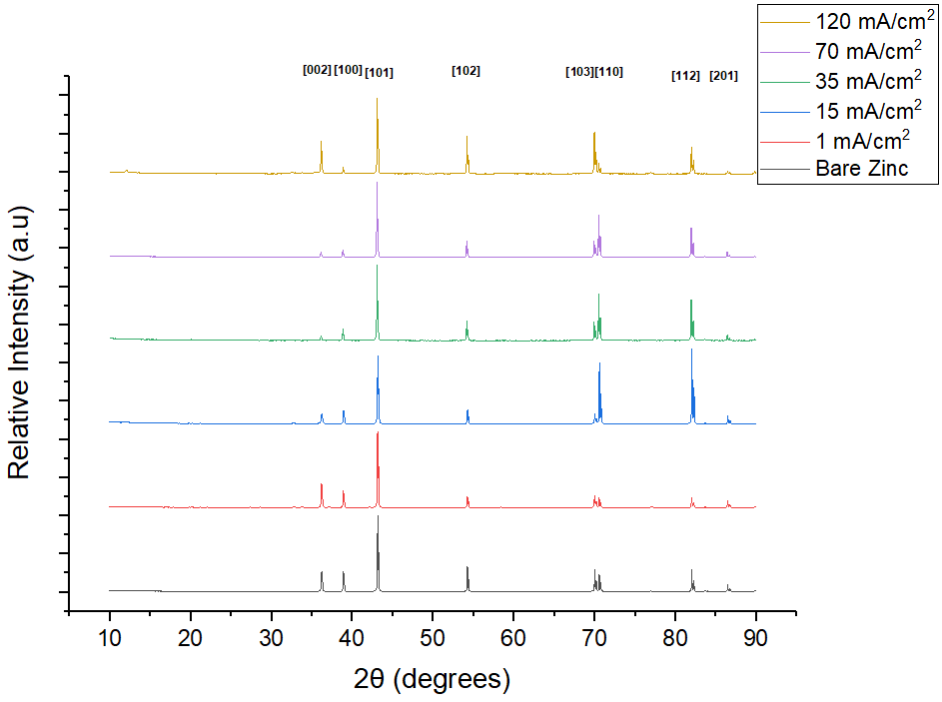


Figure 4.5: XRD Spectra of Zinc deposits after 35 mAh/cm$^2$ of cycling at different current densities. The polycrystalline nature of the deposits at 15 and 35 mA/cm$^2$ is evident as compared to the others

The XRD analysis of bare Zinc shows the Zn crystals being oriented primarily in the [101] direction. With increasing current density, the crystal orientation of the Zn deposits goes from being highly directional (in the [101] direction) to nearly non-directional, and then back to being directional at very high current densities. Zhang et al. [6] described the various types of morphologies along with their crystal orientations, and the results obtained in this study are in good accordance with the same.

For mossy and layered morphologies at 1 mA/cm$^2$, the relative intensity of the peak at [101] direction is much higher than that of the others. This is not the case at 15 mA/cm$^2$ and 35 mA/cm$^2$, (compact deposits), as [110] and [112] directions have comparable relative intensities. At 70 mA/cm$^2$, the relative intensity of [101] direction is found to increase slightly.

At 120 mA/cm$^2$, [101] direction has the highest relative intensity, whereas the peaks at several other directions, i.e. [002], [102],[103] and [112] have comparable relative intensities. This can be explained by the fact that a mix of cluster and dendritic morphology is obtained, with dendritic morphology being highly directional ( in the [101] direction)

and the cluster morphology being non directional.

The XRD study also reveals something interesting regarding the nature of Zinc deposition. Metallic zinc is not the only type of deposition observed. An additional Zinc Sulfate Hydoxy Hydrate (ZHS) is also observed at certain current densities (See Appendix A.5). ZHS has previously been observed as a phase on cathodes in the case of Zn-ion batteries with $ZnSO_4$ as the electrolyte salt. However, it has been argued that this phase is a self reaction of the electrolyte and has nothing much to do with the cathode [50] and these results corroborate the same.

### 4.3.3. TIME BASED MORPHOLOGY EVOLUTION

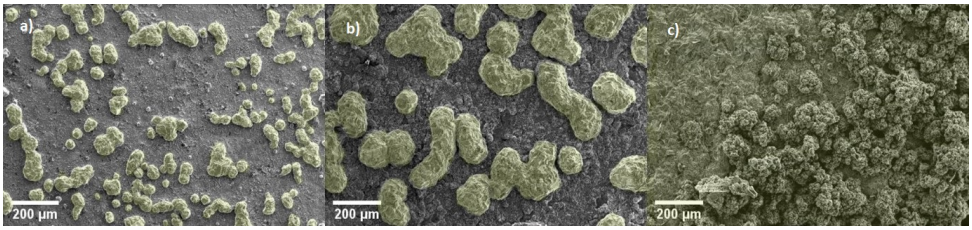


Figure 4.6: SEM images of time based deposition of Zinc at 15 mA/cm$^2$: a) 15 minutes,b) 1 hour and c) 2 hours

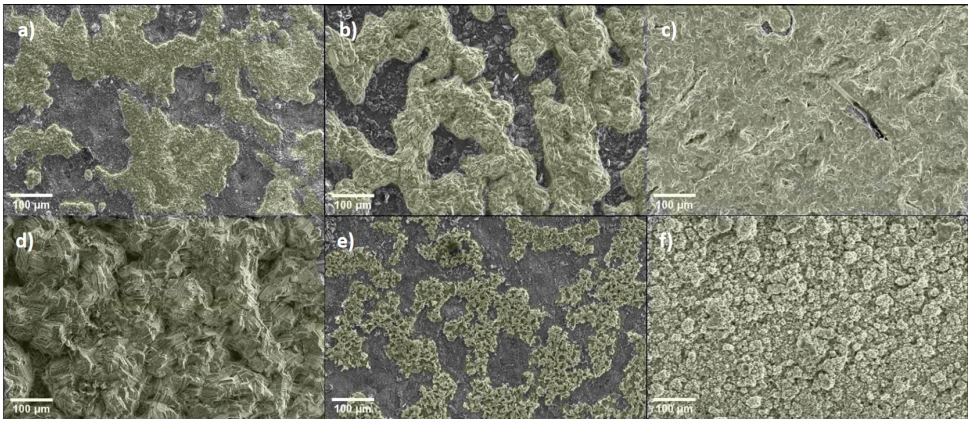


Figure 4.7: SEM images of time based deposition of Zinc at 35 mA/cm$^2$: a) 5 minutes,b) 15 minutes, c) 30 minutes, d) 1 hour e) 15 minute deposition and 15 minute stripping (1 cycle) and f) 1.5 cycles

As noted earlier, the time based evolution of deposition morphology in the compact regime can be hard to visualize with the Operando video microscopy. Therefore, Zinc samples subjected to fixed periods of deposition are later analyzed using SEM. The time based morphology evolution was studied for 15 and 35 mA/cm$^2$. For 35 mA/cm$^2$, the study was also extended to the second, third and fourth half cycles after the initial deposition half cycle.

For the deposition phase, it is observed that the islanded/patchy deposits generated during the initial phase of deposition grow in size and area, and then combine to form a

layer that covers the entire metal surface (Fig. 4.7a-d). Thereafter, zinc deposits further on top of this layer, giving boulderlike deposits.

While the deposition mechanism in both the cases appears to be multi-nuclear and multi-layered, it is interesting to note the visual differences between the nucleation and growth mechanisms at 15 and 35 mA/cm$^2$. In the former case, Zinc nucleates as hemispherical deposits, which then appear to grow in size to eventually impinge and form a deposition layer, whereas in the latter, the patches of zinc deposits (with a higher area coverage as compared to hemispheres) are observed early on, and these layers grow into compact deposits similar to those at 15 mA/cm$^2$, and then impinge to form the first deposition layer, on top of which the subsequent nucleation continues.

There also seems to be a difference in the nucleation mechanism on top of the first layer. In the former case, the deposition is mossy in nature (Fig. 4.6c) whereas in the latter, it is still compact and boulderlike.

For both these differences in the observed deposition morphology, the balance between mass transfer controlled and kinetic controlled mechanisms seems to be the key factor. Mass transfer limitations do not arise as quickly at lower current densities, and with the kinetics having a relatively higher degree of control over the deposition process in comparison, site specific, mossy deposits are likely to form.

However, it has to be noted that mossy growth on top of compact deposition can also take place at 35 mA/cm$^2$, depending on the roughness of the compact surface (which can increase over time). (See sections 4.3.4 and 4.3.5)

Further, the deposition and stripping appear to occur at two or more kinetic rates simultaneously. On analysing the foils under the SEM, it is observed that the Zinc deposition does indeed happen even in those regions surrounding the dominant patchy growth. However, the kinetics of deposition in these surrounding regions appears to be much slower. The same also holds true for stripping after deposition. In Fig. 4.7e, it can be observed that traces of the patches from the previous deposition are still visible even after stripping the same amount of zinc as what was deposited. However, there is indeed a least resistance path (in this case, the fresh deposits as compared to the bulk) from which majority of the stripping happens at a given point in time, as indicated by the voltage traces (Fig. 4.1)

### 4.3.4. MORPHOLOGY EVOLUTION WITH CONTINUOUS CYCLING

Figure 4.7 reveals that the degree of nonhomogenity at the end of the first cycle is considerably higher than that of pristine Zinc. As a result, the number of nucleation sites is much higher for the second deposition cycle, as observed in Figure 4.7e, and therefore the size of the nucleates is now much smaller as compared to the first deposition.

With the degree of roughness of metal electrode increasing with subsequent cycling, it was of interest to know whether moderate current densities could also lead to dendrite formation. Similar to the observations made by Zhang et al for Zinc deposition in Alkaline electrolyte systems [16], with repeated cycling at moderate current densities (half cycles of 15 min) in the mildly acidic/nearly neutral $ZnSO_4$ electrolyte system, the compact deposition is likely replaced by either mossy growth or dendritic growth, depending on the current density.

In the case of 15 mA/cm$^2$, mossy deposits are obtained by the end of the 3rd de-

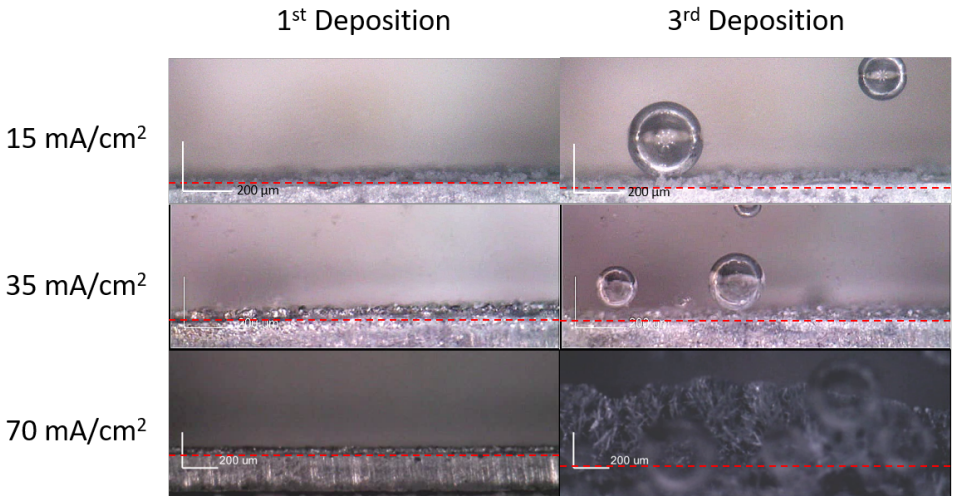


Figure 4.8: Evolution of zinc deposits with multiple cycles at different current densities (1 half cycle = 15 minutes)

position cycle (Fig 4.8 top), whereas in the case of 70 mA/cm$^2$, dendrites are obtained around the same period. With 35 mA/cm$^2$, while the deposition after 3 deposition cycles appears to be compact, a closer look would reveal that the porosity of the deposits has actually increased by 15% (see Appendix A.4), suggesting that this could pave way to a more mossy deposition the next few cycles. The exact current density at which a transition to dendrites from mossy growth occurs on long deposition is not clearly known.

### 4.3.5. MORPHOLOGY EVOLUTION WITH UNEVEN DEPOSITION (TIME)

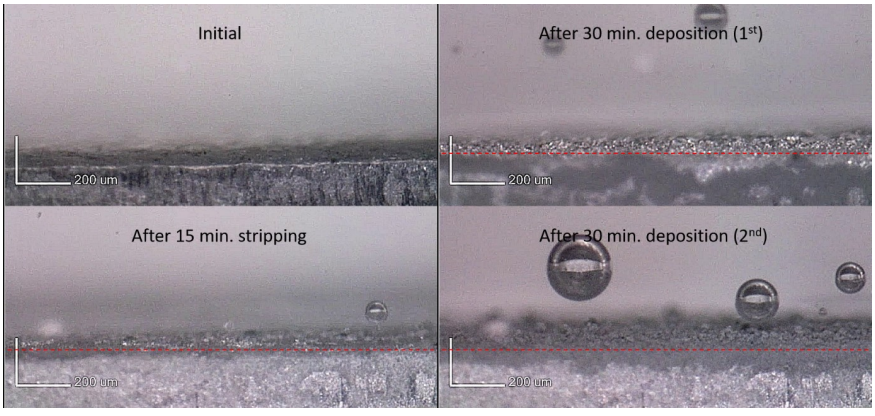


Figure 4.9: Evolution of Zinc deposits with uneven deposition-stripping times at 35 mA/cm$^2$

To simulate the uneven charge and discharge times in the case of real life batteries

and its potential impact on the metal anode, Zinc was deposited at 35 mA/cm$^2$ for 30 min, stripped for 15 min and again deposited for 30 minutes. The results are as shown in Fig. 4.9. While the deposition after the first 30 minutes is compact, the second 30 minute deposition is mossy in nature (with a porosity of about 44.7%). It is observed that the uneven deposition/stripping times cause a greater degree of roughness on the metal surface and this gives rise to non-compact Zinc deposition, and at higher current densities, this would eventually lead to dendrite formation. A possible explanation for the observed mossy growth is provided in Section 4.6.

### 4.3.6. MORPHOLOGY EVOLUTION WITH UNEVEN DEPOSITION (CURRENT DENSITY)

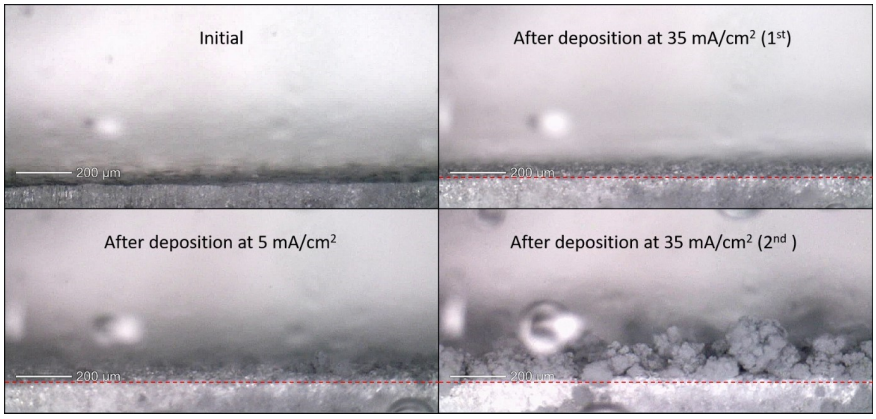


Figure 4.10: Evolution of Zinc deposits with uneven current density for 30 minutes each

In order to investigate the effects of varying current densities on the Zinc deposition pattern, one of the Zinc electrodes in the Zn-Zn symmetric cell was subjected to successive depositions at differing current densities: 35 mA/cm$^2$ for 30 mins, 5 mA/cm$^2$ for 30 mins and again 35 mA/cm$^2$ for 30 mins. The deposition for the first 30 minutes is found to be compact, and the deposition that followed at 5 mA/cm$^2$ results in mossy growth on top of the compact deposition. On further depositing Zinc at 35 mA/cm$^2$, the deposition continues to be mossy in nature, depositing on top of the previous mossy deposition at 5 mA/cm$^2$. The porosity of the deposits at the end of this deposition is about 46.7%.

It could be concluded that switching between different deposition current densities gives rise to non-compact morphologies (mossy at low to moderate current densities and dendrite at high current densities).

### 4.3.7. EFFECT OF SALT CONCENTRATION

In addition to the base condition of 1M $ZnSO_4$ at 35mA/cm$^2$ for 1 hour, Zinc deposition for 35 mAh/cm$^2$, but with certain variations to the process conditions were studied. These included change in salt concentration, presence of additional metal sulfates, high temperature and a different degree of roughness of the substrate.

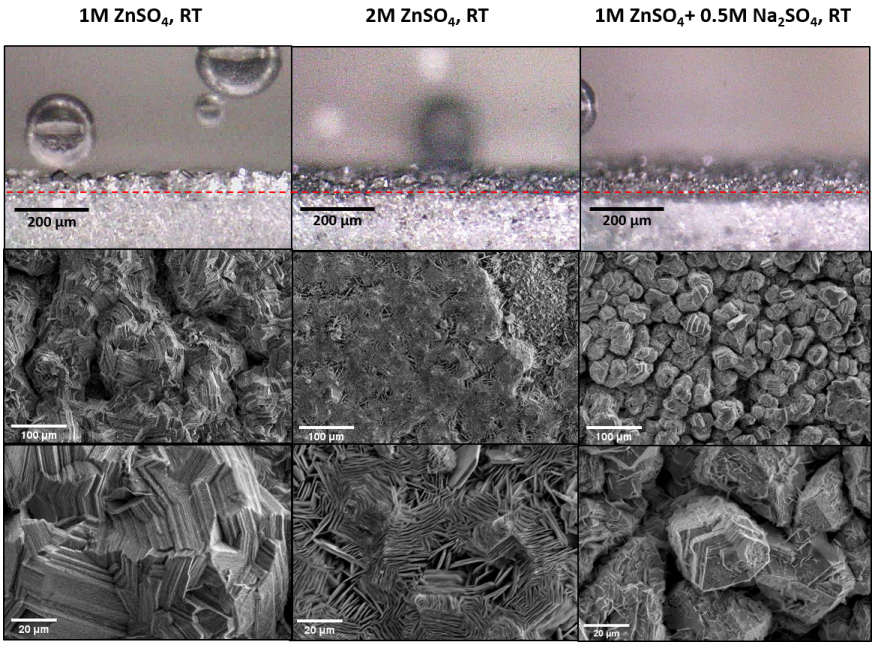


Figure 4.11: Operando microscopy (Top) and SEM Images (centre, bottom) of Zinc deposits cycled for 35 mAh/cm$^2$ with different salt concentrations

A higher salt concentration is generally favoured for batteries with high discharge requirements, as this can help avoid the depletion of metal cations at high currents, resulting in space charge effects and eventually dendrite formation. However, increasing the salt concentration close to saturation levels can cause issues with respect to the long term performance of the system, mainly to do with precipitation and passivation of the metal surface.

Figure 4.11 shows the morphologies of the Zinc post 1 hour of deposition at 35 mA/cm$^2$ for both 1M and 2M. While a few differences in the deposition pattern are observed from the optical microscopy, a post-mortem SEM provides a much clearer picture of the difference in the morphologies. In comparison to the 1M $ZnSO_4$ deposit, the 2M $ZnSO_4$ appears to be more even, and a closer look at the deposit reveals the layered nature of the deposit obtained as opposed to being boulderlike. The overall porosity of the deposits is around 6.5%, not too different from the 10% in the case of 1M $ZnSO_4$ electrolyte.

### 4.3.8. EFFECT OF ADDITIONAL METAL SULFATES

As discussed in section 2.1.2, additional salts, particularly sulfates of cathode related materials such as $MnSO_4$ and $Na_2SO_4$ have been used as electrolytes to improve the lifetimes of both the metal anode and the cathode. To investigate the influence of such additional salts on the Zinc deposition morphology, a mixture of 1M $ZnSO_4$ and 0.5M $Na_2SO_4$ was used as the electrolyte.

After 35 mAh/cm$^2$ of deposition, it is observed that the deposits are still boulderlike

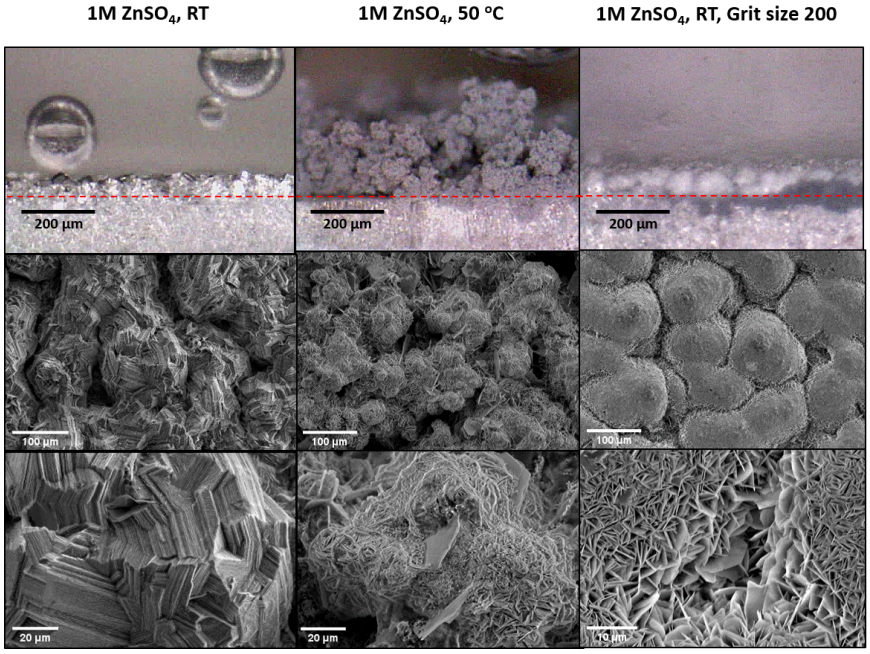


Figure 4.12: SEM Images SEM Images of Zinc deposits cycled for 35 mAh/cm$^2$: 1M $ZnSO_4$ and room temp. (left), 1M $ZnSO_4$ and 50 $^o$C (middle), 1M $ZnSO_4$ and room temp. with higher electrode roughness (right)

in nature, but the size of the deposits appears to be much smaller and more uniform in general. The overall porosity of these deposits is around 23.6% which could be the result of smaller individual deposits due to the electrostatic shield effect of $Na^+$ ions [20], and thereby slightly higher gap in between the deposits.

### 4.3.9. EFFECT OF TEMPERATURE

High temperature Zinc deposition was studied by subjecting the Zn-Zn symmetric cell with 1M $ZnSO_4$ electrolyte to 35 mAh/cm$^2$ of deposition at 50 $^o$C.

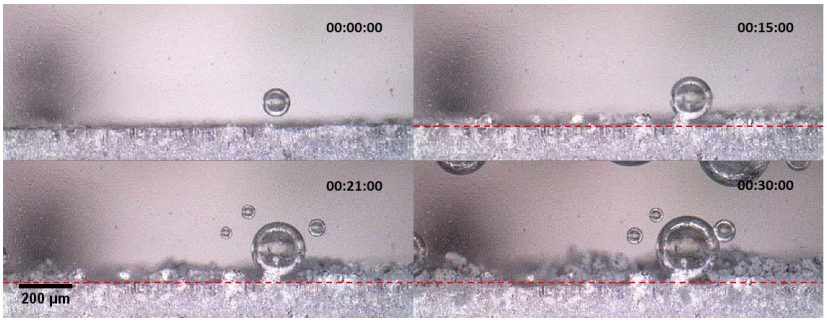


Figure 4.13: Transition of zinc deposit morphology from compact to mossy at 50 $^o$C

The sample has a porous and mossy deposition, clearly visible from both the optical microscopy and the post-mortem SEM. On a more careful analysis of the time evolution of these deposits, it is observed (as in Fig. 4.13) that the deposition does indeed start as a compact deposition, but the uniformity of deposition over the surface is poor, likely generating a lot of grooves. It can be observed that mossy deposition begins on top of the compact deposits after around 20 minutes and then proceeds to cover nearly the entire surface. The overall porosity of these deposits is found to be rather high at around 84%.

### 4.3.10. EFFECT OF SURFACE ROUGHNESS

While the surface roughness of zinc generated over time has been observed to generate non-compact deposits so far, it was of interest to investigate how a different initial degree of roughness would alter the morphology of the first deposition. For the Zn polished with a 200 rating grit instead of a 2000 rating grit, a very distinct initial morphology is observed, i.e. the deposits appear to be hemispherical nucleations just like in the base case, but these individual deposits are further made up of lateral layered deposits at an even smaller scale. With a value of 23.3%, the overall porosity also seems to be higher than that in the case of 2000 grit size.

## 4.4. INITIAL DEPOSITION - TEM STUDY

For the in-situ TEM study performed to study the initial electrodeposition mechanism of Zinc (Potential scan between 1 and -0.2V at a scan rate of 100 mV/s for 2 cycles), the morphological changes observed are displayed in Fig. 4.14. It is to be noted here that the potential applied here is with respect to the reference Pt electrode. The working electrode is shown on the right, while the counter electrode is not in the field of view.

The first electrodeposition is observed at -0.16 V and continues upto -0.2V (the lower limit) (Fig. 4.14). The deposition stays on top of the working electrode till +0.16 V where it gets stripped . The nature of the Zinc deposit observed could be described as flaky/layered. Zinc deposition is again observed at the same voltage range during the second cycle. However, all the Zinc deposited is not stripped off at 0.16 V in this case.

The observations further corroborate the fact that a minimum overpotential, corresponding to the activation energy of Zinc deposition, is necessary for the initiation of Zinc deposits, and the initial deposition always happens under activation control. But, it has to be noted that the Zinc deposition in this case was on Pt, and the value of nucleation overpotential for deposition on metallic Zinc is going to be different.

## 4.5. EFFECT OF AN SPEEK POLYMER COATING ON ZINC

Having established the fact that continuous cycling of zinc eventually gives way to non-compact morphologies both at low and high current densities, it would be ideal to have a protective layer that is hydrophilic, conducts $Zn^{2+}$ ions, adheres well to the Zn anode and is able to mechanically protect the metal anode from dendrite formation. While several commercial binders such as PVDF (that have also been successfully deployed as protective coatings on Lithium) are hydrophobic in nature, hydrophilic polymers such as SPEEK could be of interest.

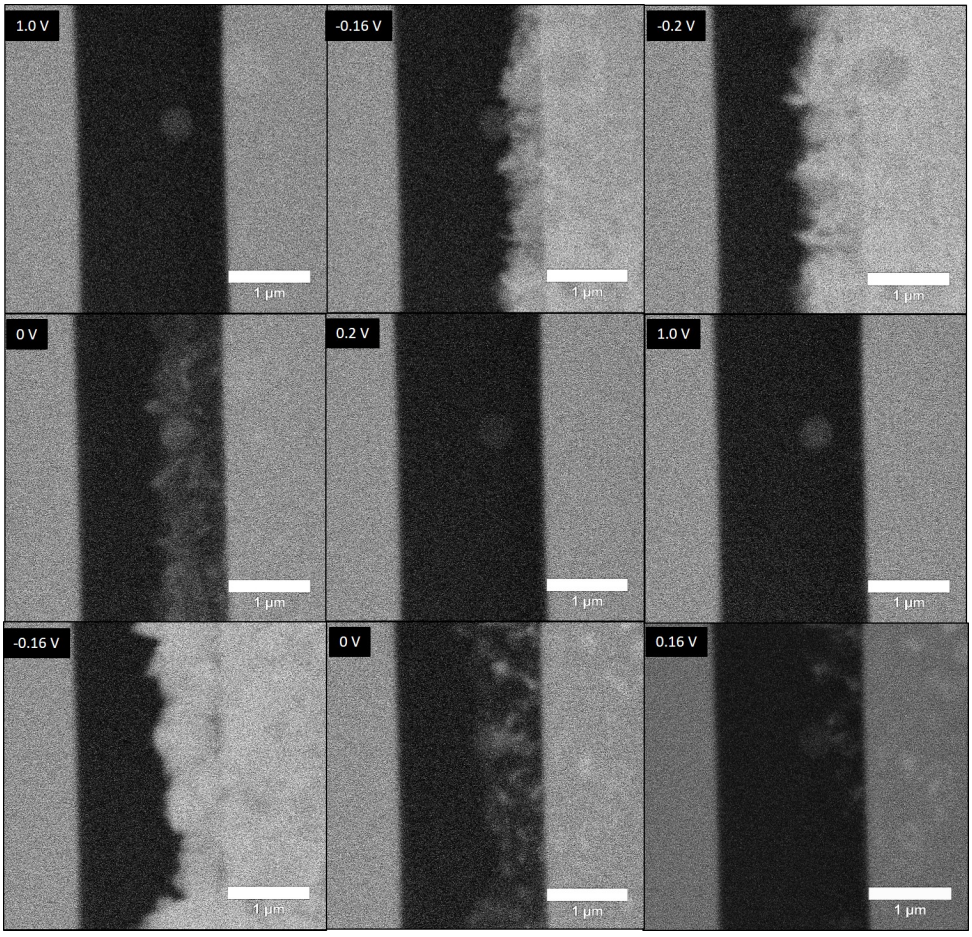


Figure 4.14: In-situ TEM images for initial electrodeposition of Zinc in $ZnSO_4$ electrolyte: a) Initial deposition at -0.16 V b) Electrodeposited Zinc at 0 V c) Bare Pt surface stripped of Zinc at 0.16 V

### 4.5.1. OPERANDO MICROSCOPY

A Zn Zn symmetric cell with one of the sides coated with SPEEK was subjected to cycling at 35 mA/cm$^2$ with half cycles of 15 mins each, and the results are as shown in Fig. 4.15. (bottom side coated with SPEEK).

During the deposition half cycle, while the zinc deposition does appear to happen through and underneath the coating, the surface does not look very uniform. Zinc deposits under hemispherical pockets of the layer that have seemingly delaminated from the metal. During the stripping half cycle, these pockets are stripped of Zinc, following which the stretched pockets of the polymer collapse, but the deformation appears to be plastic in nature. During the second deposition cycle, the number of these pockets and therefore the overall area coverage appears to increase.

Looking at the post mortem SEM of the coated Zinc foil, it can be observed that the

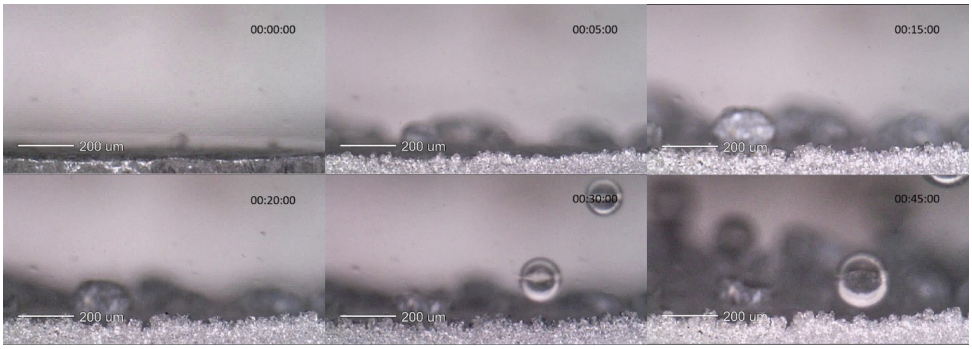


Figure 4.15: Deposition and stripping of Zinc through an SPEEK coated Zn electrode: First Deposition cycle (a, b and c), First stripping cycle (d and e), Second deposition cycle (f)

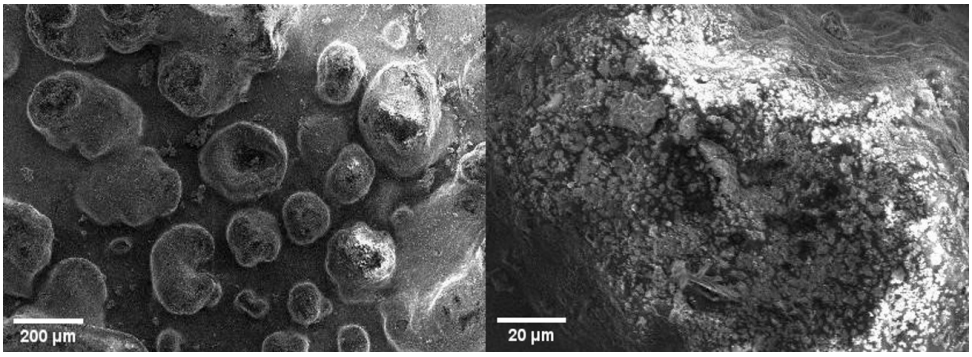


Figure 4.16: Post-mortem SEM Images of the SPEEK layer coated on Zinc

delamination of the SPEEK layer occurs at several places almost evenly throughout the foil (Fig. 4.16, left) , allowing for Zinc deposition underneath. There do not seem to be any signs of mechanical failure of the protective layer either. However, traces of microzinc particles can be observed on top of the delaminated regions and on top of the coated layer in general (Fig. 4.16, right). Therefore, it would be of interest to investigate the extent to which such deposition can occur with long term cycling.

### 4.5.2. GALVANOSTATIC CYCLING

To test the long term electrochemical stability and performance of the SPEEK coating on Zn in a $ZnSO_4$ electrolyte environment, an SPEEK coated Zn electrode - Cu current collector half cell was run at 2.5 mAh/cm$^2$ (5 mA/cm$^2$ for 30 minutes). A metal anode – Cu collector configuration was chosen ahead of symmetric cells for two reasons: 1) It allows a calculation of Coulombic efficiency at the end of each cycle and 2) A practical observation made was that in the case of cells with coated electrodes on both sides, the cell resistance is very high and creation of Zn conduction channels is very inefficient, giving rise to alternate pathways of Zinc deposition.

Further, it was decided to always start the cycling with stripping the metal from the

coated side (rather than deposition through the coating), as this creates a space underneath the coating where the metal can reversibly deposit, without much loss of adherence to the surface. A similar logic was also applied to testing Lithium based cells coated with Li-SPEEK, as seen in section 5.5.1.

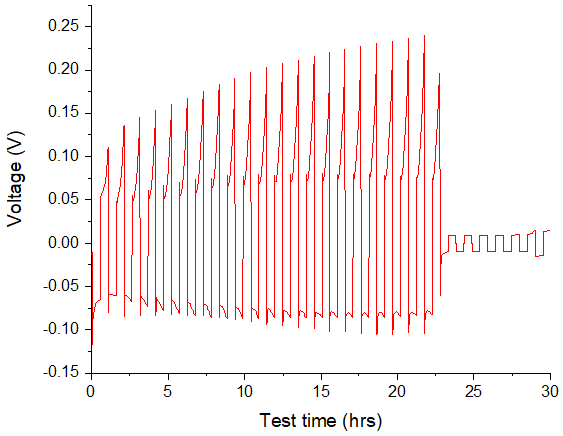


Figure 4.17: Galvanostatic voltage traces of the Zn-Cu cell with SPEEK coated on Zn

The galvanostatic voltage traces for the Coated Zn-Cu test cell are are obtained as shown in Fig. 4.17. The cell ran for about 23 cycles, thereby establishing a proof of concept for potential application of SPEEK as a protective layer in Zn anode based batteries. A recurring observation during the deposition half cycle (i.e. deposition on Zn, through the SPEEK layer) is, however, the sawtooth-like shape of the voltage trace that keeps increasing in magnitude, implying a continuous increase of impedance at the interface. An ohmic short is reached after about 23 cycles.

## 4.6. DISCUSSION

### 4.6.1. NATURE OF ZINC DEPOSITS AND THEIR DEPENDENCE ON EXPERIMENTAL PARAMETERS

It turns out that the nature of the Zinc deposits obtained at different current densities for a $ZnSO_4$ electrolyte system can, for single deposition cycles, be explained on the basis of the controlling deposition mechanism at different current densities as proposed by Zhang et al. for Zinc deposition in alkaline systems,[16] as there does not seem to be much of a difference when it comes to the types morphologies obtained with a single deposition cycle, although the current density ranges over which they are obtained are somewhat different. The present study also investigated the long term cycling performance of the Zinc anode and possible explanations for the observed morphological changes have been listed down.

Depending on the current density applied, the mode of Zinc deposition can be either

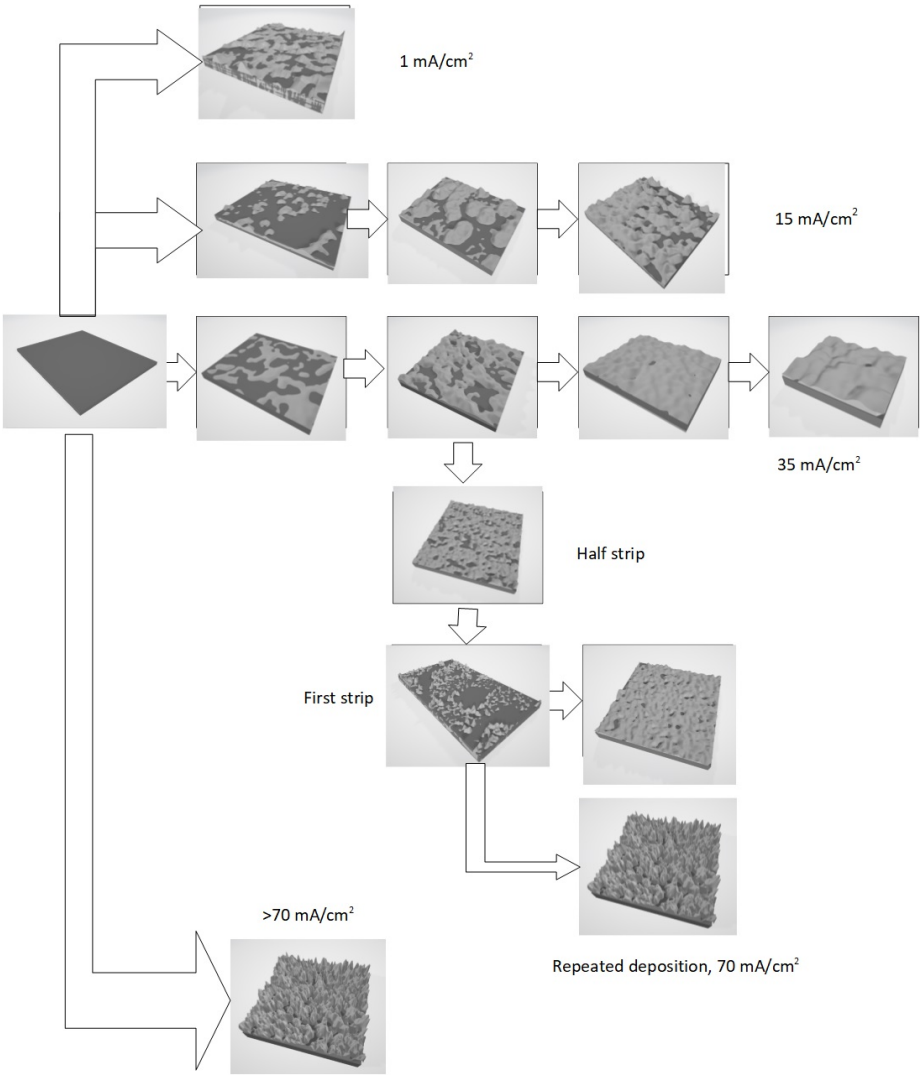


Figure 4.18: 3D Schematic Modelling of the Time Evolution of Zinc deposits at different current densities

diffusion (mass transfer) controlled, activation (kinetics) controlled, or a combination of the two, and the control mechanisms ultimately decide the nature of morphology obtained. The general trend observed is that, the deposition tends to be activation controlled in the beginning at low to moderate current densities, and the influence of mass transfer over the process increases with time. In comparison, the mass transfer limited condition is attained much earlier at higher current densities.

**Mossy Deposits:** At extremely low current densities, the nucleation overpotential becomes crucial. The deposit initiation occurs selectively on a few nucleation sites, and according to Zhang et. al., the overall process is under mixed charge transfer and nucleation control (both being the components of the overall activation process) [16], and this gives rise to mossy deposits. It is also worth noting that for the other metal anode of interest in this study, i.e. Lithium, Bai et al. note that mossy Lithium growth is in fact, typical of reaction (kinetics) controlled deposition. [17]

However, mossy deposits are also observed in $ZnSO_4$ electrolyte systems at low to moderate current densities (1-35 $mA/cm^2$), where charge transfer is not one of the limiting factors. They are observed to grow on top of previously deposited compact deposits, and their time occurrence varies depending on the degree of surface roughness generated during cycling.

It is observed that compact deposits quickly give way to mossy deposits when the deposition and stripping times were uneven, which generally increased the surface roughness. While the deposition at moderate current densities is generally under mixed activation and diffusion control, with increasing surface roughness, it is likely that Zinc chooses to selectively nucleate on the grooves and the nonhomogenties created by the previous deposition, with the diffusion resistance to reach these sites possibly being lesser, availability of such preferential sites for deposition appears to make the deposition more activation controlled, and therefore mossy deposits are observed.

Further, switching from higher to lower current densities also resulted in mossy deposits growing on top of the compact deposits. With a sudden drop in the current density, the rate of Zinc ion depletion at the surface and therefore the mass transfer dependence decreases, the overall deposition becomes more activation controlled, giving rise to mossy deposits.

Also, mossy deposits are observed to eventually replace compact deposits at high temperature. This could possibly be explained by the fact that the diffusivity of $Zn^{2+}$ increases with the temperature, which lowers the degree of mass transfer control and makes the overall process more activation controlled.

**Layered/Flaky Deposits:** At low current densities, purely under activation control (nucleation control, charge transfer no longer a limiting factor), the deposits initially grow in an oriented, layered/flaky manner to minimize the activation energy. Traces of such flaky deposits can be found in both $1mA/cm^2$ and 15 $mA/cm^2$ deposits. Further, flaky deposition was also observed in the TEM study for initial Zinc electrodeposition. Interestingly, the deposits formed at 35 $mA/cm^2$ for a 2M $ZnSO_4$ solution, although compact, are less boulderlike and more layered in terms of microstructure (Fig. 4.11). With a higher initial concentration of $Zn^{2+}$ in the solution as compared to the 1M $ZnSO_4$ sample, the overall process likely becomes more activation controlled and less diffusion controlled, which explains the more layered microstructure.

In addition, it appears that the grit size also plays a major role in determining the type of compact deposition. The Zinc subjected to grinding with a 200 rating grit provides several microstructural sites for the initial deposition of zinc. At moderate current densities, layered deposits tend to initiate on these sites instead of mossy deposits, but the deposition mode becomes mixed controlled as the degree of mass transfer control increases with time. This possibly explains the semi-circular shape of the overall deposit (Fig. 4.12.

**Boulderlike Deposits:** For moderate current densities of around 35 mA/cm$^2$, the concentration gradient in the electrolyte becomes very important and the deposition is usually under mixed (activation and diffusion) control. As far the growth direction is concerned, Zhang et al. [16] suggest that there is competition between the field of diffusion and the direction of the lateral layer growth. As a result, the deposits end up being boulderlike and not oriented in a particular crystal direction (polycrystalline). The initial roughness of the Zinc also appears to play a role here, as Zinc foils polished with higher grit ratings (2000) show boulderlike deposits and little to no flaky deposits. With the Zinc surface being even and very little sites for selective nucleation, boulderlike deposits are likely to form.

The size of the individual boulders is subject to influence by the additives present, in the case of $ZnSO_4$ with $Na_2SO_4$ as an additive, the $Na^+$ ions display the electrostatic shield mechanism [20] and thereby significantly reduce the size of the individual boulders.

**Dendritic Deposits:** Further, at very high current densities, the concentration gradient becomes even more significant, and under nearly pure diffusion control, the deposits begin to grow as dendrites in the direction of diffusion, which is predominantly perpendicular to the surface of the electrode, but also has a spherical diffusion component that causes the branching of the dendrites, mainly in the [112] direction.

This explanation is further corroborated by the XRD results, which clearly suggest dominant growth along the [101] direction for the 120 mA/cm$^2$ sample, but this dominance decreases from 120 to 70 and then 35 mA/cm$^2$, with the peaks for [101],[112],[103] all having similar intensities at 35 mA/cm$^2$, indicating the polycrystalline nature of the boulder deposits.

**Clusterlike Deposits:** In addition to the dendritic morphology at the edges, electrodeposition at 120 mA/cm$^2$ also resulted in what could be described as a clusterlike morphology. While not as compact as the boulders, these deposits appear to be a thick bunch of layered deposits. The initiation of these deposits seems to have been under activation control as flakes, but mass transfer limitations could have resulted in the vertical growth. It would be of interest to investigate this current range further to understand this morphology better.

Based on the observations made in this study, a schematic model indicating the morphology evolution at different current densities and with continuous cycling has been constructed (Fig. 4.18). While it is not precisely known how much time it would take for a full Zn-ion battery to fail under each of the operational conditions discussed, or to what extent each of the non-compact morphologies discussed is suppressed with the help of commercial separators, it would certainly be of interest to explore the impact of a Zinc-ion conductive polymer coating on the performance of the Zinc anode.

### 4.6.2. SPEEK AS A SURFACE COATING ON ZINC

Operando microscopy carried out for the SPEEK coated Zinc electrode helped visualize the characteristic movement of the polymer layer during cycling, and provided a visual proof of Zinc deposition underneath the layer. It is important to note, however, that the streching and delamination of the polymer appears to be plastic in nature, and at high thicknesses, one could expect the entire coating to nearly delaminate, after which this layer would effectively function as an additional separator.

A proof of concept was established for the use of SPEEK as a coating in a Zn-Cu test cell. It is interesting to note the slowly increasing value of the overpotential during the deposition half cycles. This clearly highlights a change in the characteristics of the interface, resulting in a gradual increase of impedance to Zinc transport. To fully understand any such changes happening it would be essential to first figure out the mechanism with Zinc conducts through the SPEEK coating.

While the mechanism of conduction for protons through ionomers in aqueous systems is well established, not much work has been carried out when it comes to conducting divalent cations through SPEEK. Therefore, it would be of interest to investigate the same, and this would also potentially provide insights into the origins of increasing impedance with cycling.

Another aspect to be carefully studied is the impact of having an SPEEK film on the pH of the system. Hydrated SPEEK turns out to be acidic (because of the dissociation of the sulfonic acid groups), which could make the water splitting reactions more favourable at its surface. This could alter the pH of the system during the operation, which could lead to cathode instability and also continuous electrolyte loss. It is therefore, important to study this phenomenon in more detail.

# 5

# Study of Electrochemical Performance of Lithium metal anodes

In the following chapter, the results of a series of experiments carried out to study the electrochemical performance of the Lithium metal anode have been described. The chapter begins with the study of bare Li anode, followed by a study of the effect of aspects such as the SEI and the type of separator used on Li deposition. The various types of morphologies obtained on the Li metal anode in carbonate based electrolytes at the battery scale have already been studied by Bai et al. [17] and several others. Therefore, morphology classification for Li is not a part of this study.

The focus then shifts to studying the effect of polymer based coatings on Li deposition. PVDF is used as a reference polymer coating and its protective actions are studied. Thereafter, similar experiments are carried out for the polymer of interest, Li-SPEEK. Further, certain modifications in terms of thickness and composition of the polymer are also attempted to study their impact on the overall performance.

## 5.1. Correlating Voltage Traces with Morphology

First, a Li-Li symmetric cell was run at 5 mA/cm$^2$ with half cycles lasting 15 minutes each. The morphology evolution was correlated to the voltage trace observed (see Fig. 5.1) in an approach similar to that by Dasgupta et al. [7] For the first half cycle, the overpotential starts from a maximum and then continues to decrease, while the deposition and stripping pathways change from fresh nucleation to growth of deposits and from bulk stripping to pitting respectively.

For the second half cycle, the initial stripping occurs from the fresh deposits, which turn darker as the active Lithium is removed. The impedance associated with this path increases as indicated by the voltage trace, until there is a change of stripping pathway

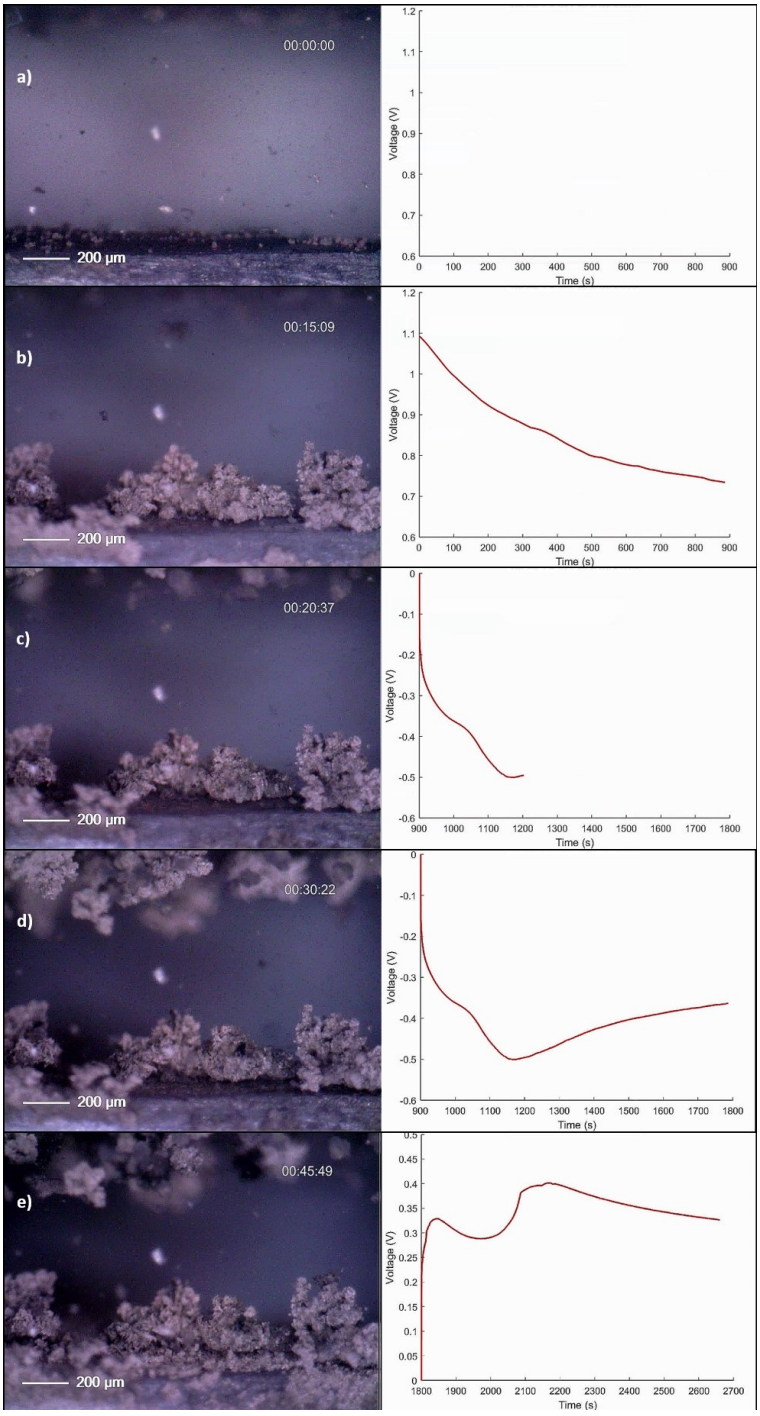


Figure 5.1: Morphology changes along with the corresponding voltage traces for the Li-Li symmetric cell under operando microscopy. Lithium deposits at random places and with uneven heights (b). Blackening of the Li deposits is observed as the active Li is removed (d, bottom electrode and e, top electrode). New deposits tend to push the 'dead' Li upwards (e).

to stripping from the bulk and then to pitting. It can be observed that the dead Li layers are pushed upwards as pitting commences.

For the third half cycle, a similar half cycle is repeated and it can be observed that the deposition now occurs on sites that were pitted in the previous half cycle. Deposition is also observed on those active sites where Lithium deposited during the first half cycle, with the dead Lithium layers being pushed further up. Therefore, the area coverage of Lithium surface for Lithium deposition increases with cycling. However. the growth over the total area is still very non uniform. This voltage trace is commonly observed in Li-Li symmetric cells and the same was confirmed for Lab cell experiments at 5 mA/cm$^2$. The overall porosity of these deposits is very high at about 96%.

## 5.2. EFFECT OF SEI AND ITS HOMOGENEITY ON MORPHOLOGY EVOLUTION

An important observation to be made is that the deposition occurs at random islanded locations in the beginning. The locations of the second deposition, although much more uniform, are not as uniform as in the case of metals like Zinc. Much of this can be attributed to the formation of the Solid electrolyte interface (SEI), inhomogenous in composition and therefore also in conductivity over the Li surface.

SEI can be induced on Li at several stages, and one of them could be the cleaning of the Li foil. If carbonates such as DEC and DMC are used to clean the Li surface prior to use, they can already react with the Li surface and form a heterogenous SEI layer. The soak time (rest period before running the cell) can also play a role, and while an increased soak time can be beneficial in presence of additives that form a stable interface (VC and FEC), an electrolyte without such additives will only cause a thicker non-homogenous SEI to grow. In comparison to other anode materials such as graphite or Silicon, the formation of the SEI on Li metal anode consumes more electrolyte.

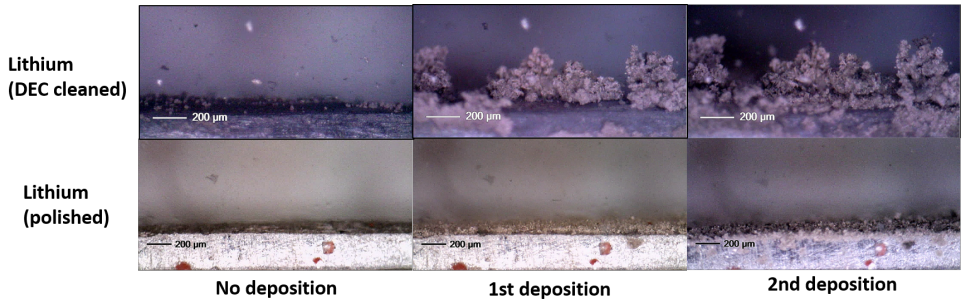


Figure 5.2: Morphology Evolution in Li-Li symmetric cells with DEC cleaned(top) and mechanically cleaned (bottom) surfaces. In the case of the latter, the absence of SEI for the first few minutes results in a very uniform Li deposition.

However, in the absence of such a non-homogeneous interface, although for a very short period, bare Lithium should also be able to exhibit a uniform deposition pattern. To test this hypothesis, the Li foils were mechanically cleaned until the surface was shiny. The Li surface was visibly a bit coarser, and these foils were assembled in a symmetric

cell and run immediately. A uniform, dense deposition of Lithium is observed for the first 2-3 half cycles, but the deposition slowly starts to get uneven with increased time of contact with the electrolyte (Fig. 5.2, bottom). In terms of compactness of deposition, the obtained deposits are 2.78 times denser than the base case.

While conventional Li metal batteries do inevitably come in contact with the liquid electrolyte to develop an SEI layer, this experiment shows how drastically the deposition morphology gets altered in its absence. This result illustrates the importance of ensuring either a uniform SEI layer or a uniform artificial passivation layer that completely eliminates any possibility of heterogeneous SEI formation to ensure uniform, compact Li deposition over a long term.

## 5.3. EFFECT OF SEPARATOR AND THE CASE FOR POLYMER BASED COATINGS ON LI

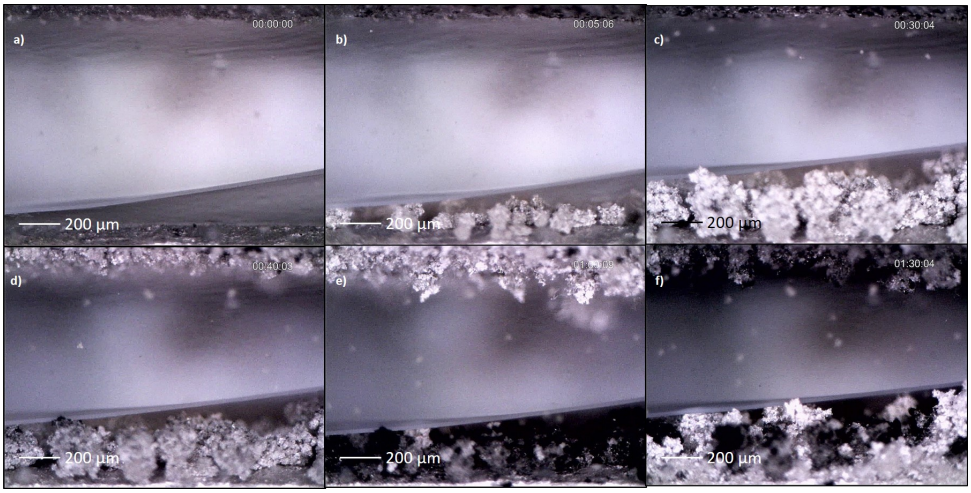


Figure 5.3: Time evolution of Li deposits with Celgard separator placed on top. a) Start of Li deposition b) Initial stage of Li deposition (after 3 min), c) End of first deposition half cycle (30 minutes), d) Initial stage of Li stripping (40 min), e) End of the 1st stripping half cycle (60 minutes), f) End of second deposition half cycle (90 minutes)

While the optical cell allows the Li deposits to grow freely without pressurization in the given electrolyte window (in this case about 1 mm), the environment in common Li coin cells is different. The interelectrode distance is occupied by a separator and the cell is pressurized.

In order to study the effects imparted by a commercial Celgard separators to Li deposition, a Celgard separator was placed on top of one of Li electrodes and the experiment was repeated. The resulting morphology development is as shown in Fig. 5.3 (a-f). While the homogeneous growth in terms of height seems to be controlled by the separator, the initial nucleation is still random and uneven.

At the end of the first deposition, the deposits are 1.62 times denser than in the case of

unobstructed Li deposition, and the area coverage appears to have improved, indicating that the separator does indeed play a role in homogenizing the Li deposition. Another important observation is that the Li deposits manage to push the separator upwards with accumulation of dead Lithium and continued deposition. Therefore, it can be posited that such movements do happen in commercial cells at a much smaller scale, and with the accumulation of dead Lithium over time,(Lithium is directly exposed to the liquid electrolyte with these separators, and keeps consuming the liquid electrolyte for the SEI formation, eventually causing mass transfer limitation at some point) the homogeneity of Lithium deposition keeps worsening, eventually leading to dendrites.

Another issue here is also the size of the dendrite units. Unlike the mossy deposits, which are microsized in nature, and therefore suppressed to some extent by the Celgard separator, the dendrites can tend to be as thin as a few nanometres [17] and with the conventional Celgard separators being microporous and not nanoporous, they will not be able to resist the actual dendrite growth.

## 5.4. EFFECT OF NANOPOROUS CERAMIC SEPARATORS ON MORPHOLOGY EVOLUTION

Separators with nanosized ceramic particles have been widely studied in attempts to improve the lifetime of Li-metal based batteries. Researchers such as Tu et. al. [42] have also proposed a combination of ionomer coatings on Lithium and nanoporous ceramic based separators to improve the lifetime of the Li metal. It was, therefore, important to know the degree of performance improvement achieved solely by using these separators in the place of microporous Celgard separators.

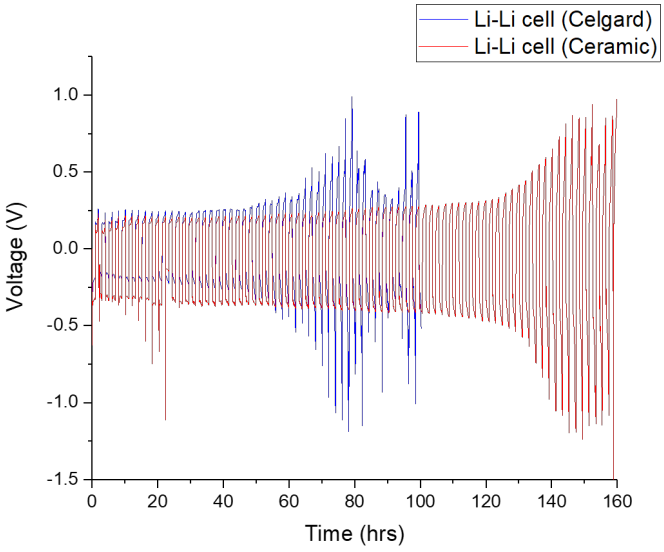


Figure 5.4: Galvanostatic cycling results for Li-Li symmetric cells with Celgard and Ceramic based separators

Two Li-Li symmetric cells were run, with a GF separator sandwiched between two Celgard separators in one of the cells and between two Ceramic (nanosized $Al_2O_3$) coated separators in the other. Both the cells were subjected to galvanostatic cycles of 2 $mAh/cm^2$.

From the results (as shown in Fig. 5.4), it can be observed that the voltage spikes corresponding to dendrite formation are already observed at around 80 hours in the case of Celgard separator based cells, while for Ceramic separator based cells, this is observed at around 150 hours.

The ceramic coated separators nearly double the lifetime of the Li metal, and this could be attributed to the fact that the nanosized ceramic particles reduce the effective pore size for Li transport, greatly reduce the SEI-forming reactions of the Lithium surface with the liquid electrolytes, and are thus able to resist dendrite formation for a longer duration. These separators should therefore, be considered to study possible synergistic effects with Li-SPEEK based surface coatings.

## 5.5. EFFECT OF POLYMER COATINGS ON LI

Having studied the deposition mechanism on bare Lithium and the influence of SEI and the type of separator on the deposition morphology, the research focus was now shifted to polymer based coatings on Li. As described in section 2.7.3, PVDF is known to work as an effective polymer coating on Li, and was therefore chosen as the reference coating.

### 5.5.1. OPERANDO MICROSCOPY

To study the effect imparted by a PVDF film to Lithium deposition, Li coated with PVDF was run against bare Li in the optical cell at a current density of 3 $mA/cm^2$. It was decided to start with stripping Li from the coated side and depositing onto the pristine side. This was done in order to create evenly distributed channels through the polymer layer and also to check whether the Li reversibly deposits back underneath the coated surface from the regions where it originally got stripped. The same operational logic was maintained for all the experiments involving polymer coatings.

During the first half cycle (Fig. 5.5 a-b), the coated PVDF layer starts moving upwards at several places as the Li is getting stripped. This could be because the Li stripping happening from underneath the coating results in a partial loss of contact with the Li substrate.

Interestingly, two modes of Li deposition though the coated layer are visualized, during the second half cycle (Fig. 5.5 c-d). While mossy deposition still occurs at the pinholes, owing to the PVDF layer being uneven, the amount of Lithium deposited at these pinholes is visually much smaller than the amount of Lithium that gets stripped from the pristine electrode on the other side. This confirms that the Li deposition is also happening underneath the PVDF layer and filling up the spaces created in the previous half cycle.

During the second stripping half cycle (Fig. 5.5e), some more movement of the PVDF layer is observed, although the movement is much lesser than that of the first half cycle. This could be explained by the fact that most of the Li stripping is now happening from the underneath of those regions that showed movement in the previous cycle, while some Li is also getting freshly stripped off the bulk, causing the movement of the coated

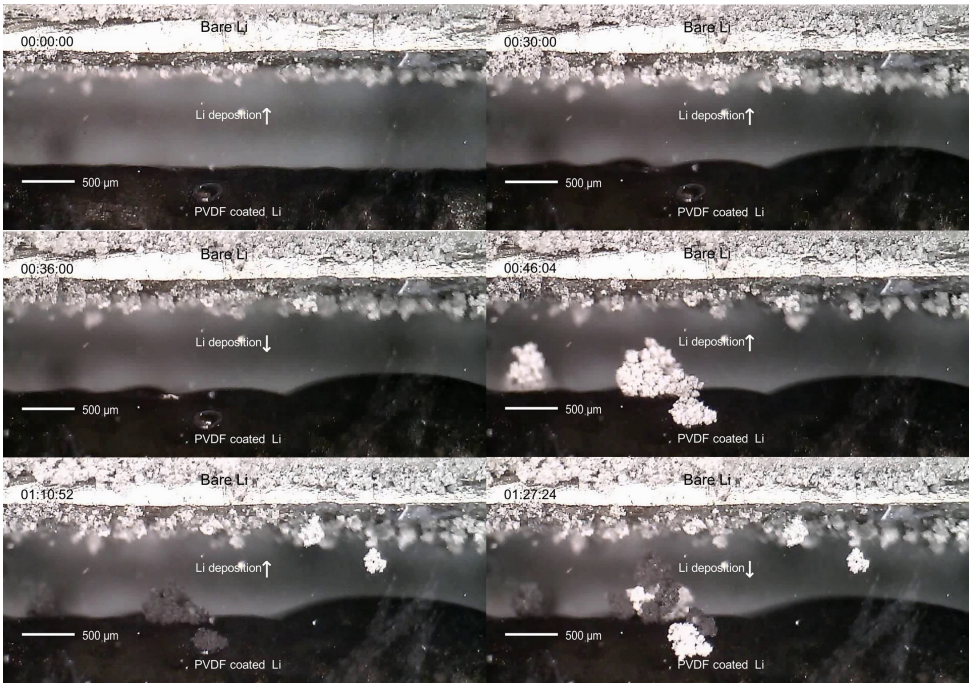


Figure 5.5: Time based morphology evolution of Li deposition with PVDF layer coated on Li. The upward motion of the PVDF layer during the cycling can be noticed.

layer in a few regions.

Having observed the dual mode of deposition with PVDF coating, the experiment was repeated for Li-SPEEK. The experiment was performed with a similar sequence for Li-SPEEK coated Li using the two concentrations i.e. 50 mg/ml and 10 mg/ml, which resulted in two different thicknesses of coating. The results obtained, in comparison to the bare Lithium deposition for 15 mins at 5 mA/cm$^2$ are as follows.

In the case of the thicker coating (Fig. 5.6, centre), uneven mossy formation is observed, most likely from pinholes, but the upward motion of the polymer layer cannot be visualized as in the case of PVDF. The density of deposition is, in fact, 8% lesser than that of bare Li deposition. This means that the conductivity of Li-SPEEK is very poor and as a result, the thickness of the coating is too much for a uniform deposition of Lithium.

The lower thickness of Li-SPEEK does result in a more uniform deposition of Li (Fig. 5.6, right), with the deposition being 1.4 times denser than that of bare Li deposition. However, the upward motion of the Li-SPEEK layer can still not be visualized; one cannot conclude for sure if the deposition occurs underneath the SPEEK layer. At the given thickness, the Li-SPEEK could have also acted like a template for homogeneous deposition rather than a coating underneath which deposition occurs.

The experiment with Li-SPEEK was repeated with a few changes: 1 wt% $TiO_2$ nanoparticles were added to the Li-SPEEK solution to improve the conductivity (more on conductivity improvement under the EIS results section) and the operando cycling was now

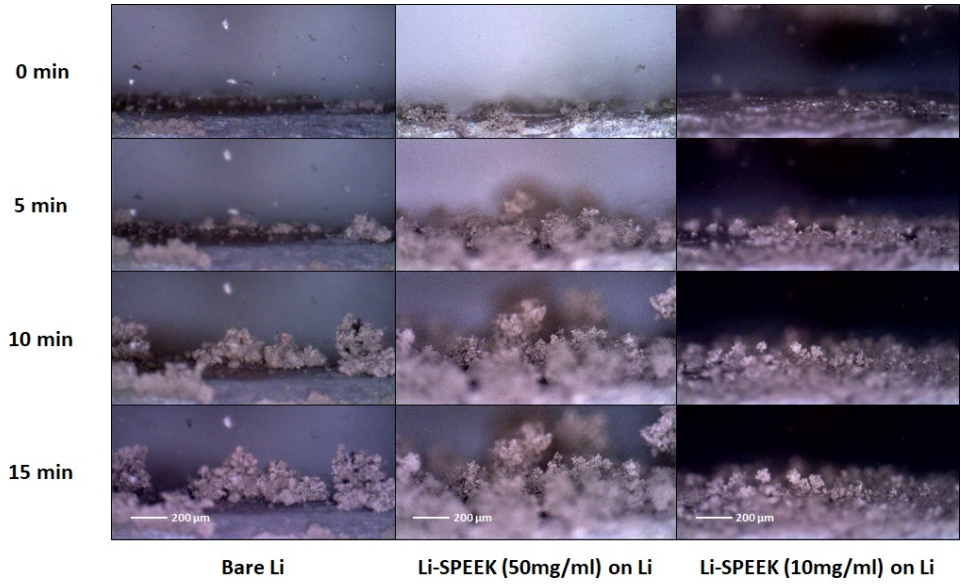


Figure 5.6: Comparison of Li deposition morphology evolution in the case of Bare Li (left), Li-SPEEK (50 mg/ml DMSO) coated Li (centre), and Li-SPEEK (10 mg/ml DMSO) coated Li (right). The deposits with 10mg/ml Li-SPEEK coating appear more even, both in terms of height and area coverage.

carried out at 3 mA/cm$^2$ instead of 5 and with deposition cycle of 25 mins instead of 15 (like in the case of PVDF).

The results, shown in Fig. 5.7, can be explained as follows. The cycling starts with stripping from the coated Li and deposition onto the pristine Li. By the end of the first half cycle (Fig. 5.7b), several pore-like formations can be observed on the surface of the coated electrode.

During the second half cycle (Fig. 5.7 c-d), the deposition observed appears to be uniform throughout the surface in terms of height, area coverage, and size of the deposits, although it still does not appear to be underneath the coating. The evenness of Li deposition on the coated side is maintained during the second deposition as well. (Fig. 5.7e).

With a positive result of uniform Li growth in the case of the doped Li-SPEEK coating and PVDF, it was now important to further validate these results for long term galvanostatic cycling.

### 5.5.2. EIS AND GALVANOSTATIC CYCLING

The pre-cycling Electrochemical Impedance Spectroscopy results for Li-Cu test cells with 1M $LiPF_6$ EC:DMC (1:1) electrolyte and four different types of Li metal anode (in terms of surface coatings) are as shown in Fig. 5.8. Clearly, the overall ionic conductivity of the system decreases in each of the cases where surface coatings are involved.

It should be noted that both Li-SPEEK and Li-SPEEK-$TiO_2$ coatings were obtained from solutions with a concentration of 10 mg/ml, while the PVDF solution was of 50

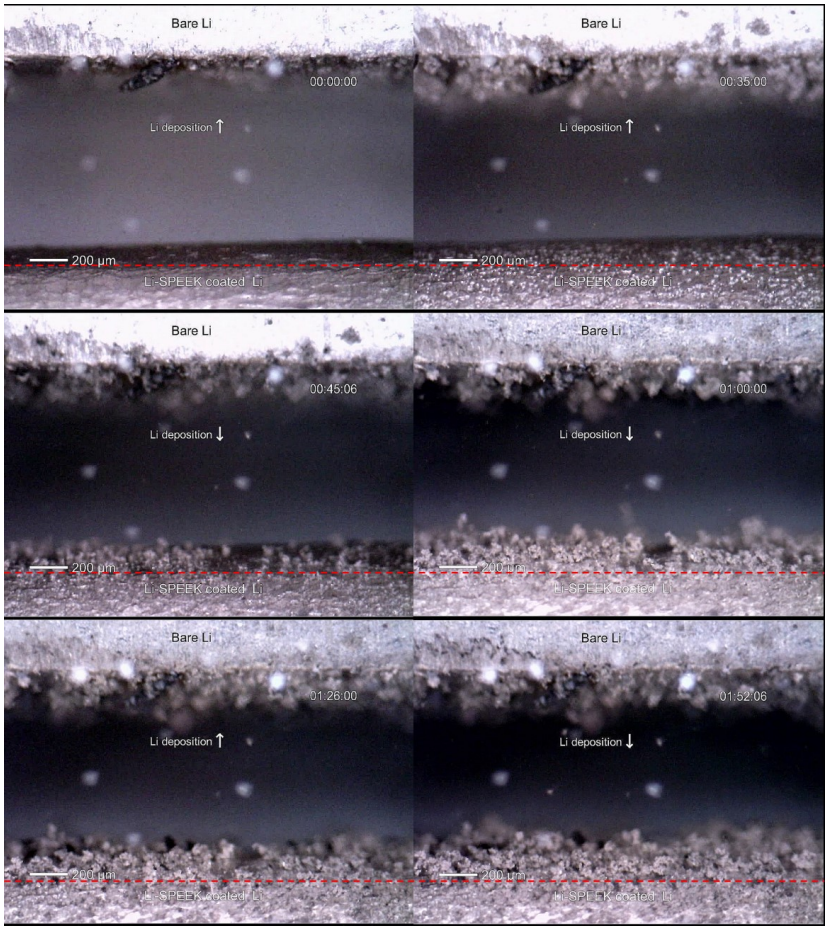


Figure 5.7: Time based morphology evolution of Li deposition with Li-SPEEK w/ 1 wt% $TiO_2$ (10 mg/ml DMSO) layer coated on Li. The deposits on the coating side appear even, both in terms of height and area coverage.

mg/ml concentration, mainly owing to the fact that PVDF gives a coarser coating and is more susceptible to pinholes at lower thicknesses.

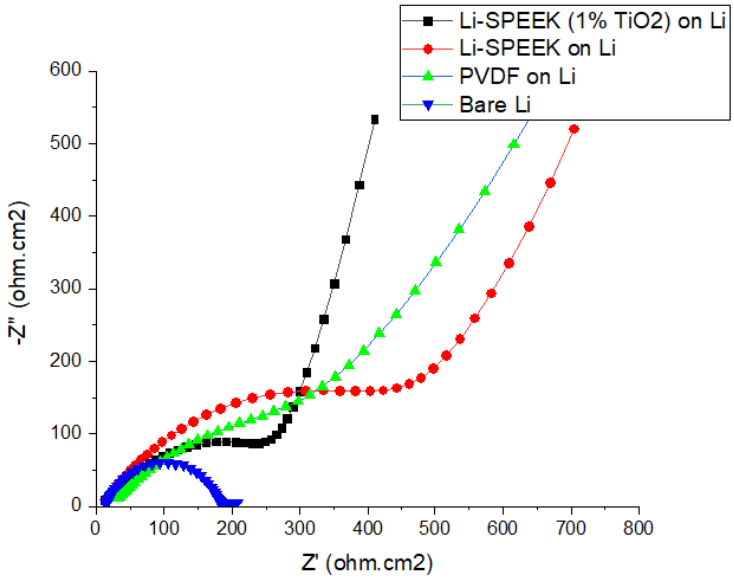


Figure 5.8: EIS Results for Li-Cu cells with Li side coated

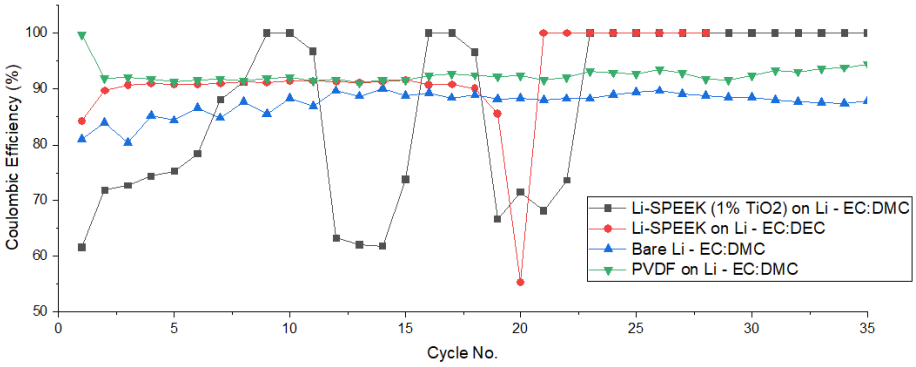


Figure 5.9: Galvanostatic cycling results for Li-Cu symmetric cells cycled for 1 mAh/cm$^2$ (Coated Li electrodes compared to Bare Li)

While the addition of $TiO_2$ appears to double the overall ionic conductivity (assuming the thickness of the coating is about 3 micron based on experiments in Section 3.4, this would be an increase from about 0.5 x$10^{-6}$ to 1 x$10^{-6}$ S/cm), this is still far off from the expected conductivity increase according to previous works (nearly 10 times according to [41]), and more importantly, still much higher than that of bare Lithium (The overall

ionic resistance for bare Lithium is around 175 ohm.cm$^2$, while in the case of Li-SPEEK doped with $TiO_2$, this value is around 350 ohm.cm$^2$, nearly the double)

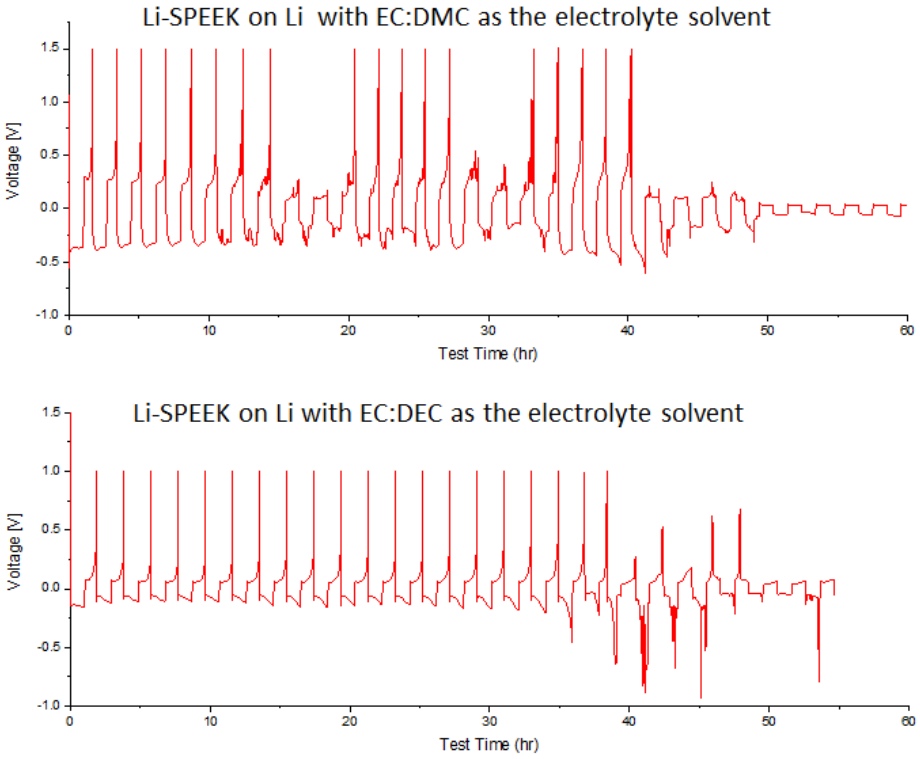


Figure 5.10: Galvanostatic cycling results for Li-Cu cells. Top: Voltage traces for Li-SPEEK (with 1% $TiO_2$) coated on Li vs Cu, in $LiPF_6$, EC:DMC(1:1) electrolyte 1 mAh/cm$^2$. Bottom: Voltage traces for Li-SPEEK coated on Li vs Cu, in $LiPF_6$, EC:DMC(1:1) electrolyte at 1 mAh/cm$^2$

On cycling these Li-Cu cells galvanostatically at 1 mAh/cm$^2$ (half cycles of 1 mA/cm$^2$ for 1 hour), the results obtained are as shown in Fig. 5.9 and Fig. 5.10. While the cell with bare Li maintains a Coulombic efficiency of around 87% over 30 cycles, PVDF performs well, averaging a Coulombic efficiency of 93%-94% for the first 30 cycles (The voltage traces for 100 cycles in the case of Bare Li and PVDF coated Li can be found in Appendix A.7).

The cell with Li-SPEEK-$TiO_2$ coated Li shows a highly fluctuating Coulombic efficiency averaging at around 75% for upto 25 cycles and then an ohmic short is observed. It is also important to note the irregularities appearing in the voltage trace starting at around the 7th cycle (Fig. 5.10 top), suggesting the instability of the coating with one of the electrolyte components. While $TiO_2$ is known to be stable with the commonly used battery electrolytes, ionomer based coatings have been shown to be possibly unstable, particularly with DMC, over extended cycling [42]. To test this hypothesis, films

of Li-SPEEK was immersed in pure DMC and pure DEC for 24 hours. Significant discoloration was observed in the case of Li-SPEEK with DMC (from colorless to yellow), while the colour change in pure DEC was very little. The long term changes in the transport and the mechanical properties of the SPEEK membranes upon DMC/DEC absorption are currently not known.

Therefore, it was of interest to investigate the performance of Li-SPEEK coated Li in EC:DEC based electrolyte. For coatings of Li-SPEEK (without the $TiO_2$ nanofiller) on Li, the Li-Cu cells were assembled and the voltage traces of the galvanostatic cycling at 1 mAh/cm$^2$ are shown in Fig. 5.10. The voltage traces do indeed seem stable for a longer number of cycles and the Coulombic efficiency is around 90%, however, irregularities in the voltage trace are observed starting from the 20th cycle, and an ohmic short is again obtained at around 25 cycles.

There definitely seem to be long term stability issues for the Li-SPEEK coating with DEC and DMC, with the degradation being slower in the case of DEC.

## 5.6. EFFECT OF THIN POLYMER COATINGS

Parallel to the tests involving Li-SPEEK and PVDF coated on Li metal, tests involving spincoated Cu electrodes were also conducted to study the possible benefits of thin, uniform polymer coatings as compared to the coatings on Li with little control over the uniformity of thickness.

### 5.6.1. VISUAL CHARACTERIZATION OF THIN FILMS ON CU WITH SEM AND AFM

PVDF and Li-SPEEK were spincoated on 10 micron thick Copper foils as described in section 3.5.

An SEM analysis of the coatings reveal the fact that the topology of coating seem to be significantly different for the two compounds. While the Li-SPEEK (Fig. 5.11a) results in a smooth uniform coating with almost no signs of pores at the microscale (as observed from SEM and AFM), the PVDF coating (Fig. 5.11b) results in a coarse topology, and the degree of roughness appears to increase at the edges of the coating. The coating also appears to be porous at the microscale.

As the SEM did not reveal much regarding the surface roughness of the Li-SPEEK coatings, an AFM line scan was carried out on bare copper and thin film coated copper respectively. The results are as shown in Fig. 5.12. It appears that the Li-SPEEK renders the surface smoother as compared to bare Copper. From a purely mechanical perspective, this implies that Li-SPEEK would work as an excellent protective layer that eliminates surface homogeneity related issues and is nanoporous to resist dendrites, even at low but uniform thicknesses. The issue is still, however, the low $Li^+$ conductivity at room temperature.

### 5.6.2. OPERANDO MICROSCOPY

Further, Li deposition on polymer coated Cu foils was studied by assembling optical cells with bare Li as the counter electrode in each cell. In Fig. 5.13, the pictures represent the bare copper electrode (left), Cu coated with PVDF (centre) and Cu coated with Li-SPEEK

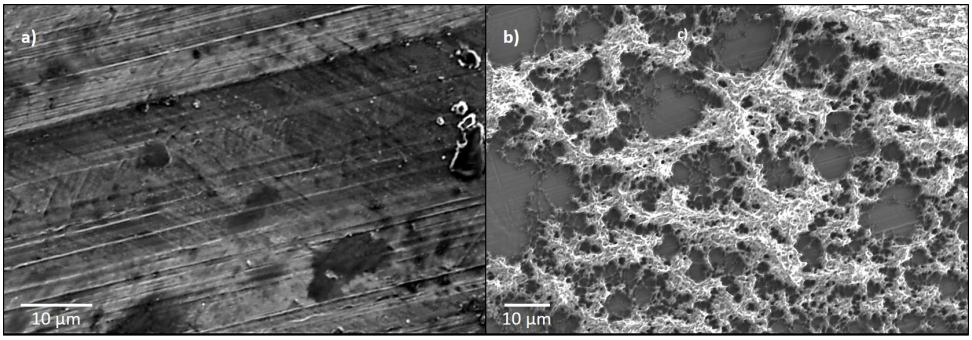


Figure 5.11: SEM images of Li-SPEEK (100 mg/ml DMSO) (left) and PVDF (50 mg/ml DMSO) layers spincoated on Cu

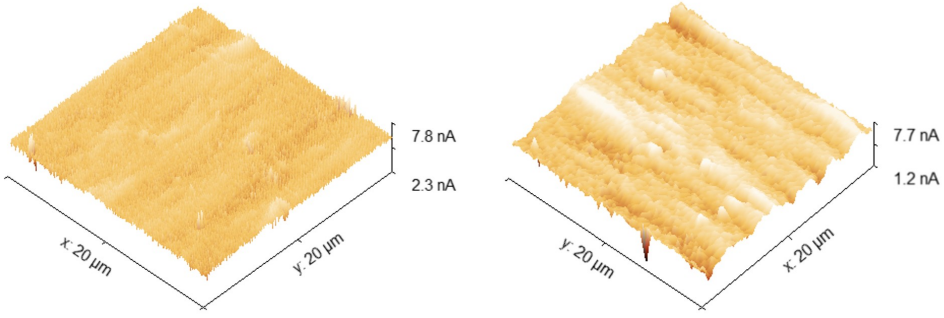


Figure 5.12: AFM Line Scan: Coated Copper foil (left) vs bare Cu foil (right)

(right). The four stages represented (top to bottom) here are 1) initial 2) after 1st half cycle at 5 mA/cm$^2$ for 15 min 3) After 3rd half cycle (2nd deposition) and 4) After the 5th half cycle, now the deposition being at 10 mA/cm$^2$

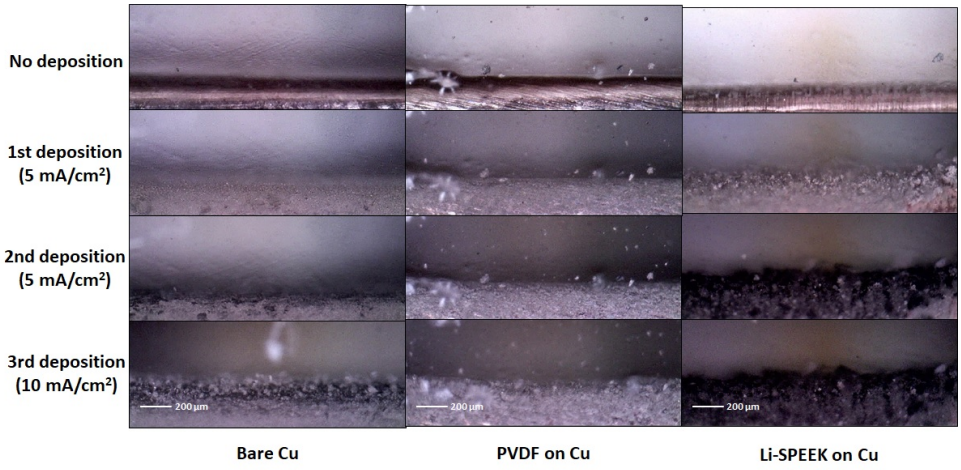


Figure 5.13: Comparison of Li deposition morphology evolution in the case of Bare Cu (left), PVDF (50 mg/ml DMSO) spincoated Cu (centre), and Li-SPEEK (25 mg/ml DMSO) spincoated Cu (right). The PVDF coating (center) enables a uniform Li deposition, while the deposition appears to occur on top of the coating in the case of Li-SPEEK(right).

While bare Cu (Fig. 5.13 left) and PVDF coated Cu (Fig. 5.13 centre) display uniform deposition upto the second deposition cycle, small mossy growths are observed on the unprotected Cu during the third deposition at 10 mA/cm$^2$. In contrast, no such mossy growth is observed with PVDF and the Li deposition appears to be contained within the polymer coating, even at a high current density of 10 mA/cm$^2$.

The observations are quite different in the case of Li-SPEEK coated on Cu (25mg/ml) (Fig. 5.13 right). The deposition is uniform in terms of surface coverage, but uneven in terms of height, right after the first deposition cycle. Moreover, the amount of dead Lithium also seems to be higher. It seems like the Li deposits on top of the Li-SPEEK layer and not through it.

To further test the impact of coating thickness on Li deposition, Li-SPEEK was spin-coated on Cu at three different concentrations – 25 mg/ml (Fig. 5.14a), 50 mg/ml (Fig. 5.14b) and 100 mg/ml (Fig. 5.14c). In all the three cases, Li deposition is observed on top of the Li-SPEEK layer rather than through it. In the case of 100mg/ml, the Li deposition is actually similar to mossy deposition on bare Li.

This is not true of PVDF, as it displays a remarkable uniformity of deposition, clearly under the layer.

Therefore, it could be concluded that Li-SPEEK does not work as a Li-conducting coating on Cu at practical current densities. Li depositing on top of the coating rather than through it led to a speculation that the Li-SPEEK layer on Cu could possibly be electronically conductive, as a result of Cu reacting with the Li-SPEEK layer.

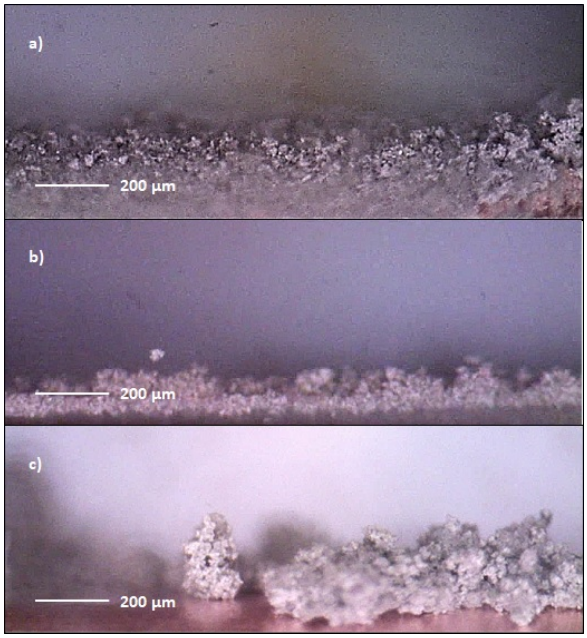


Figure 5.14: Comparison of morphology evolution after 1.25 mAh/cm$^2$ (5 mA/cm$^2$, 15 min) of Li deposition in the case of a) Li-SPEEK (25 mg/ml DMSO) spincoated Cu, b) Li-SPEEK (50 mg/ml DMSO) spincoated Cu and c) a) Li-SPEEK (100 mg/ml DMSO) spincoated Cu

### 5.6.3. EIS AND GALVANOSTATIC CYCLING

With the optical microscopy leading to mixed results for the polymer coatings, it was important to study the long term electrochemical behaviour of thin film coated Cu substrates for Li deposition in order to be able to arrive at possible conclusions regarding their performance.

From the pre-cycling EIS curves (Fig. 5.15), it can be observed that the overall ionic conductivities for both Li-SPEEK (25 mg/ml DMSO) and PVDF (50 mg/ml DMSO) coated Cu are lower than that of Bare Cu, despite them being ultra-thin in nature. (While the overall ionic resistance for Bare Cu is around 350 ohm.cm$^2$, this value is around 700 ohm.cm$^2$ for Li-SPEEK (25 mg/ml DMSO) coated Cu and 850 ohm.cm$^2$ for PVDF (50 mg/ml DMSO) coated Cu).

The galvanostatic cycling results (Fig. 5.16) provide some interesting insights into the long term performance and stability of these coatings. While bare Cu cell consistently has a Coulombic efficiency of 85-90%, the cell with Li-SPEEK coating also has a very similar Coulombic efficiency for upto 30 cycles. This is understandable as the Li deposition pattern is likely similar to that on bare Cu, as demonstrated by the operando microscopy. It does indeed appear that the Li deposition is happening on top of the Li-SPEEK layer on Cu, further strengthening the possibility of the Li-SPEEK layer on Cu somehow being electronically conductive. In the case of the cell with the PVDF coating, however, the Coulombic efficiency drops all the way from 85% to below 70% over 30 cycles. A look at the topology of the thin film coatings through SEM (Fig. 5.11) provides a

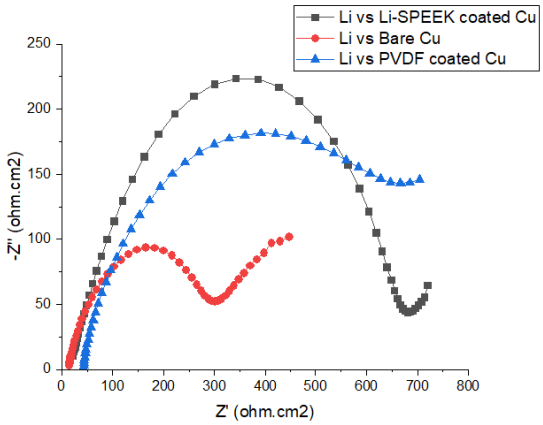


Figure 5.15: EIS Results for Li-Cu cells with Cu side spincoated

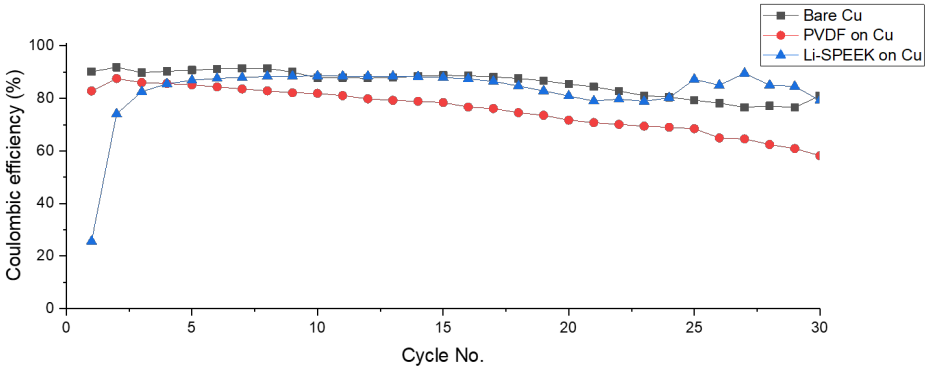


Figure 5.16: Galvanostatic cycling Results for Li-Cu cells with Cu side spincoated

good explanation of why this might be happening.

The highly porous nature of the thin film of PVDF coated on Cu ensures that Li easily passes through it and deposits underneath the layer. While this might work well for the first few cycles as observed from the operando microscopy, longer cycling results in decline of both the mechanical stability of the film (because the film is not thick enough) and the coulombic efficiency of Li deposition, possibly due to the obstruction to Li stripping created by the slowly disintegrating film. In short, the thickness of the PVDF (50 mg/ml DMSO) layer was insufficient considering the rough, porous surface it generates.

## 5.7. CHEMICAL ANALYSIS OF THE LI-SPEEK COATING USING XPS

To further understand the apparent electronic conductivity of the Li-SPEEK layer coated on Copper, a Copper foil spin coated with 100 mg/ml of Li-SPEEK was subjected to XPS

elemental analysis (survey mode). In comparison to the result for the bare SPEEK film, while Li is observed, confirming the presence of Lithium in the coating, around 3% of Copper is also observed in addition.

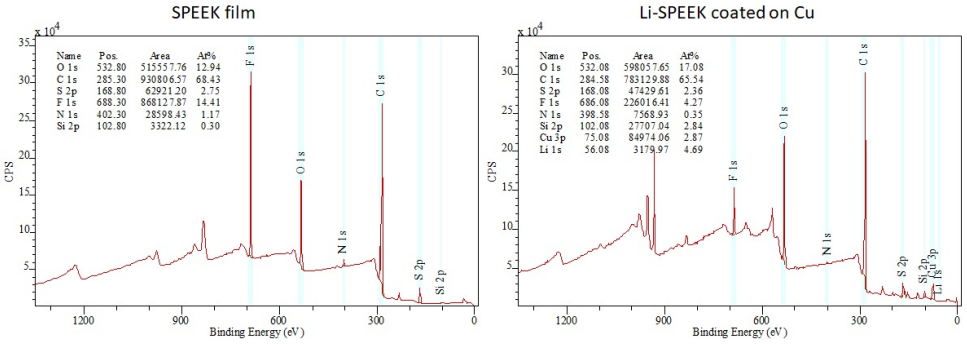


Figure 5.17: XPS spectra of bare SPEEK film (left) and Li-SPEEK spincoated on Cu (right)

This comes as a surprise, as XPS is a surface technique that has a penetration depth of only around 4 nanometres and the coating is expected to be of a few hundred nanometres in thickness. This implies that at very low thicknesses of SPEEK or Li-SPEEK on Copper (with DMSO as the solvent), certain copper based compounds are possibly formed that make the coating electronically conductive, and this could be due to the acidic nature of the Li-SPEEK in DMSO solution.

## 5.8. DISCUSSION

### 5.8.1. DEPOSITION ON BARE LITHIUM AND THE INFLUENCE OF SEI AND SEPARATOR ON THE MORPHOLOGY

The morphological evolution of Lithium at standard operational current densities (3-5/mA/cm$^2$) studied with the help of operando microscopy, revealed the random, highly localized, mossy growth of Lithium, along with the generation of dead Lithium after each cycle. This changes to a great extent with the introduction of surface modifications. A mechanically polished Li surface results in a more uniform, denser mossy growth. The presence of a separator close to the Li surface appears to homogenize the distribution of mossy Li growth over time, although the accumulation of dead Lithium over time still occurs, increasing the non-homogeneity of Li deposition with time.

### 5.8.2. ELECTROCHEMICAL PERFORMANCE OF LITHIUM WITH PVDF AS THE (REFERENCE) SURFACE COATING

PVDF was used a reference surface coating to visualize the movements and protective action of the layer during cycling. While the desired movements are indeed observed, confirming the transport of Lithium through this layer, an alternate deposition pathway is also observed at pinholes, thereby emphasizing the need to ensure the uniformity of coating. While Li shows remarkably even deposition through the spincoated layer of PVDF on Copper during the optical microscopy, the long term cycling of such a cell re-

sults in a rapid decline of Coulombic efficiency. This could be explained by the fact that PVDF, that generates a rather rough and porous surface may not be able to function effectively at very low thicknesses. It is, therefore, important to optimize the thickness of these coatings on Li.

### 5.8.3. ELECTROCHEMICAL PERFORMANCE OF LITHIUM WITH LI-SPEEK AND ITS $TiO_2$ DOPED VERSION AS SURFACE COATING

There are several takeaways from the set of experiments involving Li-SPEEK as a protective coating. In comparison to PVDF, Li-SPEEK is observed to provide a much smoother, non porous surface when spincoated on Copper. While this is favourable for the Li metal anode from a purely mechanical perspective, the poor $Li^+$ conductivity of Li-SPEEK in at room temperature (generally of the order of $10^{-6}$ S/cm as discussed in section 5.5.2) again results in a pinhole based deposition path for Lithium at high thicknesses. Attempts to increase the conductivity of the polymer by introducing 1 wt% $TiO_2$ as a nanofiller did not quite achieve the intended improvements. However, at low thicknesses (achieved through solvent control), both the Li-SPEEK and the $TiO_2$ doped Li-SPEEK coatings do appear to improve the uniformity of Lithium deposition both in terms of area coverage and the height of the deposits, although the presence of Li-SPEEK on top of these deposits is not very obvious from the videos.

The long term galvanostatic cycling, however, highlights the possible instability of the coating on long term exposure to carbonate based electrolytes, with the degradation being slower in the case of EC:DEC (1:1). This is, in fact, consistent with previous studies for ionomer based coatings on Li where a similar long term degradation was observed in the presence of DMC. [42] It is therefore, advisable to study the stability of these compounds with carbonate based electrolytes in greater detail.

While the Li deposition happening apparently on top of the Li-SPEEK coatings on Copper initially came as a surprise, the XPS analysis of these foils reveals the presence of Copper in the coating, which could offer an explanation to the electron conductive nature of the coating, possibly due to the presence of a Copper-based compound. It is possible that the Li-SPEEK coating renders the Copper surface acidic, and under acidic pH conditions, a potential of about 0.2V is sufficient for Copper to oxidize to its +2 state and react with the polymer, giving an electronically conductive layer.

### 5.8.4. PRACTICAL INSIGHTS

Besides this, a number of practical insights were also obtained regarding the electrochemical performance of the surface coatings on Lithium, the most important one being that the best way to create channels for Li conduction and ensure efficient functioning of these coatings is to always start with the discharge of these coated electrodes. Getting uniform, pinhole free coatings on Lithium was a major challenge in itself. Further insights into these aspects are provided in Appendix A.1.

# 6

# Conclusion and Recommendations

## 6.1. Conclusion

The electrochemical performances of bare Zinc and Lithium metal anodes were studied using operando microscopy. In the case of Zinc, it was possible to visualize the morphology evolution of zinc at low, moderate and high current densities, and these morphology transformations were correlated with their characteristic voltage traces.

With the increase in current density, depending on the controlling mechanism of ion transport (kinetics vs mass transfer) the Zinc deposits displayed different morphologies, both compact and non-compact in nature. Owing to competition between the kinetics and the mass transfer over the control of ion transport with time, compact deposits were observed to give way to non-compact deposits. Further, altering the operating parameters such as electrolyte composition/concentration, temperature and initial surface roughness resulted in slightly different morphologies. The crystal orientation would also change from directional to non-directional (polycrystalline) depending on the morphology.

In the case of Lithium, a very porous deposition was observed at standard current densities, but factors such as SEI and separator seemed to greatly influence it. It was also possible to visualize the actions of a polymer coating (PVDF) in ensuring uniform deposition underneath it.

SPEEK, the ionomer coating of interest, worked in both aqueous electrolyte system for Zn and Carbonate based electrolyte system for Lithium. Movement of the SPEEK polymer layer during deposition/stripping was observed in the case of Zinc. In the case of Lithium, a coating of Lithiated SPEEK on Li managed to suppress the non-homogeneous growth of Li to some extent at lower thicknesses. The thickness of the coating is crucial in the case of Lithiated SPEEK of Li as too high an ionic resistance of thicker coatings would result in alternative deposition paths through pinholes. Further, the addition of $TiO_2$ to Li-SPEEK also slightly improved the ionic conductivity and the performance of

the Li anode. To conclude, Li-SPEEK can potentially work as a protective coating for Lithium, provided the coating is of optimum and uniform thickness, and the conductivity is enhanced with the addition of a suitable material such as nanoparticle inorganic fillers. However, its long term stability in carbonate based electrolytes could be a potential concern, and should be investigated further.

## 6.2. RECOMMENDATIONS

**Improvements to the optical cell design for advanced electrochemical studies:**

The current design of the optical cell has a provision for two electrodes, sufficient to simulate a working battery. However, the presence of a reference electrode is recommended when carrying out electrochemical studies such as cyclic voltammetry. With the system showing a lot of promise as a tool for electrochemical studies, it is advisable to come up with a new design of the optical cell that also includes a provision for a reference electrode.

**Improvements to the optical cell design to enable long term cycling:**

While the electrochemical study using operando microscopy provides information regarding the first few cycles of an electrochemical process, the long term operation of it becomes impractical for several reasons.

The minimum possible interelectrode distance possible is currently 1 mm. While this works well for studying the morphology growth under non pressurized conditions, this is not fully reflective of the morphology growth under pressure and with a separator inside a battery, with a much lower interelectrode distance. In the case of both Zinc and Lithium, a high interelectrode distance means that the Sand's time conditions are reached much earlier than in batteries, thereby limiting long term study opportunities. Efforts should be made to lower the interelectrode distance and also accommodate a separator at the same time, so that the setup gets closer to simulating real life batteries.

In aqueous systems, there is continuous generation of bubbles (generation of $O_2$ and/or $H_2$) that lowers the video quality and also the efficiency of the experiment to some extent. It would also be advisable to think of a strategy to overcome this phenomenon for long term studies of aqueous systems.

**A detailed study of the voltage profiles and corresponding morphologies for potential BMS applications:**

This project demonstrates the possibility of studying the morphology evolution in metal anodes in correlation to their voltage traces at different current densities using operando microscopy. While it would not be possible to visualize the metal insertion into intercalation based materials, studying a full cell in an operando microscopy setup as opposed to a symmetric cell would help further establish the correlation between crucial morphology changes on the anodes and their corresponding voltage traces in a full cell, which could be of use in future battery management systems.

**Application of Li-SPEEK in ether based electrolytes and in Li-Sulfur batteries:**

This project explored the possibility of using Li-SPEEK as a coating on Li in carbonate based electrolyte systems. However, Ether based electrolytes (such as LiTFSI in DOL/DME) have emerged as an option for a more stable operation of the Li metal anode and are currently used in Li-S batteries. Li-SPEEK, also an ionomer, provides additional benefits such as the blocking the diffusion of polysulfide ions onto the Li metal anode. It

would be of interest to evaluate the application of Li-SPEEK either as an anode surface coating or as a separator coating in Li-S systems.

**Blending SPEEK with PVDF:**

As demonstrated in this project, PVDF works effectively as a coating for Li deposition in carbonate based electrolyte systems. Therefore, combining Li-SPEEK and PVDF to produce synergistic effects could be an interesting option to explore for polymer coatings. PVDF blends have already been tried for Nafion [24]. Blending SPEEK with PVDF has also been tried, but for fuel cell membranes. [48] PVDF: Li-SPEEK (4:1 wt ratio) blend would be good place to start based on the work of He et al., [48] who investigated the miscibility of PVDF and SPEEK at different weight ratios and at different degrees of sulfonation.

# REFERENCES

[1] Chengjun Xu, Baohua Li, Hongda Du, and Feiyu Kang. Energetic zinc ion chemistry: the rechargeable zinc ion battery. *Angewandte Chemie International Edition*, 51(4):933–935, 2012.

[2] Guozhao Fang, Jiang Zhou, Anqiang Pan, and Shuquan Liang. Recent advances in aqueous zinc-ion batteries. *ACS Energy Letters*, 3(10):2480–2501, 2018.

[3] Brazil's aerotec to invest 5m in li-s battery company oxis energy; expanding into brazil, 2019.

[4] Luke Hencz, Hao Chen, Han Yeu Ling, Yazhou Wang, Chao Lai, Huijun Zhao, and Shanqing Zhang. Housing sulfur in polymer composite frameworks for li–s batteries. *Nano-Micro Letters*, 11(1):17, 2019.

[5] Guangyuan Zheng, Seok Woo Lee, Zheng Liang, Hyun-Wook Lee, Kai Yan, Hongbin Yao, Haotian Wang, Weiyang Li, Steven Chu, and Yi Cui. Interconnected hollow carbon nanospheres for stable lithium metal anodes. *Nature nanotechnology*, 9(8):618, 2014.

[6] XG Zhang. Secondary batteries—zinc systems| zinc electrodes: overview. *Encyclopedia of electrochemical power sources*, pages 454–468, 2009.

[7] Kevin N Wood, Eric Kazyak, Alexander F Chadwick, Kuan-Hung Chen, Ji-Guang Zhang, Katsuyo Thornton, and Neil P Dasgupta. Dendrites and pits: Untangling the complex behavior of lithium metal anodes through operando video microscopy. *ACS central science*, 2(11):790–801, 2016.

[8] Zhigang Xue, Dan He, and Xiaolin Xie. Poly (ethylene oxide)-based electrolytes for lithium-ion batteries. *Journal of Materials Chemistry A*, 3(38):19218–19253, 2015.

[9] Jeffrey Lopez, Allen Pei, Jin Young Oh, Ging-Ji Nathan Wang, Yi Cui, and Zhenan Bao. Effects of polymer coatings on electrodeposited lithium metal. *Journal of the American Chemical Society*, 140(37):11735–11744, 2018.

[10] T Maiyalagan and Sivakumar Pasupathi. Components for pem fuel cells: An overview. In *Materials science forum*, volume 657, pages 143–189. Trans Tech Publ, 2010.

[11] Chunxia Zhao, Da He, Yuntao Li, Jianfei Xiang, Peng Li, and Hung-Jue Sue. High-performance proton exchange membranes for direct methanol fuel cells based on a speek/polybenzoxazine crosslinked structure. *RSC Advances*, 5(59):47284–47293, 2015.

[12] Gamry. Basics of EIS, 2019.

[13] Allen J Bard, Larry R Faulkner, Johna Leddy, and Cynthia G Zoski. *Electrochemical methods: fundamentals and applications*, volume 2. wiley New York, 1980.

[14] Scott Speakman. Introduction to x-ray powder diffraction data analysis, 2019.

[15] Introduction Products and Scanning (SEM). Scanning electron microscopes (sem) | introduction to jeol products | jeol ltd., 2019.

[16] RY Wang, DW Kirk, and GX Zhang. Effects of deposition conditions on the morphology of zinc deposits from alkaline zincate solutions. *Journal of The Electrochemical Society*, 153(5):C357–C364, 2006.

[17] Peng Bai, Ju Li, Fikile R Brushett, and Martin Z Bazant. Transition of lithium growth mechanisms in liquid electrolytes. *Energy & Environmental Science*, 9(10):3221–3229, 2016.

[18] Daniel A Cogswell. Quantitative phase-field modeling of dendritic electrodeposition. *Physical Review E*, 92(1):011301, 2015.

[19] Jun Ming, Jing Guo, Chuan Xia, Wenxi Wang, and Husam N Alshareef. Zinc-ion batteries: Materials, mechanisms, and applications. *Materials Science and Engineering: R: Reports*, 135:58–84, 2019.

[20] Fang Wan, Linlin Zhang, Xi Dai, Xinyu Wang, Zhiqiang Niu, and Jun Chen. Aqueous rechargeable zinc/sodium vanadate batteries with enhanced performance from simultaneous insertion of dual carriers. *Nature communications*, 9, 2018.

[21] Ning Zhang, Fangyi Cheng, Yongchang Liu, Qing Zhao, Kaixiang Lei, Chengcheng Chen, Xiaosong Liu, and Jun Chen. Cation-deficient spinel znmn2o4 cathode in zn (cf3so3) 2 electrolyte for rechargeable aqueous zn-ion battery. *Journal of the American Chemical Society*, 138(39):12894–12901, 2016.

[22] Robert Eduard Franciscus Einerhand. Zinc electrode shape change. 1989.

[23] Anne Berger, Anna TS Freiberg, Armin Siebel, Rowena Thomas, Manu UM Patel, Moniek Tromp, Hubert A Gasteiger, and Yelena Gorlin. The importance of chemical reactions in the charging process of lithium-sulfur batteries. *Journal of The Electrochemical Society*, 165(7):A1288–A1296, 2018.

[24] Jing Luo, Rung-Chuan Lee, Jian-Ting Jin, Yu-Ting Weng, Chia-Chen Fang, and Nae-Lih Wu. A dual-functional polymer coating on a lithium anode for suppressing dendrite growth and polysulfide shuttling in li–s batteries. *Chemical Communications*, 53(5):963–966, 2017.

[25] JW Diggle, AR Despic, and JO'M Bockris. The mechanism of the dendritic electrocrystallization of zinc. *Journal of The Electrochemical Society*, 116(11):1503–1514, 1969.

[26] J-N Chazalviel. Electrochemical aspects of the generation of ramified metallic electrodeposits. *Physical review A*, 42(12):7355, 1990.

[27] C Brissot, M Rosso, J-N Chazalviel, and S Lascaud. Dendritic growth mechanisms in lithium/polymer cells. *Journal of power sources*, 81:925–929, 1999.

[28] JL Barton and J O'M Bockris. The electrolytic growth of dendrites from ionic solutions. *Proceedings of the Royal Society of London. Series A. Mathematical and Physical Sciences*, 268(1335):485–505, 1962.

[29] Grecia Garcia, Edgar Ventosa, and Wolfgang Schuhmann. Complete prevention of dendrite formation in zn metal anodes by means of pulsed charging protocols. *ACS applied materials & interfaces*, 9(22):18691–18698, 2017.

[30] Yaron S Cohen, Yair Cohen, and Doron Aurbach. Micromorphological studies of lithium electrodes in alkyl carbonate solutions using in situ atomic force microscopy. *The Journal of Physical Chemistry B*, 104(51):12282–12291, 2000.

[31] Dingchang Lin, Yayuan Liu, and Yi Cui. Reviving the lithium metal anode for high-energy batteries. *Nature nanotechnology*, 12(3):194, 2017.

[32] Xin-Bing Cheng, Rui Zhang, Chen-Zi Zhao, and Qiang Zhang. Toward safe lithium metal anode in rechargeable batteries: a review. *Chemical reviews*, 117(15):10403–10473, 2017.

[33] Aiping Wang, Sanket Kadam, Hong Li, Siqi Shi, and Yue Qi. Review on modeling of the anode solid electrolyte interphase (sei) for lithium-ion batteries. *npj Computational Materials*, 4(1):15, 2018.

[34] Nurhaswani Alias and Ahmad Azmin Mohamad. Morphology study of electrodeposited zinc from zinc sulfate solutions as anode for zinc-air and zinc-carbon batteries. *Journal of King Saud University-Engineering Sciences*, 27(1):43–48, 2015.

[35] JY Song, YY Wang, and C Cv Wan. Review of gel-type polymer electrolytes for lithium-ion batteries. *Journal of power sources*, 77(2):183–197, 1999.

[36] Xunliang Cheng, Jian Pan, Yang Zhao, Meng Liao, and Huisheng Peng. Gel polymer electrolytes for electrochemical energy storage. *Advanced Energy Materials*, 8(7):1702184, 2018.

[37] Munmaya Mishra. *Encyclopedia of Polymer Applications, 3 Volume Set.* CRC Press, 2018.

[38] Anil Arya and AL Sharma. Structural, electrical properties and dielectric relaxations in na+-ion-conducting solid polymer electrolyte. *Journal of Physics: Condensed Matter*, 30(16):165402, 2018.

[39] Zhenguang Gao, Shaojian Zhang, Zhigen Huang, Yanqiu Lu, Weiwei Wang, Kai Wang, Juntao Li, Yao Zhou, Ling Huang, and Shigang Sun. Protection of li metal anode by surface-coating of pvdf thin film to enhance the cycling performance of li batteries. *Chinese Chemical Letters*, 30(2):525–528, 2019.

[40] Jialiang Lang, Yuanzheng Long, Jiale Qu, Xinyi Luo, Hehe Wei, Kai Huang, Haitian Zhang, Longhao Qi, Qianfan Zhang, Zhengcao Li, et al. One-pot solution coating of high quality lif layer to stabilize li metal anode. *Energy Storage Materials*, 16:85–90, 2019.

[41] Shuang Jiang, Yong Lu, Yanying Lu, Mo Han, Haixia Li, Zhanliang Tao, Zhiqiang Niu, and Jun Chen. Nafion/titanium dioxide-coated lithium anode for stable lithium–sulfur batteries. *Chemistry–An Asian Journal*, 13(10):1379–1385, 2018.

[42] Zhengyuan Tu, Snehashis Choudhury, Michael J Zachman, Shuya Wei, Kaihang Zhang, Lena F Kourkoutis, and Lynden A Archer. Designing artificial solid-electrolyte interphases for single-ion and high-efficiency transport in batteries. *Joule*, 1(2):394–406, 2017.

[43] Savitha Thayumanasundaram, Vijay Shankar Rangasamy, Jin Won Seo, and Jean-Pierre Locquet. Lithium polymer electrolytes based on sulfonated poly (ether ether ketone) for lithium polymer batteries. *European Journal of Inorganic Chemistry*, 2015(32):5395–5404, 2015.

[44] Ying Shi and RA Weiss. Sulfonated poly (ether ether ketone) ionomers and their high temperature shape memory behavior. *Macromolecules*, 47(5):1732–1740, 2014.

[45] Beata Teresa Koziara. *Thin sulfonated poly (ether ether ketone) films for the dehydration of compressed carbon dioxide.* University of Twente, 2015.

[46] F Alloina and C Iojoiu. Composite polymer electrolytes for electrochemical devices. In *Polymer Electrolytes*, pages 129–175. Elsevier, 2010.

[47] Jin Zheng and Yan-Yan Hu. New insights into the compositional dependence of li-ion transport in polymer–ceramic composite electrolytes. *ACS applied materials & interfaces*, 10(4):4113–4120, 2018.

[48] Shaojian He, Shaoxiong Zhai, Chong Zhang, Yang Xue, Wei Yang, and Jun Lin. Effect of sulfonation degree and pvdf content on the structure and transport properties of speek/pvdf blend membranes. *Polymers*, 11(4):676, 2019.

[49] Paul Heiney. Basics of XRD, 2019.

[50] Ming Song, Hua Tan, Dongliang Chao, and Hong Jin Fan. Recent advances in zn-ion batteries. *Advanced Functional Materials*, 28(41):1802564, 2018.

[51] Yasuhiro Awakura, Toshiya Doi, and Hiroshi Majima. Determination of the diffusion coefficients of cuso4, znso4, and niso4 in aqueous solution. *Metallurgical Transactions B*, 19(1):5–12, 1988.

# A

# APPENDIX

## A.1. PRACTICAL ASPECTS OF OPERANDO MICROSCOPY

### A.1.1. CHOICE OF MICROSCOPE

Optical microscopy is generally limited by the resolution, the minimum observable range is limited to the wavelength of light (400 – 700 nm). Further, the microscopes have their own resolution limits as all microscopes do not go up to the optical limit in terms of magnification. When it comes to video microscopy, the video resolution of the camera also matters, as this would ultimately decide the quality of the produced video. Presented with two choices, an Olympus BX series microscope equipped with a Dino Lite eyepiece camera (1.3MP) and a standalone Dino-lite Edge digital microscope (5MP, 220X)

The handheld digital microscope proved to be advantageous over the standard microscope setup with respect to the following aspects: a) While the standard microscope had a magnification of upto 100X, the eyepiece camera had a poor image/video quality of only 1.3 MP. In contrast, the Dino lite handheld microscope offers a resolution of upto 220X and a superior video quality of 5 MP at 15 FPS. b) It has a better source of light and offers greater degree of control over the overall brightness and the polarizability of light.

While the chosen microscope turned out to be an excellent option for operando microscopy at moderate to high current densities for Zinc and all current densities for Lithium, the setup lacked in effectively capturing/recording the initial phase of Zinc deposition at low current densities as it was limited by the optical resolution of 220X. A microscope with similar brightness and polarisation control but with a greater magnification range is therefore desirable to increase the amount of information that can be extracted from such operando microscopies.

Alternatively, in-situ TEM was used to study the initial deposition mechanism of Zinc, but introducing liquid electrolyte in the TEM setup proved to be quite challenging, resulting in a low success rate of experiments.

### A.1.2. BUBBLE FORMATION: POSSIBLE EXPLANATION AND IMPACT ON COULOMBIC EFFICIENCY

One of the common occurrences in operando microscopy videos of Zinc was the bubble formation during cycling, particularly at the anode for that half cycle (the electrode being stripped). Since the reaction at the anode is an oxidation reaction that releases electrons, (ie. Zn -> $Zn^{2+}$ + $2e^-$ ) the parallel reaction causing the water splitting/bubble formation should also be an oxidation reaction releasing electrons, and therefore splitting of water to give oxygen as $2H_2O$ -> $4H^+$ + $O_2$ + 4 $e^-$. If this is true, then the current supplied would also be spent on the parallel reaction.

The experiment and the video discussed in section 4.1 were used for computing the Coulombic efficiency, the amount of $O_2$ generated and the current spent on its generation.

The coulombic efficiency, as calculated from the voltage traces (fig. A.1b) is 2348 x 100/2400 = 97.833 %.

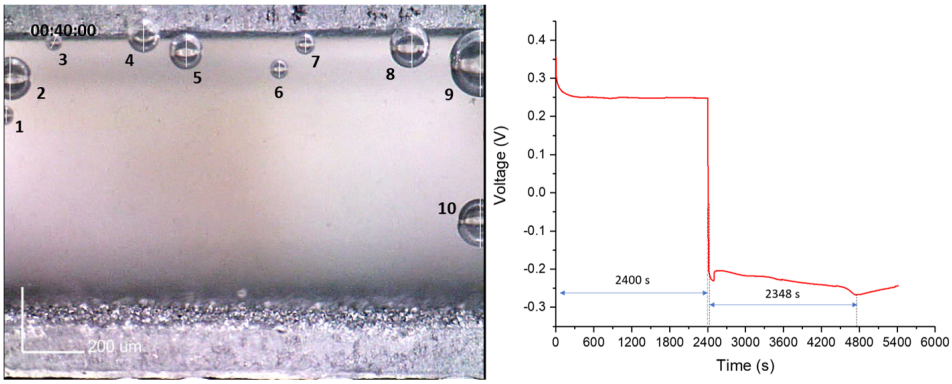


Figure A.1: Left: Index of bubbles generated during the first half cycle (for volumes, see table A.1. Right: Charge Discharge curve for the experiment

A still from the end of the deposition half cycle (Fig. A.1a) is used to measure the volume of $O_2$ generated. The measurements of the individual circles were made using ImageJ.

The approximate total volume was found to be 1.102 x $10^{-11}$ $m^3$. This corresponds to 4.92 x $10^{-10}$ moles of oxygen using the ideal gas relation of PV = nRT (This is assuming nearly atmospheric pressure inside the optical cell, although that is possibly not true). From Faraday's first law of electrolysis, Q = I.t = n.F.z where n= 4.92x $10^{-10}$ moles, F = 96485 C/mol and z = 4 (number of electrons involved in the reaction) Q = 1.9 x $10^{-4}$ C = 7.92 x $10^{-5}$ mAh For the same time period, i.e. 40 minutes the current applied across the cross section in view (1.568 mm length and 5 mm in depth) = 35 mA/$cm^2$ x (0.1568x0.5) $cm^2$ x 0.6667 h = 1.829 mAh.

Clearly, the current spent on water splitting is nearly 5 orders smaller than the total current applied. Even if the internal pressure were to be tenfold higher (i.e. 10 times higher moles generated), the current supplied would still be nearly four orders higher than the current used to split water.

Table A.1: Bubble volume calculations for 1M $ZnSO_4$, 35 mA/$cm^2$ for 40 minutes

| No. | Diameter (micron) | Volume ($m^3$) |
|---|---|---|
| 1 | 135.802 | $1.31135\times10^{-12}$ |
| 2 | 49.383 | $6.30568\times10^{-14}$ |
| 3 | 41.39 | $3.71267\times10^{-14}$ |
| 4 | 101.235 | $5.4324\times10^{-13}$ |
| 5 | 106.173 | $6.26674\times10^{-13}$ |
| 6 | 51.852 | $7.29955\times10^{-14}$ |
| 7 | 59.259 | $1.08959\times10^{-13}$ |
| 8 | 143.21 | $1.53787\times10^{-12}$ |
| 9 | 209.877 | $4.84054\times10^{-12}$ |
| 10 | 153.086 | $1.87848\times10^{-12}$ |
| **Total** | | $1.10203\times10^{-11}$ |

This means that the bubble formation observed does not influence the Coluombic efficiency by much. However, there have been instances where formation of large bubbles have influenced the overall voltage traces in the form of small overpotential spikes. It is not currently known to what extent the formed bubbles influence the observed morphology but the bubbles appear on the mostly on the stripped side and not the deposited side, and therefore the impact can be assumed to be minimal

### A.1.3. OCCURRENCE OF FLOATING MICROPARTICLES

In several videos, tiny flying objects of the size of 1-5 microns were observed during the early stages of zinc deposition, moving from the deposited electrode to the stripped electrode (i.e the direction opposite that of the conventional current). The direction of motion implies that the particles are somehow negatively charged.

Another observation was that the occurrence of these flying objects was very inconsistent and showed no correlation whatsoever with the applied current density. With passage of time, however, the motion of these particles almost completely subsided.

It could be argued that these flying objects are non metallic microparticles generated when the Zinc foils are mechanically polished with SiC paper. In addition to the SiC paper, another source could also be the Teflon based spacer used the cell that is made of microfibers and is slowly releasing these microparticles.

It is not clearly known why these particles move towards the electrode being stripped. One explanation could be that the sulfate ions that do not participate in the deposition process somehow associate with these microparticles, which causes them to be effectively negatively charged, and attracted to the electrode being stripped of Zn.

### A.1.4. SHADOW EFFECTS

As the video progresses, shadow effects are sometimes observed on an otherwise white background (especially in cases of videos with mossy deposits) thereby reducing the overall quality of the video. This is mostly due the shadow cast by the deposits, particularly those mossy in nature, and also sometimes the bubbles.

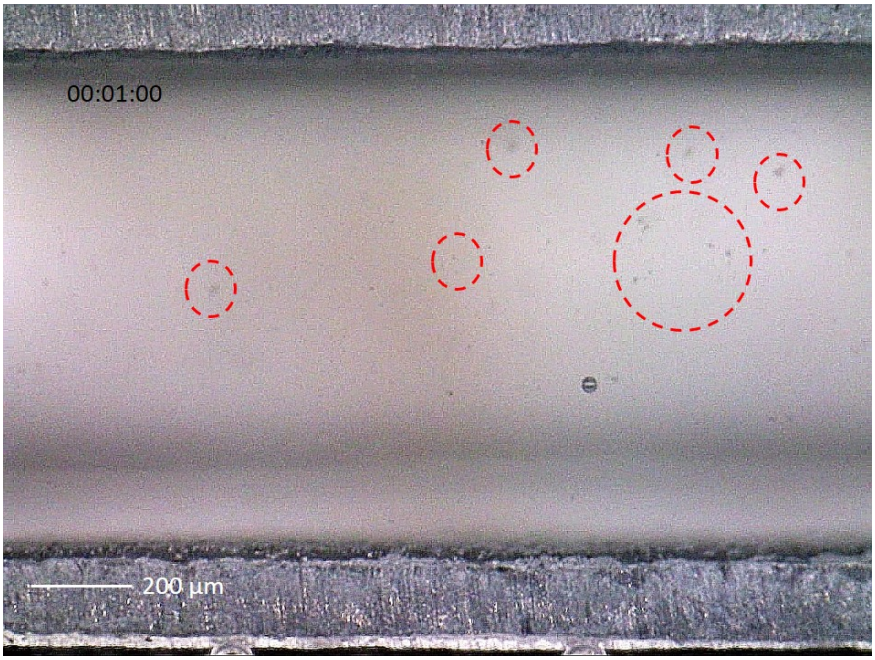


Figure A.2: Occurrence of floating microparticles during Zinc cycling

## A.2. CHALLENGES OF GETTING A UNIFORM COATING ON LI

Several important aspects need to be taken care of for obtaining smooth, homogenous coatings of polymers on Li

### A.2.1. CLEANLINESS AND HOMOGENEITY OF LI SURFACE

Commercially obtained Li foil generally has native oxide and nitride layers on the surface, owing to the highly reactive nature of Lithium. The best way to get rid of these layers is to mechanically clean them with a non reactive abrasive such as a piece rough polypropylene. The mechanical cleaning, however has to be done carefully to ensure that the soft surface does not develop a lot of roughness elements. Pressing the Li foil between two stainless steel plates or glass plates can also help in further flattening the foil, rendering it ideal for coating.

### A.2.2. OBTAINING UNIFORM COATINGS ON LI

Since advanced coating techniques such as spincoating were not available inside the glovebox. The only option was, therefore to drop cast the polymer dissolved in DMSO onto Lithium. Getting the desired thickness, based on solvent control, also works on the basis of trial-and error as the ionic resistance also scales with the thickness of the coating. Further, the coating is almost never uniform with drop casting (always decreasing at the edges), and therefore it is advised to start with a Li foil larger than the required size and then cut out the edges.

### A.2.3. DRYING METHOD AND TEMPERATURE

Drying the coated samples systematically is also crucial to getting a good coating, as failing to do would most likely result in a coating with a lot of pinholes, detrimental to the performance of the cell. The best method to obtain homogeneous, nearly pinhole free coating was to first dry the coated samples inside the glovebox for about an hour at 55 – 60 $^{o}$C. Majority of the solvent evaporates by this point, and then the samples are dried in the vacuum antechamber at 80 $^{o}$C and higher for 24 hours. This staged drying of the sample prevents the formation of pinholes due to rapid evaporation to a great extent.

## A.3. SAND'S TIME CALCULATION FOR ZINC DEPOSITION AT 120 MA/CM$^2$

The Sand's time for a binary electrolyte system is calculated as [27]:

$$T_s = \pi D\left(\frac{C_o F}{2 J t_a}\right)^2 \tag{A.1}$$

Where, the parameters and their values are as follows:

Table A.2: Sand's time Calculation for Zinc at 120 mA/cm$^2$

| **Sand's Time Calculator** | **Zn** |
|---|---|
| $C_o$, Concentration (mol/m$^3$) | 1000 |
| F, Faraday Constant (C/mol) | 96485 |
| D, Diffusivity (m$^2$/s) [51] | $3.93\times10^{-10}$ |
| $t_a$, Anionic transport number [18] | 0.6 |
| J (A/m$^2$)(1 mA/cm$^2$ = 10 A/m$^2$) | 1200 |
| **$T_s$ (sec)** | 221.72 |
| **$T_s$ (min)** | 3.7 |

## A.4. POROSITY CALCULATION FOR ZINC AND LITHIUM DEPOSITS, AREAWISE

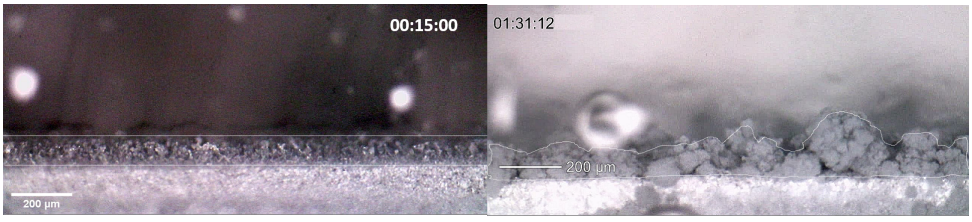


Figure A.3: Examples for Porosity Measurements

For the deposits whose porosity were to be calculated, the area of the deposits were calculated as shown in Fig. A.3 using ImageJ. While uniform dense deposits can be easily

approximated as rectangles, non-compact deposits require tracing as shown Fig. A.3b to compute the area. Assuming that the deposition is uniform across the depth (not in view), the calculated areas are then compared with the theoretical area of deposition for a 100% efficient 100% compact, deposit at that current density. The porosity is then calculated as:

$$P = \frac{(Actual Area – Theoretical Area)}{Actual Area} \tag{A.2}$$

| Description | Theoritical Height (µm) | Real Height (µm) | Overall Porosity | Video Screen length (µm) | Theoritical Area (sq. µm) | Real Area (sq. µm) | Overall Porosity |
|---|---|---|---|---|---|---|---|
| **1M $ZnSO_4$, 35 mA 1 hr** | 59.78 | 66.6 | 0.102 | | | | |
| **70 mA 30 min** | 59.78 | 60.1 | 0.005 | | | | |
| **120 mA 15 min** | 51.24 | 100 | 0.488 | | | | |
| **120 mA 11 min** | 34.16 | NA | | 1468 | 50152.21818 | 103316 | 0.515 |
| **120 mA 12.75 min** | 43.55 | NA | | 1468 | 63937.272 | 200023 | 0.680 |
| **120 mA 17 min** | 58.08 | NA | | 1468 | 85261.44 | 493513 | 0.827 |
| **Uneven** | | | | | | | |
| **35 mA 45 min** | 44.84 | NA | | 1236.5 | 55444.66 | 100340 | 0.447 |
| **35 mA+5 mA+35 mA 30 min** | 64.06 | NA | | 1567 | 100380.453 | 188450 | 0.467 |
| **Multiple cycles** | | | | | | | |
| **35 mA 15 min-1st Deposition** | 14.95 | NA | | 1555 | 23239.475 | 44166 | 0.474 |
| **35 mA 15 min-3rd deposition** | 14.95 | NA | | 1555 | 23239.475 | 51155 | 0.546 |
| **Others** | | | | | | | |
| **2M $ZnSO_4$** | 59.78 | 64 | 0.066 | | | | |
| **1M $ZnSO_4$+ 0.5 M $Na_2SO_4$** | 59.78 | NA | | 1859 | 111131.02 | 145510 | 0.236 |
| **1M $ZnSO_4$ High temp.** | 59.78 | NA | | 1700 | 101626 | 631688 | 0.839 |
| **1M $ZnSO_4$ Rough Zn** | 59.78 | 78 | 0.234 | | | | |

Figure A.4: Porosity Calculations for Zinc

| Description | Theoritical Height (µm) | Video Screen length (µm) | Theoritical Area (sq. µm) | Real Area (sq. µm) | Overall Porosity | Density Ratio | Relative Density |
|---|---|---|---|---|---|---|---|
| Bare Li | 6.06 | 1537 | 9314.22 | 281798 | 0.9669 | 0.033 | 100.00 |
| Mechanically polished Li | 6.06 | 2250 | 13635 | 148387 | 0.9081 | 0.092 | 278.00 |
| With separator on top of Li | 12.12 | 1544.64 | 18721.0368 | 349040 | 0.9464 | 0.054 | 162.27 |
| Li-SPEEK (50 mg/ml) on Li | 6.06 | 1210 | 7332.6 | 238544 | 0.9693 | 0.031 | 93.00 |
| Li-SPEEK (10 mg/ml) on Li | 6.06 | 1215 | 7362.9 | 157860 | 0.9534 | 0.047 | 141.11 |
| Li-SPEEK w/ $TiO_2$(10 mg/ml) on Li | 6.06 | 2097.5 | 12710.85 | 317703 | 0.9600 | 0.040 | 121.04 |
| PVDF spincoated on Cu | 12.12 | 1410 | 17089.2 | 71352 | 0.7605 | 0.240 | 724.61 |
| Li-SPEEK spincoated on Cu | 12.12 | 1410 | 17089.2 | 113979 | 0.8501 | 0.150 | 453.62 |
| Bare Cu | 12.12 | 1410 | 17089.2 | 121632 | 0.8595 | 0.140 | 425.07 |

Figure A.5: Porosity Calculations for Lithium

## A.5. XRD Results for Zn foils with additional Zinc Sulfate Hydroxide Hydrate Phase

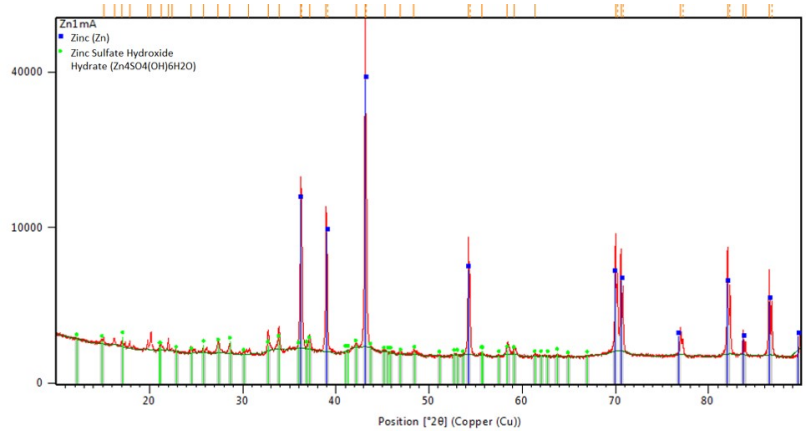


Figure A.6: XRD Spectra of Zinc deposits at 1 mA for 30 hrs showing the presence of the ZHS phase

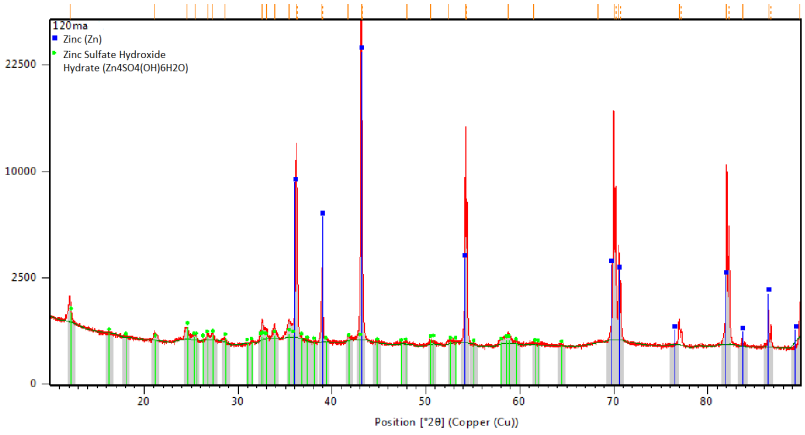


Figure A.7: XRD Spectra of Zinc deposits at 120 mA for 17.5 mins showing the presence of the ZHS phase

Zinc samples were cycled at different current densities from 1 mA/cm$^2$ to 120 mA/cm$^2$ in Zn Zn symmetric Optical cells. Post mortem XRD analysis of the samples revealed the presence of an additional Zinc Sulfate Hydroxide Hydrate phase for two of the current densities, i.e. 1 mA/cm$^2$ (for 30 hours) and 120 mA/cm$^2$ (for 17.5 minutes).

## A.6. SEM BASED MEASUREMENTS FOR VARIOUS ZINC DEPOSITS

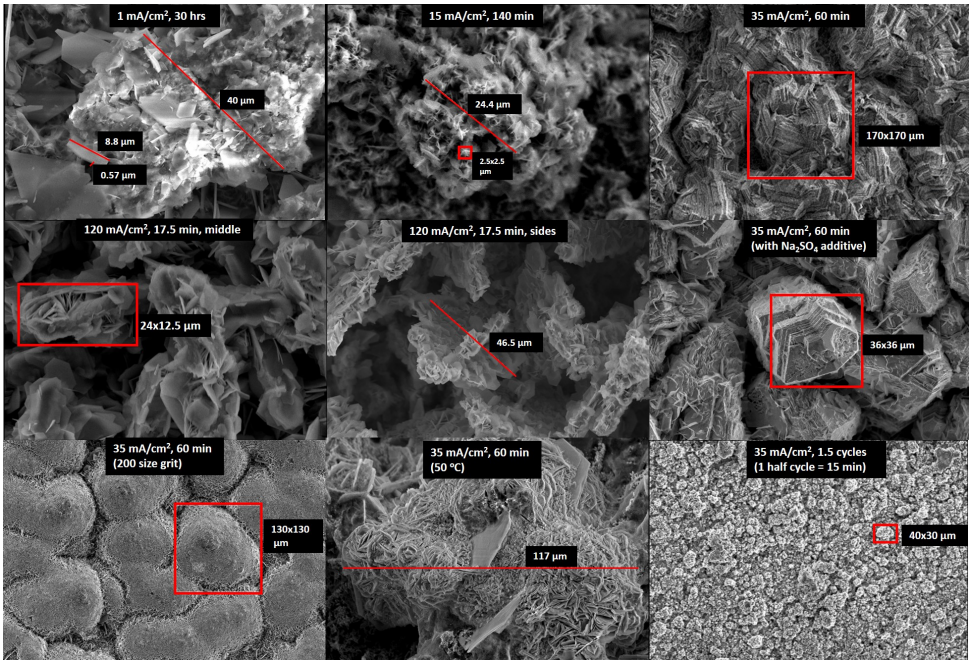


Figure A.8: SEM Image Measurements

The following measurements were made using ImageJ for the various types of deposits described in section 4.3.

# A.7. GALVANOSTATIC CYCLING - VOLTAGE TRACES FOR BARE LI VS CU AND PVDF COATED LI VS CU TEST CELLS

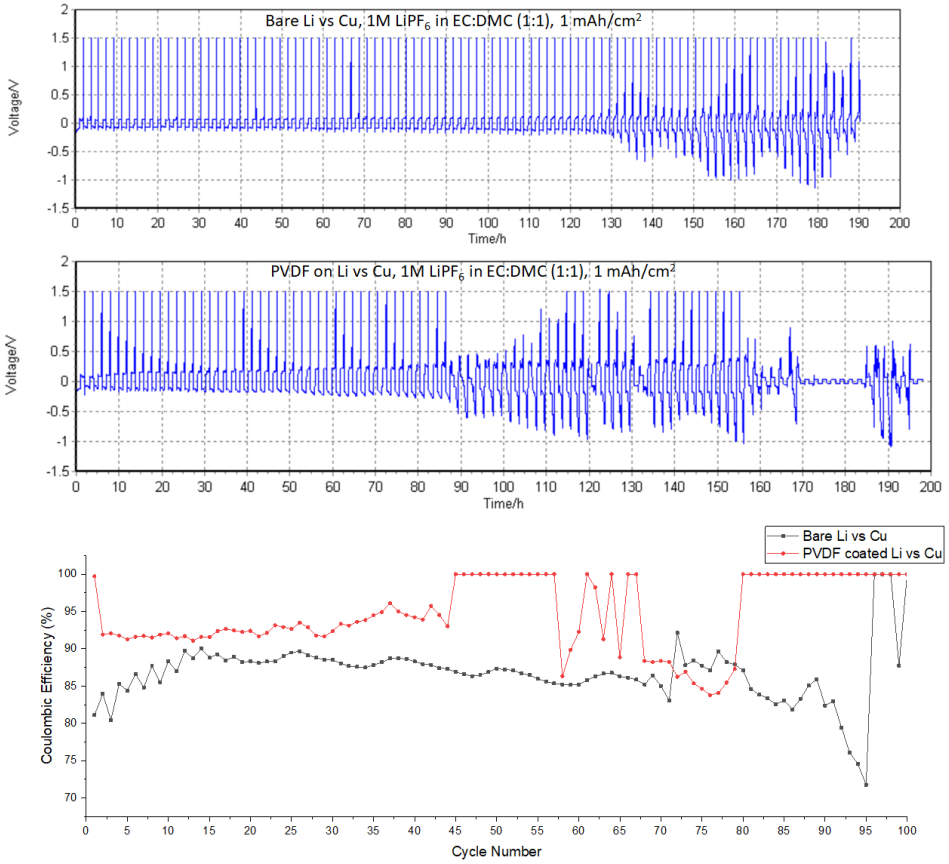


Figure A.9: Voltage traces for Bare Li vs Cu (Top) and PVDF coated Li vs Cu (Middle) test cells cycled at 1 mAh/cm$^2$. A comparison of the Coulombic efficiencies is provided at the bottom

The Galvanostatic voltage traces for the Li-Cu test cells with Bare Li and PVDF coated Li as the anode respectively are obtained as shown when cycled at 1 mAh/cm$^2$ (1mA/cm$^2$ with half cycle of 1 hour) for 100 cycles.

In comparison to the bare Li cell, the cell with PVDF coated Li has a higher Coulombic effciciency for about 45 cycles, although a slow buildup of impedance can be observed looking at the voltage traces. The voltage trace then shows irregularities for a few cycles, appears to recover at around 70 cycles, but then again appears to reach an ohmic short at about 80 cycles.

## A.8. STABILITY TEST FOR LI-SPEEK WITH DMC AND DEC

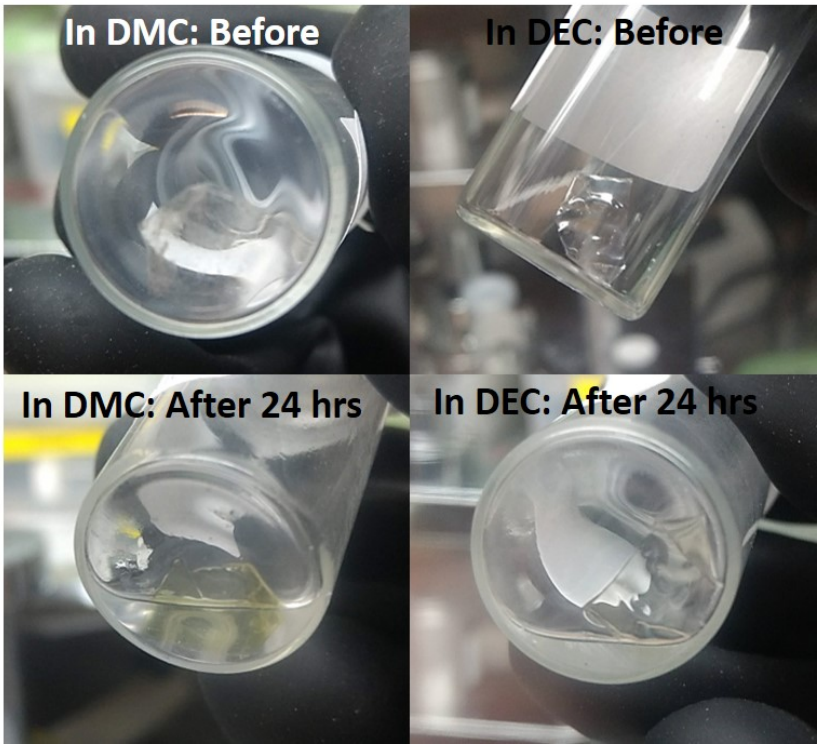


Figure A.10: Appearance of Li-SPEEK film before and after immersion in pure DMC and DEC for 24 hours. The sample in DMC exhibits a great degree of discolouration